POLITECNICO
MILANO 1863

SCUOLA DI INGEGNERIA INDUSTRIALE
E DELL'INFORMAZIONE

# HERA mission trajectory safety assessment through on-board failure detection

Tesi di Laurea Magistrale in
Space Engineering - Ingegneria Spaziale

*Developed at ESA ESTEC (Hera mission GNC)*
*Noordwijk, The Netherlands, April-September 2023*

Author: **Pietro Califano**

Student ID: 939515
Advisor: Prof. Michéle Roberta Lavagna
Co-advisors: Jesús Gil-Fernández
Academic Year: 2022-23

# Abstract

The Hera Mission, the contribution by the European Space Agency within the AIDA collaboration, is dedicated to studying the Didymos asteroid. In the Experimental Phase "Very Close Flyby," the spacecraft relies solely on its on-board GNC functionalities. The effort of the work has concentrated on devising Fault Detection algorithms to evaluate the trajectory safety independently of the GNC loop. A comprehensive analysis of the dynamical environment precedes the design phase, evaluating how various models impact trajectory propagation errors. Three strategies are explored, two utilizing a collision risk definition based on the Distance at Closest Approach (DCA) distribution and the establishment of a keep-out sphere around both asteroids. The first strategy involves raw measurements and local regression techniques to estimate DCA and its uncertainty, determining the probability of entering the keep-out sphere through integration, triggering a Collision Avoidance Maneuver based on a predefined threshold. The second strategy employs an unscented Kalman filter in Square Root form, processing observables akin to the navigation filter. The investigation extends to using the gravitational parameter as a considered state and its effect on unscented transform accuracy. The third approach adapts a pair of Square Root Unscented Kalman Filters within the Wald sequential hypothesis testing framework, employing a sigma point projector based on a Lambert solved algorithm to enforce PDF constraints. A Likelihood ratio informs the test, guiding decisions based on thresholds derived from target probabilities of inferential errors. To tackle the issue associated with the constrained filter dismissing physically inconsistent measurements, a secondary failure detection routine is introduced with a counter that monitors the filters rejections. All algorithms, implemented in MATLAB, underwent testing using Hera Experimental trajectory scenarios, providing critical insights into their assumptions, limitations, and performance.

**Keywords:** Hera mission, trajectory safety, on-board failure detection.

# Abstract in lingua italiana

La Missione Hera, il contributo dell'Agenzia Spaziale Europea all'interno della collaborazione AIDA, è dedicata allo studio dell'asteroide Didymos. Nella Fase Sperimentale di sorvolo molto ravvicinato, il veicolo farà affidamento esclusivamente sulle funzionalità di GNC a bordo. Il lavoro è stato concentrato sulla creazione di algoritmi di rilevamento di fallimenti per valutare la sicurezza della traiettoria in modo indipendente dal sistema GNC. Un'analisi della dinamica del moto precede la fase di progettazione, valutando come vari modelli influenzino gli errori di propagazione della traiettoria. Tre strategie sono state esplorate, di cui due utilizzanti una definizione del rischio di collisione basata sulla distribuzione della minima distanza di sorvolo e sulla creazione di una sfera di esclusione intorno ad entrambi gli asteroidi. La prima strategia impiega direttamente misurazioni e tecniche di regressione per stimare la minima distanza e la sua incertezza, determinando la probabilità di entrare nella sfera di esclusione mediante integrazione, e comandando una manovra di evitamento qualora tale probabilità dovesse superare la soglia prestabilita. La seconda strategia utilizza uno Square-Root Unscented Kalman filter, processando misurazioni similmente al filtro di navigazione. L'indagine si estende all'utilizzo del parametro gravitazionale con associata incertezza e al suo impatto sull'Unscented Transform. Il terzo approccio adatta una coppia degli stessi filtri in un test di ipotesi sequenziale, impiegando un Sigma Point projector basato sul Problema di Lambert per imporre vincoli alla PDF. Un rapporto di Verosimiglianza guida le decisioni del test, basate su soglie derivate dalle probabilità di errori inferenziali desiderate. Per affrontare il problema legato a misurazioni predette dal filtro fisicamente inconsistenti e perciò rifiutate, una procedura decisionale secondaria è stata introdotta tramite un contatore che monitora il numero di rifiuti del filtro. Tutti gli algoritmi, implementati in MATLAB, sono stati testati utilizzando lo scenario di missione di Hera. Le loro ipotesi, limitazioni e prestazioni sono criticamente discusse in fase di analisi.

**Parole chiave:** Missione Hera, sicurezza della traiettoria, rilevamento di fallimenti a bordo.

# Contents

# List of Figures

# List of Tables

# Acronyms

**ADCS** Attitude Determination and Control subsystem. 5, 6

**AFC** Asteroid Framing Camera. 5, 36, 37, 58

**AIDA** Asteroid Impact and Deflection Assessment. 2, 3

**ATCM** Autonomous Translation Control Manoeuvres. 6

**AU** Astronomical Unit. 32

**CA** closest approach. 27

**CAM** Collision avoidance manoeuvre. 27, 46, 107

**CDF** Cumulative distribution function. 46

**CI** Central Inertial. 59, 60

**CoB** Centre of brightness. 60, 61

**CoM** Centre of mass. 1, 25, 26, 29, 31

**COP** Close Observation Phase. 5, 12

**CRE** Collision risk estimator. vi, vii, 43, 44, 80

**DCA** Distance of Closest Approach. 6, 44, 54, 96, 99

**DCM** Direction cosine matrix. 59

**DCP** Detailed Characterization Phase. 5

**DKE** Dynamics, Kinematics and Environment. 40

**DV** Delta-V. 6

**ECP** Early Characterization Phase. 4

**ECRV** Exponentially correlated random variable. 29

**EKF** Extended Kalman filter. 62

**EXP** Experimental Phase. 5, 12, 33, 63

**FD** Failure detection. 27, 36, 58, 109

**FDI** Failure Detection and Isolation. 6, 10, 12, 21, 27

**FOGM** First-Order Gauss Markov Process. 42

**FoV** Field of view. 5, 38

**FT** Feature Tracking. 5

**GNC** Guidance, Navigation and Control. 5, 43, 75

**HF SRUSKF** High Fidelity Square-Root Unscented Schmidt Kalman Filter. 43, 66

**HFM** Higher fidelity model. 38, 40, 42, 82

**IP** Image Processing. 37, 40, 49, 52, 60, 74

**kepSRUSKF** Keplerian Square-Root Unscented Schmidt Kalman Filter. vi, 43, 53, 66

**KoS** Keep-out sphere. 46, 70, 82

**LFM** Lower fidelity model. 39, 40, 42, 81

**Los** Line of sight. 42, 52, 59

**LS** Least Squares. 49–51

**MA** Mission Analysis. 5

**NEA** Near-Earth Asteroids. 1, 2

**OBSW** On-Board Software. 27, 38, 46, 58, 66, 67

**PALT** Planetary Altimeter. 37

**PDF** Probability Density Function. 12, 14, 15, 18, 44, 46, 54, 55, 61, 63, 66, 67, 70, 83

**PDP** Payload Deployment Phase. 4

**PHA** Potentially Hazardous Asteroid. 1

**PoC** Probability of Collision. 14, 44, 82, 95, 96, 104

**RMS** Root-Mean Square. 51

**SCB** Spacecraft Body. 64

**SOI** Sphere of Influence. 4

**SPRT** Sequential Probability Ratio Test. vii, 14, 15, 44, 67, 104

**SRP** Solar Radiation Pressure. 32, 35, 57, 66

**SRUSKF** Square-Root Unscented Schmidt Kalman Filter. vi, 43, 62, 65

**SSA** Space Situational Awereness. 12

**TB** target body. 59

**TCA** Time of Closest Approach. 45

**UT** Unscented Transform. 20, 55, 56

**VCFB** Very Close Flybys. 5, 46

**WSPRT** Wald Sequential Probability Ratio Test. 15

# Acknowledgements

Numerous people have played a crucial role in the path that led to these words, and to each of them, I extend my heartfelt gratitude.
Firstly, my time at ESTEC as part of the Hera mission Team proved to be a transformative experience that I will cherish. Special thanks to my supervisor, Jesús, for giving me this exceptional opportunity and for his remarkable assistance and insightful discussions on GNC matters. Diego, for his invaluable explanations on the Hera design and patient answers to my questions. Hannah, for her insights into payloads design, testing, and valuable suggestions for the 6S Cubesat project. I would also like to express my sincere thanks to Ian Carnelli for his suggestions whenever I needed them.
Thanks to Professor Lavagna, for the rare yet thought-provoking talks and help in developing this work.
Among my friends, Davide, aka *"Perry"*, your ceaseless assistance and enriching conversations have been indispensable. Elena *"Pylo"*, I am grateful for all the discussions on filtering and navigation that we had in the past, as well as for your patience till it lasted. Pleng, Fabri, Luca M., Mala, Annaky, Ale, Lusvi, Luca N., Davide M., AleMiceli and Sergio, your presence has been equally important for me in the last years.
A special acknowledgment goes to the EPOPEA team, that marked one of the greatest experiences in my life. Together, we faced and overcame numerous challenges before, during, and after the months of my internship. In the end, it had been an experience far beyond a mere course project.
Last but certainly not least, my sincere appreciation goes to my family for their unwavering support, even when the nature of my work remains somewhat obscure to them. *P.C.,*

*22 November 2023*

# 1 | Introduction

## 1.1. Near-Earth Asteroids

Near-Earth Asteroids are a class of small bodies orbiting the Sun whose perihelion distance is estimated to be less than 1.3 AU [55]. These asteroids are considered scientifically significant targets for deep space exploration missions for three primary reasons:

1. They typically consist of compounds that offer insights into the early stages of Solar System evolution, characterized by intriguing dynamics of formation.
2. Some NEAs pose potential threats to Earth when their heliocentric trajectory intersects with Earth's. Specifically, asteroids with a semi-major axis larger than 1 AU and a perihelion distance less than 1.017 AU, known as "Apollo" asteroids, fall into the category of Potentially Hazardous Asteroid (PHA). The impact of such asteroids, especially those with dimensions in the hundreds of meters, could have catastrophic consequences for human activities and life on our planet.
3. NEAs are rich in materials of economic interest, making them potential targets for future commercial missions designed for resource exploitation.

A percentage of the NEA group, estimated to be around $15\% \pm 4\%$, is represented by binary asteroid systems, that is systems of one large primary asteroid and a smaller secondary, orbiting around their Centre of mass (CoM) [76].

### 1.1.1. The (65803) Dydimos binary asteroid

Exploring binary asteroid systems offers valuable insights into the intricate interaction between two celestial bodies, encompassing their complex gravitational dynamics, the formation and evolution processes of such systems, and their interaction with the broader solar system environment. Their study provides a unique opportunity to understand phenomena such as the YORP effect and its role in shaping these systems. Unlike single asteroids, the observation of binary systems from Earth allows for more accurate estimations of the mass and density of the bodies by measuring their orbital period and distance.

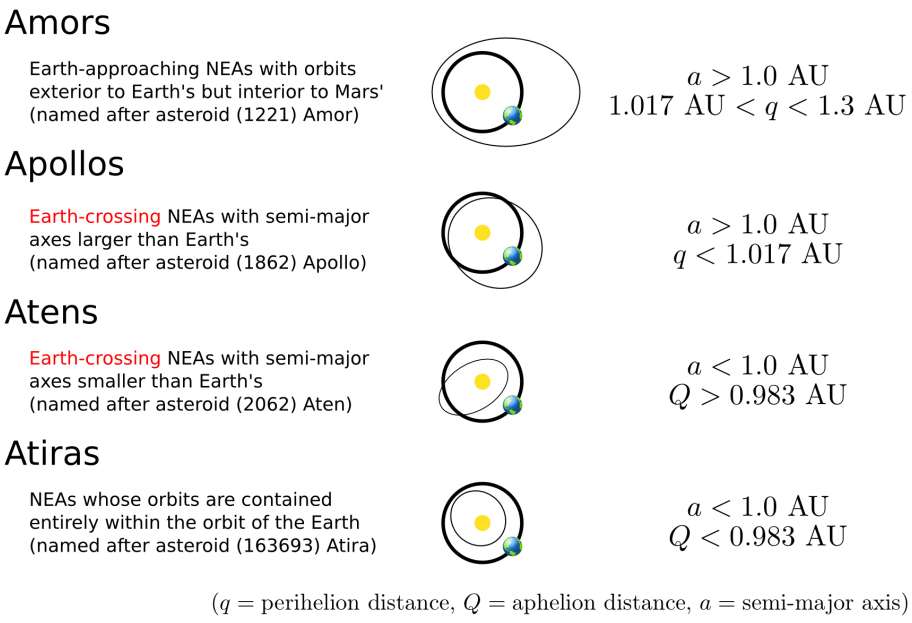


Figure 1.1: Near Earth Asteroids classification. Reproduced from [55].

The asteroid (65803) Dydimos, accompanied by its secondary Dimorphos (fig. 1.2, from APL DART mission gallery[1]), stands out as a particularly intriguing example within the Apollo NEA category: ongoing research suggests that Didymos may be at the structural stability limit typical for asteroids, a conjecture supported by its rapid spin period of around 2.26 hours marking it as the fastest-spinning object ever visited. Notably, Dimorphos resides at the recognized threshold between structures dominated by gravity and those dominated by strength. Furthermore, Dimorphos serves as an ideal subject for observing dynamic changes within the system resulting from an impact. This makes it a valuable candidate for comparative analysis with data obtained from the Hayabusa2 mission, specifically from the study of (162173) Ryugu.

## 1.2. AIDA: DART and Hera missions

Building upon these scientific interests, the Asteroid Impact and Deflection Assessment (AIDA) collaboration between NASA and ESA was established in early 2010s [16]. This collaboration consists of two interrelated yet independent missions aimed at demonstrating the Kinetic Impactor technology as mean to alter the trajectory of potentially dangerous asteroids. Simultaneously, it seeks to extensively examine both the impact process and the repercussions on binary systems [24]. DART and Hera missions, respectively, are

[1] `https://dart.jhuapl.edu/Gallery/`. Last visited: 02 Nov. 2023

Figure 1.2: The (65803) Dydimos binary asteroid as imaged by DART.

designed to embody these two objectives.
NASA DART spacecraft successfully launched on 24 November 2021 and impacted the secondary asteroid Dimorphos (in the work also referred to as Didymoon or as D2) on 26 September 2022, determining a change in its revolution period of around 32 minutes. While this outcome is currently solely validated through ground observations, it significantly surpasses the initial mission requirement by more than 25 times [52]. The Hera

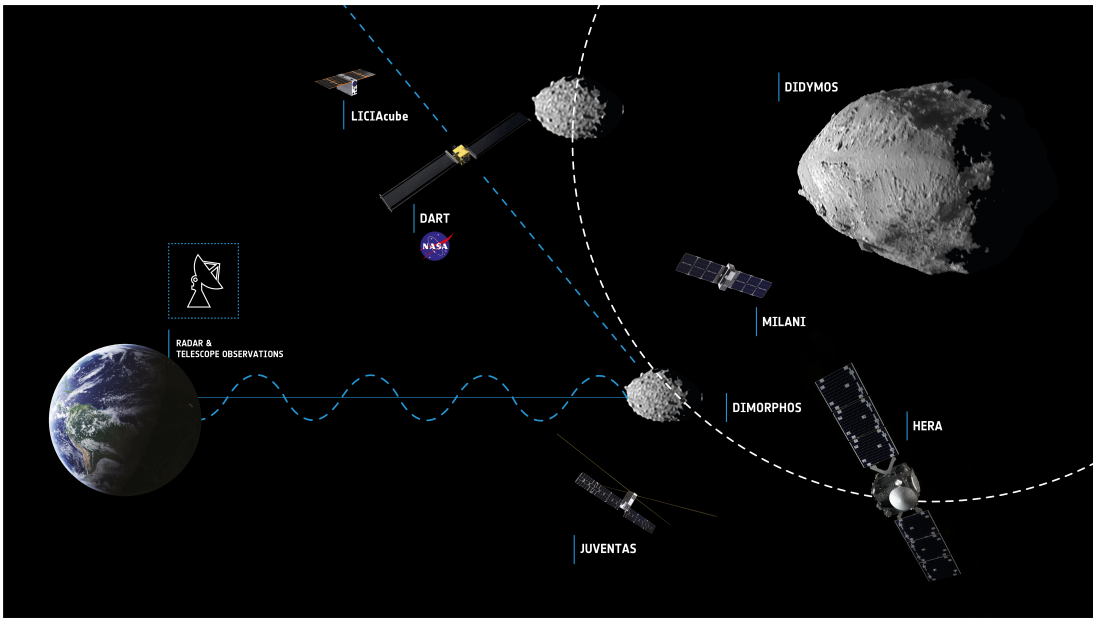


Figure 1.3: Infographic of DART and Hera missions. Courtesy: ©ESA/scienceoffice.

mission is the ESA contribution to the AIDA collaboration. It is currently in phase D,

with its launch scheduled in October 2024 and rendez-vous with the Dydimos system in December 2026 (fig. 1.4). The mission scientific objective is the detailed characterization of the binary asteroids, with particular focus on the properties and interior structure in an extremely low gravity environment.
As consequence, demanding requirements are imposed in terms of Operations, GNC capabilities and close approach trajectories. Additionally, similarly to DART, Hera is a mission of opportunity to demonstrate autonomous GNC technologies deemed as enabling of future missions to small bodies in general, starting from the first-ever rendez-vous and orbiting (on hyperbolic trajectories) of a binary asteroid system [31].

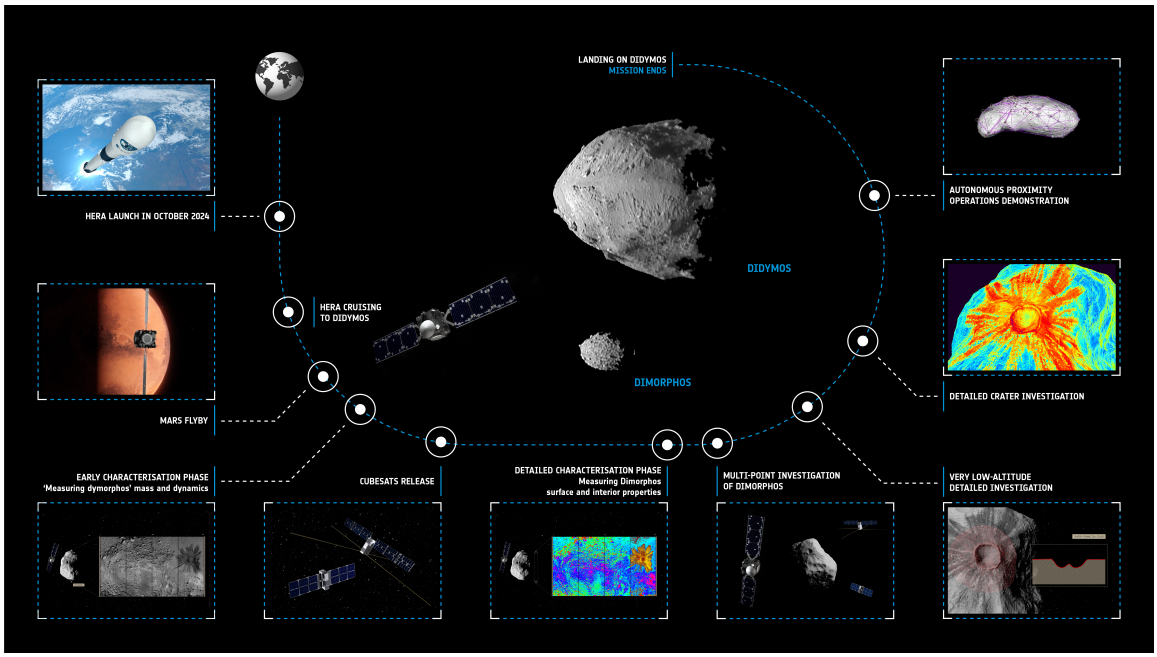


Figure 1.4: Hera high-level mission timeline. Courtesy: ©ESA/scienceoffice.

## 1.3. Overview of Hera Close Proximity Operations

Once the rendez-vous phase concludes in approximately 8 weeks, the close-proximity operations are structured to nominally extend over 22 weeks. These are allocated among three nominal mission phases along with an experimental one. Throughout this duration, there will be a progressive enhancement in on-board autonomy coupled with a reduction in the distance from the asteroid [24, 60]:

1. **Early Characterization Phase (ECP)/Payload Deployment Phase (PDP)** (6+2 weeks): Hera will operate outside the Sphere of Influence (SOI) of Didymos ranging from 20 and 30 km. It will fly two distinct types of hyperbolic trajectory

arcs, categorized as "short" and "long" each lasting 3 and 4 days respectively. This Mission Analysis (MA) requirement applies across all nominal mission phases, intended aligning the SC trajectories with Ground Operations scheduling. The ECP is of paramount importance to enhance the knowledge of the thermal and dynamical parameters of the system, facilitating the reduction in the flybys distances as well as the planning of the subsequent phases. According to the current operational timeline, a two-week duratin is allocated for the deployment of the two Hera cubesats, Juventas and Milani, from the same ECP trajectories. As of August 2023, Hera is foreseen to operate with an E2 level of autonomy (fully controlled by ground) during this phase. The exception is the rehearsal of the GNC functionalities, a necessary step to verify the subsystem's correct functioning.

2. **Detailed Characterization Phase (DCP)** (4 weeks): The trajectories of the DCP will span distance from 8 to 20 km increasing the coverage of the surface through diverse flyby geometries compared to the ECP. The ADCS is engineered to provide fully autonomous pointing to the Asteroids, whereas the Navigation, which remains ground-based, will exploit the image acquisition of the Asteroid Framing Camera (AFC) on the primary asteroid.

3. **Close Observation Phase (COP)** (6 weeks): during the Close Observation Phase, the spacecraft will follow the same trajectory geometries as the DCP, but further reducing the minimum distance down to 4 km. The first close flybys of the secondary asteroid will be conducted to cover a large portion of its surface while targeting the DART impact site. To allow the pointing of the paylods, the spacecraft will partially navigate relative to Dimorphos, with the altimeter becoming operational below approximately $\sim 15$ km. The ADCS will operate in a fully autonomous mode similarly to the DCP.

4. **Experimental Phase (EXP)** (6 weeks): the Experimental Phase serves as the culminating "risk-taking" segment of the mission, during which the full autonomy of the GNC will be demonstrated. Hera will achieve closest approaches at $\approx 1.3$ km from Didymos and at mere *hundreds* of meters from the surface of Dimorphos (Very Close Flybys (VCFB)). As the spacecraft approaches within about 2.5 km, the GNC will transition to utilizing Feature Tracking (FT) for relative navigation with respect to Dimorphos. This transition is necessary due to the complete filling of the navigation camera's Field of view (FoV) by the asteroids. A thorough description of the trajectory, perturbations and navigation architecture is provided in chapter 3.

## 1.4. Motivation and outline of the work

The final phase poses the most tough challenge from the GNC perspective: Hera will operate in a configuration characterized by almost full on-board autonomy. The ADCS will function autonomously across all its capabilities. The Orbit Determination and Control System is designed to be semi-autonomous for the translational guidance while maintaining full autonomy for other functionalities. The term "semi-autonomous" implies that the nominal Delta-V (DV) of the manoeuvres will be provided as time-tagged commands from the Ground Flight Dynamics plan. However, in contrast to earlier phases, the on-board guidance algorithms will be active during the EXP. Specifically, a manoeuvre correction term $\delta\mathbf{v}$ will be computed based on the estimated state $\hat{\mathbf{x}}(t_{man})$ at the manoeuvre times as provided by the Navigation functionalities (Autonomous Translation Control Manoeuvres (ATCM) [60]).

$$\Delta\mathbf{v} = \Delta\mathbf{v}_{nom} + \delta\mathbf{v}_{autoguid}$$

This feature is designed with the scope of letting the spacecraft perform the re-targeting manoeuvres to achieve a minimum Distance of Closest Approach (DCA) closer than what ground-based planning permits. In fact, the additional trajectory dispersion introduced by Ground-in-the-loop operations and the uncertainty associated with maneuver execution undermine the feasibility of performing such very close flybys without on-board autonomy.

An additional rationale to seek such developments in spacecraft autonomy lies in the current trend of the Space industry for both near Earth and Deep Space applications. Smaller spacecrafts such as CubeSats, including potential formation flying applications [9], enhance the capability of performing technological demonstrations and scientific missions, simultaneously paving the way to higher risk-taking missions. On the other hand, the continuously growing number of missions determines an excessive burden on Ground Control Operations [53], which has been traditionally a cornerstone for large missions since the early years of the Space Age. At the same time, it imposes additional constraints on the GNC and mission costs.

In this context, it is thus deemed advisable to augment the GNC functionalities with equally autonomous Failure Detection and Isolation (FDI) on-board algorithms, capable of detecting and suggesting actions to the OBSW should any error or failure arise during the operations. Additionally, considering the spacecraft's autonomy in modifying its trajectory and the relevance of thrust errors or failures in low-gravity environments, the FDI should include algorithms for trajectory safety. These are intended to monitor the GNC performance and ensure timely detection of any out-of-nominal collision risk. Such

features are deemed as critical for future mission to seek even increased autonomy and closer observations beyond the capabilities of the current state-of-the-art [31].

**Thesis outline** This document is structured as follows:

- Chapter 2 provides an overview of the current state-of-the-art of interplanetary missions in terms of Flight dynamics and operations. Recent advancements of the topics forming the key ingredients of the presented methods are reviewed and commented as well.
- Chapter 3 poses the basis of the work by framing its context in terms of the asteroid dynamical system, Hera GNC design and simulation models. All the relevant details for the design choices are highlighted.
- Chapter 4 is dedicated to describe the developed approaches in detail, emphasizing their assumptions and possible limitations.
- Chapter 5 contains the validation and a preliminary performance assessment of the methods in the simulation scenario. A thorough analysis moving from the considerations in chapter 4 is provided.
- Chapter 6 closes the work to summarize all the findings and offers considerations about future development paths.

# 2 | Survey of current operational paradigm and methods

This chapter offers an overview of the current state-of-the-art of interplanetary missions focusing on Flight dynamics and operations. It highlights the prevailing paradigm in terms of trajectory safety. The review briefly covers collision assessment methods commonly used for artificial objects in Earth orbits, particularly those applied in Space Situational Awareness applications. The objective is to assess their adaptability to the Hera mission scenario and their feasibility for on-board execution. Additionally, uncertainty propagation methods are presented as relevant elements in the context of filtering and estimation.

## 2.1. Mission to small bodies: trajectory safety-by-design approach

The number of interplanetary missions that visited small bodies in the past decades is relatively limited even when including missions such as Deep Impact and DART [16]. In fact, the objective of the latter two was not to rendez-vous and orbit the body, but to target and impact it. Among these, Rosetta, Hayabusa 2 and OSIRIS-REx stand out as significant contributors to the study of asteroids and comets in the Solar System as well as for the innovative technologies they required and the derived Lessons learnt. An intriguing aspect is that each visited small body target has showcased the diverse and unpredictable nature of this class of objects. Factors such as mass, shape, physical properties, gravitational field, and the presence of dust or smaller orbiting objects introduce uncertainties, necessitating mission margins and careful operational planning.

**Rosetta** Rosetta [32] was a cornestone ESA mission of the Horizon 2000 program, targeting Comet 67P/ChuryumovGerasimenko. For the first time ever, it successfully characterized the nucleus of a comet with global coverage, determining its dynamic properties, morphology and composition. Rosetta also carried the small lander Philae for in-situ

study of the surface. Scientific objectives included studying cometary activities such as outgassing and investigating the interaction with the solar wind. The challenging environment and behavior of comets posed unique considerations for the design of Rosetta's trajectories and GNC. The early characterization was conducted by flying three segments of hyperbolic arcs at distances ranging from 115 to 90 km, known as "Pyramid Orbits" [2], that ensured Rosetta to remain on the illuminated side of 67P. Once the shape model and comet parameters were sufficiently estimated (with accuracy up to 200 meters for the former), the spacecraft was moved to closed orbits at about 29 km and 60° inclination away from the Sun direction. Later in the mission, terminator plane orbits at about 19 km were exploited.

**Hayabusa 2** The Hayabusa 2 is the JAXA second sample return mission to "1999 JU3 Ryugu" [71], a C-type asteroid of interest for the plausible presence of organic matter and hydrated minerals. The spacecraft reached Ryugu in June 2018, where all the planned operations, including sample return and kinetic impactor test were performed. The return flight began in November 2019, ending with the delivery of the sample capsule in 2020. Currently, an extended mission phase is underway.
The operations planning for Hayabusa 2 was performed in three scenarios considering three different values of the asteroid gravitational parameter [64], with significant uncertainty in the spin axis prior arrival. Peculiar with respect to other missions, Hayabusa 2 did not fly orbits around Ryugu but exploited three main hovering points (HP) between 5 and 20 km distance. Station keeping $\Delta\mathbf{v}$ were necessary every one or two days, based on ground planning. During touchdown operations from the hovering points, the spacecraft followed a pre-computed nominal descent trajectory. Navigation was primarily conducted on Ground every 10 minutes. At approximately 50 meters, the fully *automatic* control phase was set to begin, still following pre-stored commands. Gate points were positioned along the trajectory, allowing the Ground segment to verify the spacecraft status before proceeding. Contingency planning and FDI were limited to the definition of conditions causing the spacecraft to either switch to redundant units or trigger the abort mode.

**OSIRIS-REx** The OSIRIS-REx mission [42] is an asteroid sample return mission of the NASA New Frontier program to the near-Earth asteroid (101955) Bennu. Successfully reaching its target in November 2018, the mission aimed to globally characterize Bennu and acquire a minimum of 60 grams of asteroid regolith. The touch-down for the sampling operations was performed in October 2020, resulting in the collection of a significantly higher-than-expected amount of material. The sample return capsule was successfully delivered by the spacecraft and landed intact on 24 Sept. 2023 in Utah's Great Salt Lake

Desert [54].
The close proximity operations [79] planning was designed to rely on radiometric navigation data during the first survey phase, gradually moving to optical landmark-based navigation as the spacecraft started to fly closer orbits [6]. Hyperbolic flyby arcs started at $\approx 7$ km distance, then moved closer down to 3 to 5 km range. Bennu's mass and shape allowed closed orbits to be design at distances lower than 2 km after the first Detailed Survey Phase. Specifically, Sun terminator frozen orbits were chosen to be flown during the Orbital A phase. For safety reasons, weekly scheduled orbit trims were planned in case OSIRIS-REx would have entered an unstable or incorrect orbit. However, none was actually exercised [6]. The subsequent Detailed Surveys again employed hyperbolic arcs reaching distances down to 650 and 250 meters during the site selection campaign.

**The current paradigm** Previous interplanetary mission to small bodies tackled the safety problem relying on Ground Flight Dynamics and planning: ensuring safety through conservative margins validated by covariance and Monte Carlo analyses of various mission scenarios and uncertainties [79].
Hyperbolic flybys are preferred for their enhanced safety as collision with the main attractor is impossible unless an unexpected event occurs. Terminator orbits are also particularly relevant for low-gravity environments thanks to their self-stabilizing property with respect to SRP. However, they suffer from poorer Sun illumination. For instance, Hera will not exploit this class of orbits unlike Juventas, whose main instrument is in fact a radar [33]. Finally, the threat posed by failures during thrusting manoeuvres at the "corners" of hyperbolic arcs may even further mitigated by the adoption of the so-called "dog-leg" strategy.
Trajectory re-design is iteratively performed through the close proximity operations phase, based on the most recent batch of received data after data cut-off. This imply that the trajectory and the related uncertainties must be predicted forward for periods longer that 24 hours. In fact, as a consequence of the low-gravity environment, subtle perturbations (e.g., SRP, thermal re-radiation of the spacecraft and reaction wheels unloadings) can completely change the trajectory of the spacecraft even imparting very low $\Delta\mathbf{v}$. For instance, [79] reports that a 2 cm/s change in velocity around Bennu could determine a change in the pericentre of more that 500 m.
While the current paradigm has proven effective, an autonomous spacecraft capable of detecting collision risks in the presence of uncertainties could significantly reduce the time and costs associated with early characterizations. This increased tolerance to dynamical uncertainties enhances spacecraft safety and allows for missions, particularly smaller and lower-cost ones, to accept lower margins in Flight Dynamics planning while relying more

on the spacecraft's self-guarding capabilities [31].

**Hera mission approach** As mentioned in chapter 1 and detailed in chapter 3, the Hera mission is pioneering in several aspects, one of which is its ability to determine trajectory safety "online". The on-board trajectory safety FDI will be tuned and enabled by ground when COP and EXP trajectories will be flown below 15 km. Notably, the latter phase foresee no ground contact during the entire operation until after the pre-scheduled third "comeback" manoeuvre.
In this regard, no other prior investigation seems to exist or at least to be publicly available in the literature. However, various methods have been developed for ground-based applications to assess conjunctions between artificial satellites in the field of SSA.

## 2.2. Methods of collision assessment between Earth orbiting objects

The simplest method to evaluate the collision risk involves the computation of the miss distance $r_{CA}$, representing the minimum relative range between two objects. In fact, in the early years of Space Situational Awereness (SSA) field, this metric was used to assess the probability of collision during closest approaches between satellites orbiting the Earth [72]. Under the Gaussian distribution assumption, the PDF of the estimated $\hat{r}_{CA}$ can be characterized in terms of its mean $\mu_{\hat{r}_{CA}}$ and variance $\sigma^2_{\hat{r}_{CA}}$. Therefore, the state covariance information must be propagated along with the mean estimate. it's worth noting that when dealing with large propagation times *without* measurements, the Gaussianity assumption may become invalid due to non-linearities in the dynamics [81].

### 2.2.1. Probability of Collision-based approaches

**Definition and assumptions** When the absolute position vectors of the two objects $\mathbf{r}_{obj1}$, $\mathbf{r}_{obj2}$ with the associated covariance matrices $P_{rr_{obj1}}$, $P_{rr_{obj2}}$, are fully known and independent, the most general expression for the cumulative probability of collision involves the first three dimensional integral (2.1) of the state PDFs, which is time-varying [44].

$$P_c = \int_{t_{start}}^{t_{end}} \int_V p\left(\mathbf{x}, t; \mathbf{r}_{obj2} - \mathbf{r}_{obj1}, P_{rr_{obj1}} + P_{rr_{obj2}}\right) dV\, dt \tag{2.1}$$

where each of the objects are characterized as spheres with hard body radius $R_{hb}$, and $V$ is the volume of the combined ellipsoid centred in one of the two objects.
Methods to approximate the computation of eq. (2.1) with a very high accuracy are all

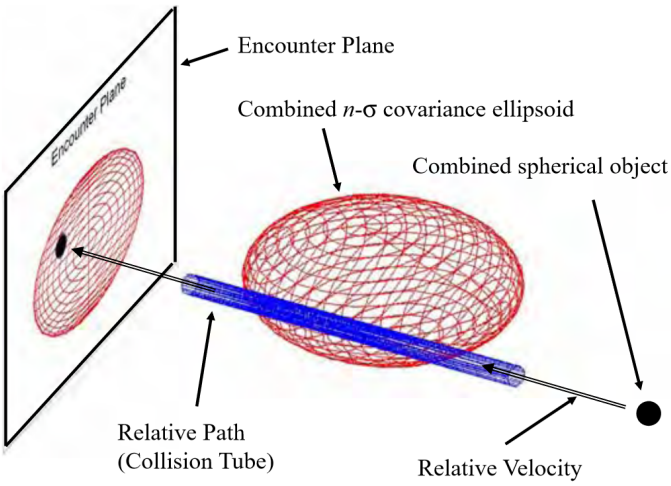


Figure 2.1: Conjunction projection on the Encounter plane. Reproduced from [72].

variants of the Monte Carlo method [44]: $N$ samples of the state vectors are generated from the assumed distributions and propagated until the nominal time of the encounter. The probability is estimated in the classical sense $P_c = N_{collisions}/N_{total}$, where the numerator is the number of samples that led to a collision.

Most of the methods available in the literature [44] simplifies the formulation by assuming:

1. All the random variables distributed as Gaussian variables.
2. The encounter occurs at very high relative velocity (Short encounter assumption) with a negligible velocity uncertainty

The short term encounter assumption has been proved to hold when the magnitude of the relative velocity is in the order of several $km/s$, such that the encounter lasts tens of seconds at most. This simplifies the integral [20], while also making the computation less costly. A comparison of computational times is shown [44].

**Computational methods** Numerous methods have been developed to compute it either analytically or numerically [4, 44, 65], with some of them being actively used in operational scenarios [19, 72]. A key point to highlight is that in principle, all of them address a general problem: estimating the probability of the combined covariance ellipsoid (assuming uncorrelation between the two objects) intersecting a sphere with a radius equal to the sum of the hard body radii. The first ellipsoid is centred in the primary object, the sphere in the secondary object. The "Short encounter" assumption simplifies the problem by projecting both in the encounter plane (hence, the reduction to a 2D integral, fig. 2.1). In contrast, "Long encounter" methods make no assumptions in this

regard and considers the time evolution of the state PDF over the encounter period.
One limitation of these methods is that the hard body radius of both objects must be small, at least compared to the covariance ellipsoid. For instance, the method proposed by [65] can even return a solution that neglects the hard body radius altogether.
On the other hand, methods for long term encounters are more general, but less common and developed for two reasons:

1. Most of the encounters in Earth orbits are well modeled as "short".
2. The computation time is excessive to be performed on a very large number of objects conjunctions.

The endpoint of all these methods is the use of the PoC estimate for a collision avoidance manoeuvre decision problem. To date, this step involves a decision either made by human operator or threshold-based.

### 2.2.2. Hypothesis testing-based approaches

Alternative approaches to the CAM decision problem were proposed by [12–14]. Instead of focusing on the accurate computation of the PoC and threshold-based decisions as seen in the majority of the Literature, a Sequential Probability Ratio Test (SPRT) is employed to drive the decision based on hypothesis testing, i.e., evaluating which of two hypothesis better explains the available information. The Innovation PDFs of two inequality constrained filters estimating the relative state vector of two artificial objects are compared. The filters bank is guided by a third unconstrained filter which executes a preliminary screening, computes the nominal time of closest approach of the conjunction and performs measurements editing if needed.
A constraint enforcement is performed on the PDF of the two filters at each Observation Update. Specifically, the constraint directly corresponds to a hypothesis in the binary inferential test, either $H_0$ or $H_1$, respectively the Null and the Alternative hypothesis. Therefore, the hypothesis define two complementary partitions of the state space separated by the constraint manifold that distinguishes them. All the mentioned works take advantage of the Wald SPRT.
This test was also evaluated as decision-making scheme for the CAM decision problem of the OSIRIS-REx mission [49], in the hypothetical scenario of the discovery of a secondary body around Bennu. In fact, OSIRIS-REx was planned to exploit Sun Terminator orbits, where the stability of the orbit of natural objects is higher. The characteristics of the Wald SPRT are utilized similarly, assessing the test outcomes for various false alarm and missed detection probability targets. The analysis revealed that having low desired probability

targets does not equate to a good decision-making strategy and that it is challenging to find the correct balance between these two tuning parameters.

**Wald Sequential Probability Ratio Test (SPRT)** The Wald Sequential Probability Ratio Test is a method proposed by [77] to drive the decision in binary inferential tests in a sequential manner. Two mutually exclusive hypothesis, conventionally indicated as Null $H_0$ and alternative $H_1$, are compared based on the Likelihood ratio of the PDFs of the random variables associated to the observations, conditioned to the hypothesis and to the available realizations. The sequential nature of the method lies in the fact that the Likelihood ratio is updated sequentially each time a new realization is available. For this reason, there are three possible outcomes:

1. $H_0$ is rejected, and $H_1$ accepted.
2. $H_1$ is rejected, and $H_0$ accepted.
3. The test suggests to wait for additional observations, because of the uncertainty in the decision.

Conversely, non-sequential tests are performed on batch of measurements and their outcome is always the rejection of the less supported hypothesis, relying on the currently available realizations.
An additional difference lies in the number of observations used by the two approaches: the WSPRT takes into account as many observations as needed to attain a decision, meaning that this number is not determined prior the experiment, but only during its execution; on the contrary, the non-sequential approaches require the prior specification by the user.
Finally, the WSPRT provides guarantees of accuracy in terms of the false alarm (fa) and missed detection (md) specified in the experiment thanks to the fact that the decision bounds are directly related to the former parameters. In other words, the user can specify the accepted values of the probability of obtaining an incorrect decision determining the bounds of the Likelihood ratio driving the test. This, in turn, determines when and which decision is made For these reasons a sequential scheme to conduct binary hypothesis testing is naturally more suitable for "on-line" applications.

**Types of inference errors** In binary Inferential statistics two type of errors are commonly defined: Type I error and Type II error, easily explained by table 2.1, depending on which hypothesis is the "true" one and which the test indicates as refused. The probability of false alarm and missed detection are thus the probabilities associated to the

Table 2.1: Truth table of inferential errors.

| Decision | Null $H_0$ True | Null $H_0$ False |
|---|---|---|
| $H_0$ not rejected | Correct decision | Type II error (false alarm) |
| $H_0$ Rejected | Type I error (missed detection) | Correct decision |

test rejecting the Null (i.e., "default") $H_0$ hypothesis in case it is true and the test not rejecting it when false, respectively. Casted in the collision assessment problem, the $H_0$ is associated to the case where the conjunction is not safe and thus a CAM is required. The false alarm in fact corresponds to the CAM being performed without real need; the missed detection to the case in which the collision risk is discarded even if the conjunction is truly unsafe.

**Filters bank implementations** Two types of filters implementations were proposed, given that the time instant at which the constraint has to be enforced (i.e. the time of the conjunction) is strictly posterior to any of the available measurements. Reference [12] describes both in detail, building upon previous work.

- **Epoch-state** estimators: the inequality constrained filters perform the measurement incorporation by updating the state at a fixed epoch, which is the constraint time (closest approach). Therefore, the constraint enforcement does not need to be propagated backward to the current state. The constraint enforcement is addressed by augmenting the state vector through a slack variable, modifying the cost function that the estimator minimizes to account for the constraint manifold.
- **Current-state** estimators: the filter progresses forward in time through the conventional Time and Measurement update cycles. The constraint at the future epoch must be therefore mapped to the current time. A sigma point projection (fig. 2.2) combined with Lambert-like Differential correction of the current-state velocity is employed to map the constraint.

The presented methods were based on a pair of Extended KF designed to work with a full covariance matrix. The authors suggested that UKFs could be more suitable for the application of the Sigma point projector, starting from the Sigma points the filter uses. However, this would not avoid a third Cholesky decomposition if the full covariance is used in the UKF as well. A Square-Root form [28, 75] seems the most convenient implementation from a computational standpoint.

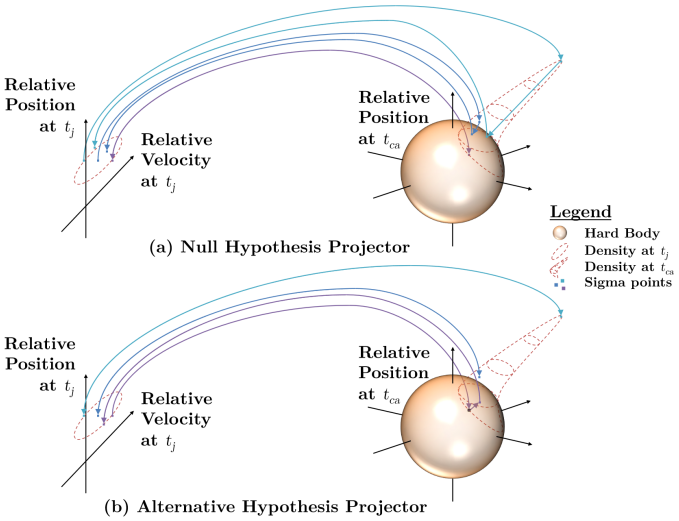


Figure 2.2: Sigma Points projection representation. Reproduced from [11].

## 2.3. Uncertainty propagation and filtering methods

**Linear Covariance and Sigma-Point transformation** In applications involving estimation methods, accurately quantifying the uncertainty of the estimated quantity is crucial. When dealing with conjunctions assessment, accuracy in predicting both mean and covariance is even more critical for ensuring spacecraft safety. Among the exist-

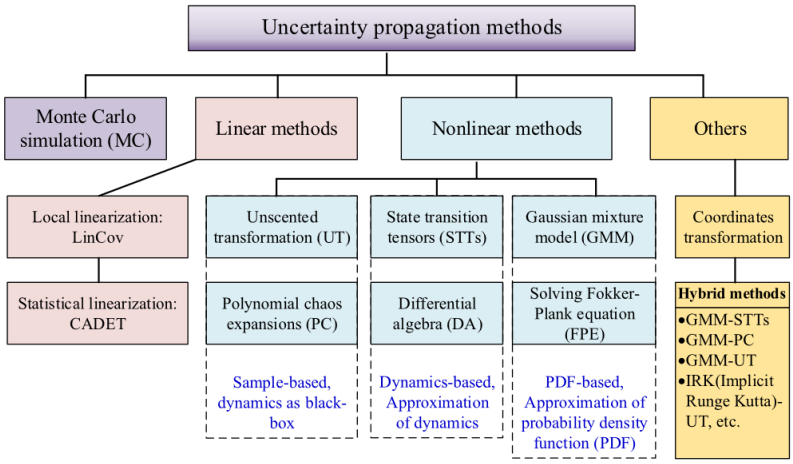


Figure 2.3: Overview of Uncertainty propagation methods reproduced from [46].

ing methods shown in figure 2.3 [46], two of them are commonly employed in on-board applications, both relying on the Gaussian distribution assumption.

1. **Linear covariance**: the propagation of the covariance through a generic map $\mathbf{y} =$

$\mathbf{f}(\mathbf{x})$ is performed through its linearization with respect to the state vector ($1^{st}$ order truncation of the Taylor series of the function), only requiring the jacobian $\nabla f$ computed with respect to the inputs $\mathbf{x}$. The mean is non-linearly mapped through the function. In the case of dynamical systems governed by a set of ODEs, the Error State Transition matrix $\Phi(t_k, t_k + 1)$ linearly maps any state deviation $\delta\mathbf{x}$ from the mean $\hat{\mathbf{x}}$ from time $t_k$ to time $t_{k+1}$ (2.2).

$$P_x(t_{k+1}) = \Phi(t_{k+1}, t_k) P_x(t_k) \Phi(t_{k+1}, t_k)^T \tag{2.2}$$

2. **Sigma Point-based** methods employ deterministic sampling of the state PDF to generate a discretization in terms of the so-called sigma pointsenabling a full capture of covariance information. Among the different methods, the Unscented Transform [37, 39, 40] is a widely used approach due to its simplicity and a good balance between accuracy and computational cost. Nevertheless, the basic principle is the same for all the methods: each point, regardless of how they are generated (where the methods differ) are mapped through the non-linear function. The reconstruction of the first two moments is then performed by weighted sample mean and covariance. The Scaled Unscented Transform algorithm is reviewed below (2.3.1).

Indeed, both approaches have non-negligible drawbacks. Linear Covariance is known to suffer from accuracy loss when long time propagation through non-linear dynamics is performed, typically leading to an underestimation of the covariance. Additionally, the linearization error in the first moment can be significant [74]. In fact, these are the main reasons of the increased robustness and accuracy of Sigma Points estimators [61]. Despite having the same algorithmic complexity, Sigma-Point based methods are more costly due to the need of applying the non-linear functions to every Sigma-points, whose number rapidly grows with the state vector size. Moreover, they can fail in case of nearly singular covariance matrices, incorrect scaling parameters [82] and single-precision arithmetic (as the weights can be very large).

**High-order methods** High-order methods offer enhanced accuracy and realism of the uncertainty propagation in case of highly non-linear dynamical systems. In fact, their main advantage is the ability to capture high-order moments and/or Non-Gaussian distribution of the state PDF.
State Transition Tensors (SST) and Differential Algebra (DA) are the two most promising for on-board application, whenever Linear Covariance and Sigma points methods do not suffice (e.g., when long measurements outages occur). To date however, they still suffer

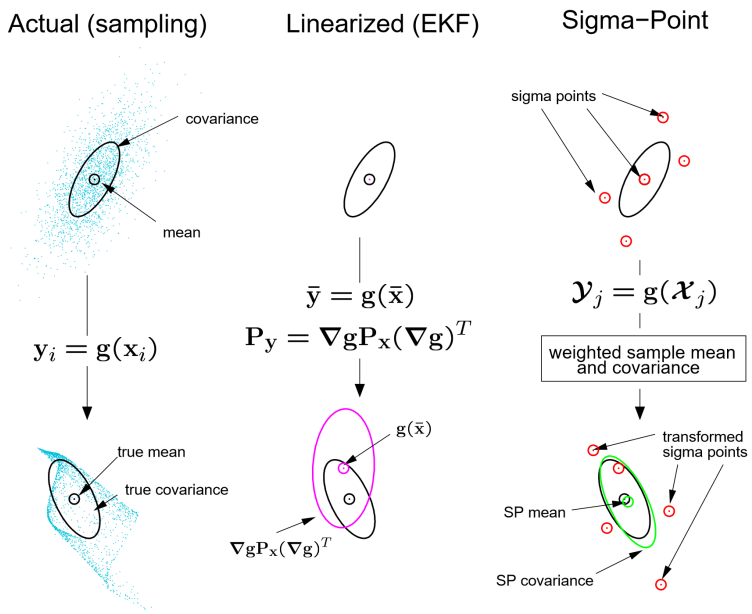


Figure 2.4: 2D representation of Linear Covariance and Unscented transformation, compared to samples propagation (MC). Reproduced from [74].

from the unsustainable computational burden.

The former technique was first proposed by [56] and applied to filtering problems in [57]. It enables uncertainty propagation by solving for the higher order Taylor series terms of the flow function. Direct integration of the Variational equations involves a number of equations which exponentially increases with the order, rendering on-board implementation troublesome. Automatic differentiation (e.g., [27]) may provide a sufficiently reliable and fast on-line computation of the SST.

Differential Algebra is at its core a technique that allows the approximation of the flow function directly as its Taylor series, computed exploiting Taylor Algebra in a computerized environment. In other words, it can be interpreted as an alternative computation method for the State Transition Tensor. In [22] a feasibility assessment with processor-in-the-loop simulations of the DACE library [50] was conducted for the ESA Advanced Concept team, providing evidence that the computational cost may be acceptable under some conditions. The work however has some limitations: it did not include process noise; the state vector was relatively small with respect to real applications, where techniques such as Dynamical model compensation [70] are necessary. In this regard, it should be noted that DA does not scale well: the computational cost rapidly scales up with the state vector size and Taylor series order.

Several filtering methods have been developed in [73] which fully exploit DA for non-linear propagation in both the Time and the Measurement Update, yet keeping the linear

estimator structure of the Kalman filtering. In [66] a further extension to non-linear estimators is demonstrated to attain improvements in accuracy at the expense of increased computation time. Finally, the analytical approximation of the Taylor map provided by DA can also be exploited for the solution of targeting problems [45] and as auxiliary tool for Sigma-point projections.

### 2.3.1. Unscented Transform

The Unscented Transform (UT) is the most used transformation in Literature. The algorithm for the generation of the Sigma Points and the uncertainty propagation is hereafter reported. The scaling parameters can be set equal to the typically adopted values [75]. $N_z$ is the size of the state space; $\alpha$ determines the spread of the Sigma points;

Table 2.2: Scaling Parameters of the Unscented Transform used in this work.

| | |
|---|---|
| $\alpha$ | $1 \times 10^{-4}$ |
| $\beta$ | 2 |
| $\kappa$ | 3 - $N_z$ |

$\beta = 2$ is optimal for Gaussian distributions; finally, the expression of $\kappa$ guarantees that the error in capturing the higher order moments is minimized. The number of Sigma points is equal to $N_\chi = 2N_z + 1$ since two sigma points per dimension of the space are required, plus the mean state.
The perturbation coefficient to scale the columns of the Square Root covariance matrix for the Sigma points generation is then computed (eq. (2.3)).

$$\lambda = \alpha^2(N_z + \kappa) - N_z\,; \qquad \eta = \sqrt{N_z + \lambda} \tag{2.3}$$

Finally, the Square Root covariance matrix $S_{\mathbf{zz}}$ is computed by decomposing the full covariance $P_{\mathbf{zz}}$ (e.g. using Cholesky decomposition):

$$S_{\mathbf{zz}} = \texttt{Chol}\,(P_{\mathbf{zz}}) \;\Rightarrow\; P_{\mathbf{zz}} = S_{\mathbf{zz}} S_{\mathbf{zz}}^T \tag{2.4}$$

The Sigma points are generated by perturbing the mean state vector $\hat{\mathbf{z}}$ using the scaled columns of $S_{\mathbf{zz}}$ in two "directions" per each axis of the state space (eq. (2.5)). The set "-"

corresponds to the Sigma points parameterizing the distribution to propagate [38, 67, 75].

$$\begin{cases} \boldsymbol{\chi}_0^- = \hat{\mathbf{z}}^- & \\ \boldsymbol{\chi}_i^- = \hat{\mathbf{z}}^- + \eta \left[S_{\mathbf{zz}}\right]_i & i = 1, ..., N_z \\ \boldsymbol{\chi}_i^- = \hat{\mathbf{z}}^- - \eta \left[S_{\mathbf{zz}}\right]_{i-N_z} & i = N_z + 1, ..., 2N_z \end{cases} \tag{2.5}$$

Given a generic non-linear function $\mathbf{y} = \mathbf{f}(\mathbf{x})$, the uncertainty propagation through the latter is simply performed by evaluating the function in the Sigma points:

$$\boldsymbol{\chi}_i^+ = \mathbf{f}(\boldsymbol{\chi}_i^-) \qquad i = 0, \ldots, 2N_z \tag{2.6}$$

The set "+" corresponds to the Sigma points parameterizing the propagated distribution, whose mean and covariance are recovered by the weighted sample mean and covariance operators (2.7, 2.8).

$$\hat{\mathbf{z}}^+ = \sum_{i=0}^{2N_z} W_i^{(m)} \boldsymbol{\chi}_i^+ \tag{2.7}$$

$$P^+ = \sum_{i=0}^{2N_z} W_i^{(c)} \left(\boldsymbol{\chi}_i^+ - \hat{\mathbf{z}}^+\right) \left(\boldsymbol{\chi}_i^+ - \hat{\mathbf{z}}^+\right)^T \tag{2.8}$$

## 2.4. Research Question

The present work aims at answering the following main research question in the context of the Hera mission scenario:

*From a Navigation standpoint, which are possible methodologies to autonomously assess the safety of the trajectory of the spacecraft?*

Several sub-questions are then derived, specifically addressing the main features the algorithms should possess:

1. To what extent is it possible to provide this assessment ***independently*** from the Navigation filter?
2. Which models may be compatible with the requirement of low computational cost necessary for FDI routines?

# 3 | Didymos system and Hera GNC: description and analysis

This chapter is dedicated to offering a more detailed context for the work, starting from an analysis of the dynamics within the double asteroid system. A high-level description of the navigation architecture and of the Hera GNC simulator is provided to let the reader understand the dataset utilized in the analysis. Emphasis is placed on highlighting details influencing the design choices made.

## 3.1. Baseline EXP trajectories

### 3.1.1. GNC and trajectory constraints

The Experimental phase has the main purpose of demonstrating several GNC technologies that will significantly contribute to more autonomous missions in the future. Additionally, it aims to collect high-resolution observation data of the DART impact and the Dimorphos surface from various viewing angles. The key elements of this phase include:

- Autonomous navigation based on line-of-sight and feature tracking technologies, including altimeter measurements for enhanced observability of the position states.
- Semi-autonomous trajectory guidance to achieve controlled passages near the target bodies, targeting a pre-specified state vector, based on the information obtained through the autonomous navigation.
- Autonomous attitude GNC in a loosely coupled configuration with the translational GNC.

In fact, Hera will operate with an E3 level of autonomy (as defined in [62]) for the entire GNC subsystem. This level of autonomy signifies that the spacecraft's on-board algorithms can independently adapt both attitude and orbit to fulfill specified mission objectives.

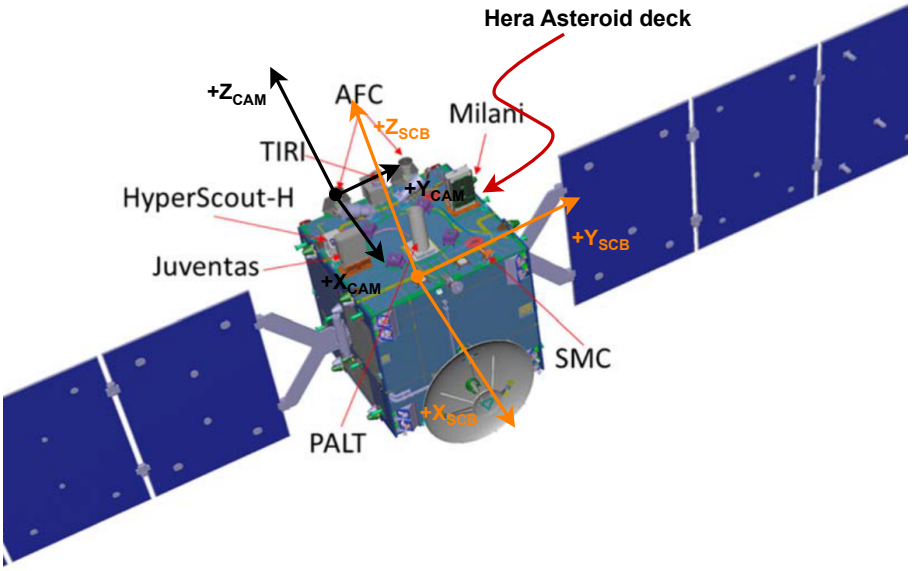


Figure 3.1: Hera +Z Asteroid deck with Spacecraft Body Frame SCB and Camera CAM frame orientations. Adapted from [24].

The design of Hera trajectories is subect to three major GNC constraints, namely:

1. The need of continuous pointing of the +Z Asteroid deck (3.1) where all the instruments are mounted, toward the target body. The -X axis shall remain in shadow throughout the trajectory for thermal control reasons.
2. The Sun Phase angle, defined as the angle between the Sun direction and the relative position between target body and spacecraft fig. 3.2, must be sufficiently high to ensure proper surface illumination for the image processing algorithms. Autonomous relative navigation would not be feasible otherwise.
3. The trajectory shall be hyperbolic at any time, with a velocity at closest approach lower bounded by the escape velocity considering both bodies as a single point mass, including a safety factor $C$:

$$v_{CA} = (1 + C)\sqrt{\frac{2\mu_{D12}}{r_{CA}}} \quad \text{where } C > 0$$

### 3.1.2. Reference frames and conventions definition

Several reference frames are used throughout the work. Their origins, orientations and nomenclature are thus here defined.

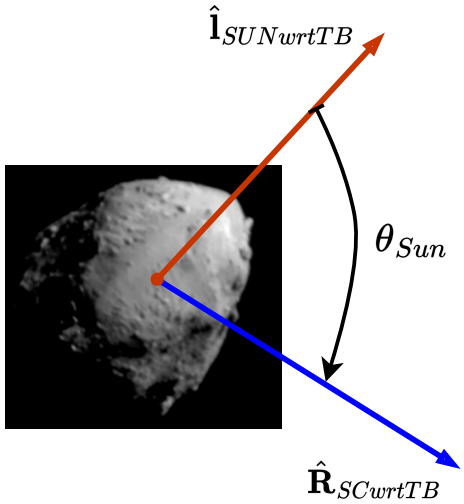


Figure 3.2: Definition of Sun Phase angle $\theta_{Sun}$.

1. **Central (Pseudo) Inertial: CI**. Centred in the CoM of Didymos (approximated as the CoM of the binary system). Axes aligned with ECLIPJ2000 reference frame.
2. **Target Body: TB**. Centred in the target (fixed) body CoM (i.e. +Z axis in the direction of the body spin axis and rotating with it).

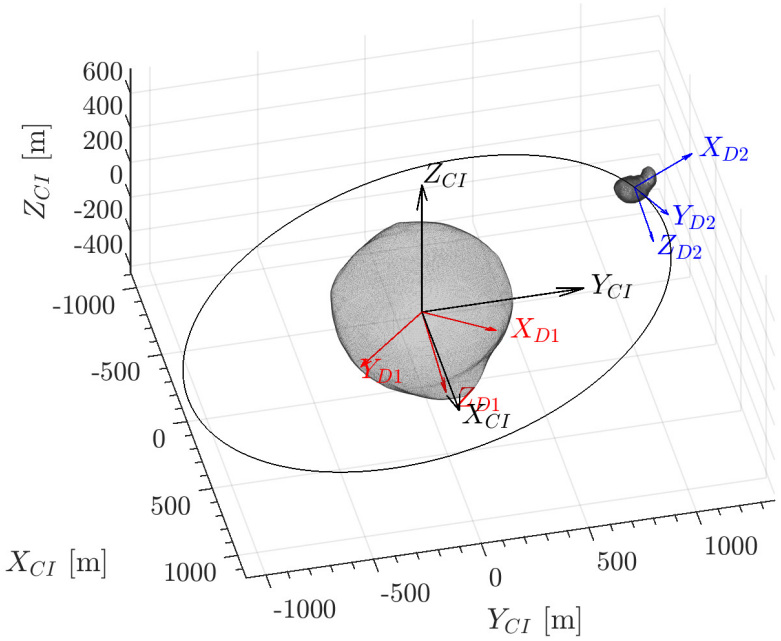


Figure 3.3: Central Inertial frame centred in Didymos CoM, aligned with ECLIPJ2000, and Target Bodies frames attached to D1 and D2 shape models at closest approach time.

3. **Spacecraft Body: SCB**. Centred in the spacecraft CoM. +Z axis is taken as the normal to the asteroid deck side; +X axis orthogonal to the side on which the High gain antenna in mounted. Y axis completes the triad and corresponds to the solar array drive mechanism axis (around which the array can rotate).

4. **Camera frame: CAM frame**. Centred in the spacecraft CoM. The camera +Z bore-sight axis coincides with SCB +Z axis. The remaining axis (X, Y) are aligned with the detector plane.

5. **Image plane**: coordinates of vectors in CAM frame defined by the pinhole model projection through the camera calibration matrix (3.7) and normalization with respect to the third component.

The JPL convention is adopted for quaternions [47], namely: $\mathbf{q} = \begin{bmatrix} \mathbf{q}_{vec}^T & q_{scalar} \end{bmatrix}^T$.
The following nomenclature is established for rotations parameters: $\mathbf{q}_{XwrtY}$ is the quaternion identifying the attitude of reference frame $X$ wrt to frame $Y$, thus corresponding to the DCM rotating a vector from frame $Y$ to frame $X$, $DCM_{XwrtY}$.

### 3.1.3. Trajectory and CAM strategy

An example of the first arc trajectory of the EXP phase with a duration of approximately 3.73 days, is depicted in fig. 3.4. The present work exclusively focused on the trajectory

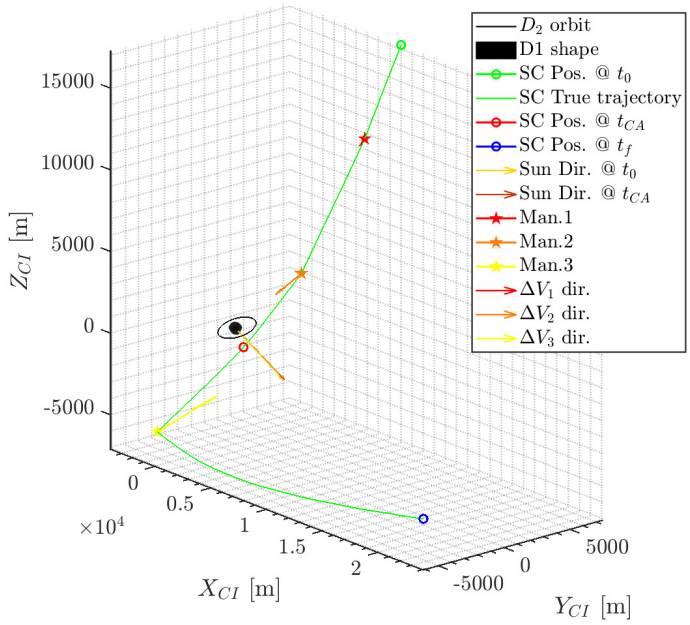


Figure 3.4: Hera EXP trajectory, D1 and D2 at $t_{CA}$ - Arc 1 @Didymos CI.

segment before the occurrence of the closest approach. The reason is rather straightforward: the detection of any trajectory safety issue *must* occur within the timeframe required for the spacecraft to perform a Collision avoidance manoeuvre (CAM). Additionally, running such FD algorithms after the CA is unnecessary since the hyperbolic arcs ensure that the spacecraft will move away from the system.
The CAM strategy adopted for Hera leverages the second constraint mentioned earlier: the Sun direction is inherently a safe direction to move toward. This direction's knowledge is consistently available at any given time through sun sensors, making the complete attitude reconstruction unnecessary. Consequently, the following operations are executed whenever an avoidance manoeuvre is initiated by the OBSW following the suggestion of the collision risk estimator (GNC-FDI, categorized as level-3, system-wide [62]):

1. The spacecraft GNC transitions to the CAM execution mode. All the autonomous functionalities are disabled and can no longer determine the spacecraft behaviour.
2. An attitude slew manoeuvre is performed to point the +X axis toward the estimated Sun direction according the predefined accuracy.
3. The thrusters are fired to impart a pre-defined $\Delta v$, computed such that the spacecraft is ensured to move away from the system in the Sun direction regardless of its position along the trajectory.

The described sequence of events requires a maximum time period of approximately 1 minute, which is sufficiently short to perform the manoeuvre even if the collision risk is detected shortly before the event. In principle, detecting it during the feature tracking navigation window would still be acceptable. However, this study concentrated on methods that solely utilize centroiding information due to the added complexity associated with the exploitation of the former.

## 3.2. Didymos dynamics and Hera DKE models

### 3.2.1. Dynamical and shape parameters

The parameters considered for the analysis are summarized in table 3.1 in which $(\beta, \lambda)$ are the Heliocentric latitude and longitude coordinates.

It is important to note that the provided values are subject to changes as new studies emerge in the near future. Several assumptions were made on the asteroid system modeling for this work:

- Dimorphos spin axis is assumed to be perpendicular to its orbital plane, aligned to

the its orbital angular momentum vector.

- The spin rate of Dimorphos is assumed to be synchronous with the orbital motion, such that it consistently points the same side toward Didymos
- Dimorphos shape could not be completely determined neither by Ground Radar observations nor by Space observatories. For Hera GNC development a 3D model of (25143) Itokawa (fig. 3.5) was utilized, scaling it according to the tri-axial size, with the purpose of better characterizing the GNC performance.

Table 3.1: Parameters of Didymos system for the simulation scenario.

| | | | |
|---|---|---|---|
| $R_{D1}$ | 386.67 $[m]$ | $\mu_{D1}$ | 35.7854 $m^3/s^2$ |
| $R_{D2}$ | 77.83 $[m]$ | $\mu_{D2}$ | 0.3328 $m^3/s^2$ |
| D1 $T_{spin}$ | 8136 $[s]$ | D1 $T_{orb}^{Helioc.}$ | 770 days |
| D1 Spin axis $\beta$ | $-87$ $[deg]$ | D1 Spin axis $\lambda$ | 270 $[deg]$ |
| D1 Perihelion | 1.014 $[AU]$ | D1 Apohelion | 2.275 $[AU]$ |
| D1 Orb. ecc. | 0.384 $[-]$ | D1 orb. incl. | 3.408 $[deg]$ |
| D2 $T_{spin}$ | 11.9216 $[hr]$ | D2 $T_{orb}$ | 11.9216 $[hr]$ |
| D2 orbit params | $\begin{bmatrix} 1063.8 \\ 0.1530 \\ 2.8240 \\ 2.9980 \\ -0.6133 \\ -2.8348 \end{bmatrix}$ [m, -, rad] | $t_0$ Epoch | July 2027 |

Lastly, it is worth noting that the successful impact of the DART spacecraft with Dimorphos [17, 63] already induced several modifications to the system. In particular, the dynamics of Didymos and Dimorphos changed as consequence of the mass and shape alterations of the secondary; dust and smaller leftovers ejected due to the impact may still be present around the asteroids at the time of Hera arrival. Large boulders were detected in images by Hubble and ground observatories [35]: they do not pose a threat thanks to the millions of kilometers of distance they reached after exceeding the escape velocity (around $\approx 0.24 m/s$) due to the energy transfer of the impact. However, there is not guarantee that none remained within the Didymos sphere of influence if released through distinct mechanisms.

### 3.2.2. Environment models description

The reference trajectory ("truth") that utilized for this study is computed through propagation from given initial conditions, accounting for the Hera spacecraft state, attitude and environment. The Hera GNC simulator includes all the relevant perturbations acting on the spacecraft CoM. The details of the parameters and the modeling equations are omitted, but a qualitative description is offered.

1. **Didymos**: spherical (central force) and non-spherical gravity as Exterior spherical Harmonics expansion model up to degree 2 [72]. The body is treated as point mass irrespective of the distance.
2. **Dimorphos**: $3^{rd}$ body perturbation to account for its central force along with the non-spherical gravity. The latter is included as if the body were the main attractor by subtracting its gravitational pull on Didymos. Similarly to Didymos, the secondary is considered as point mass regardless of its distance from the spacecraft.
3. **SRP**: detailed model considering a representation of the SC with multiple panels. The properties of each are derived by averaging the values of the components they represent. The attitude determines the dynamics in "closed-loop" and its effect is indeed notable due to the magnitude of the perturbation. The model accounts for eclipses of Didymos and Dimorphos.
4. **Sun**, **Earth** and **Mars**: treated as $3^{rd}$ body perturbation due to point masses.
5. **Non-modeled accelerations**: random accelerations modeled as discrete Exponentially correlated random variable (ECRV) [70].
6. **Control acceleration**: computed as ratio between the actually executed thrust vector and the mass of the spacecraft at each time instant.
7. **Internal perturbations**: propellant sloshing and flexible modes are included. Their effect is the cause of the high frequency oscillations noticeable in the results presented in the next chapters in correspondence of the manoeuvres. The sudden changes noticeable in fig. 3.7 are in fact related to these accelerations. It is stressed that by definition, internal perturbations cannot affect the CoM orbital motion with respect to Didymos.

The ephemerides required for the computations are generated at each simulation start-up from SPICE kernels[1]. As final note, a scattering of the parameters involved in the models

[1] `https://www.cosmos.esa.int/web/spice/spice-for-hera`. Last visited: 02 Nov. 2023

is always performed, such that the "truth" parameters slightly differ from their nominal values, but within the assumed uncertainty.

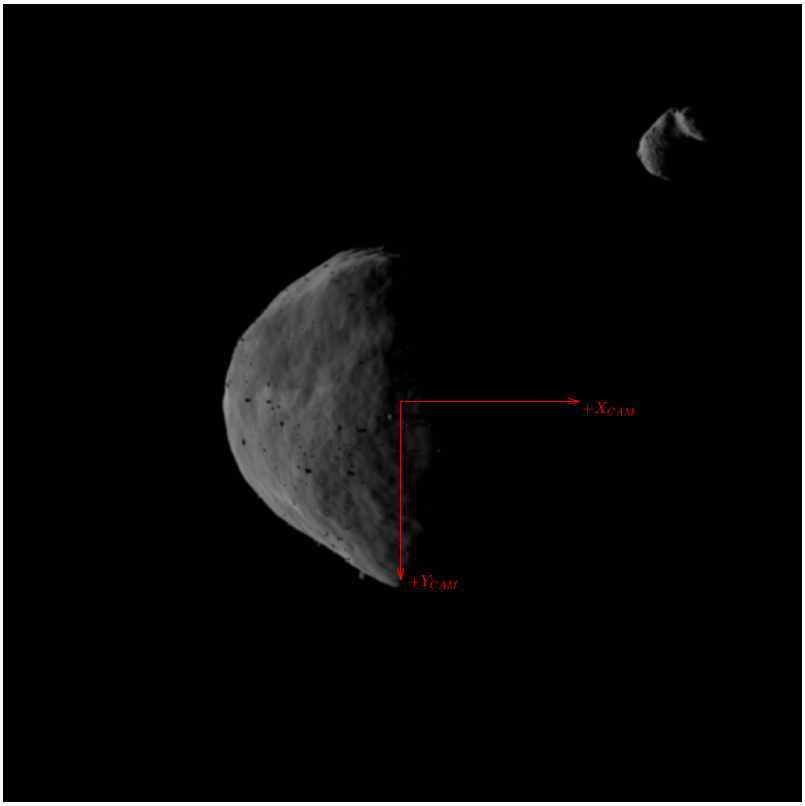


Figure 3.5: Didymos and Dimorphos as scaled (25143) Itokawa. Simulated image as acquired by NavCam, generated with PANGU v5.0[2].

### 3.2.3. Perturbations and propagation analysis

The reference trajectory generated from the aforementioned models was used for a brief analysis of the dynamics in flying the EXP trajectory of fig. 3.4. The magnitude of the accelerations over time are shown in fig. 3.6 compared with the magnitude of the position vector. [25] conducted an analysis of the same environment for the Hera's Milani Cubesat, revealing good agreement in the orders of magnitude of the accelerations. It is essential to note, however, that the gravitational acceleration contributions presented by the authors are referenced to each body individually. The slight differences observed in the magnitude of SRP acceleration stem from the variations in mass and surface area between Milani

[2] `https://pangu.software/`, Last visited: 02 Nov. 2023

and Hera.

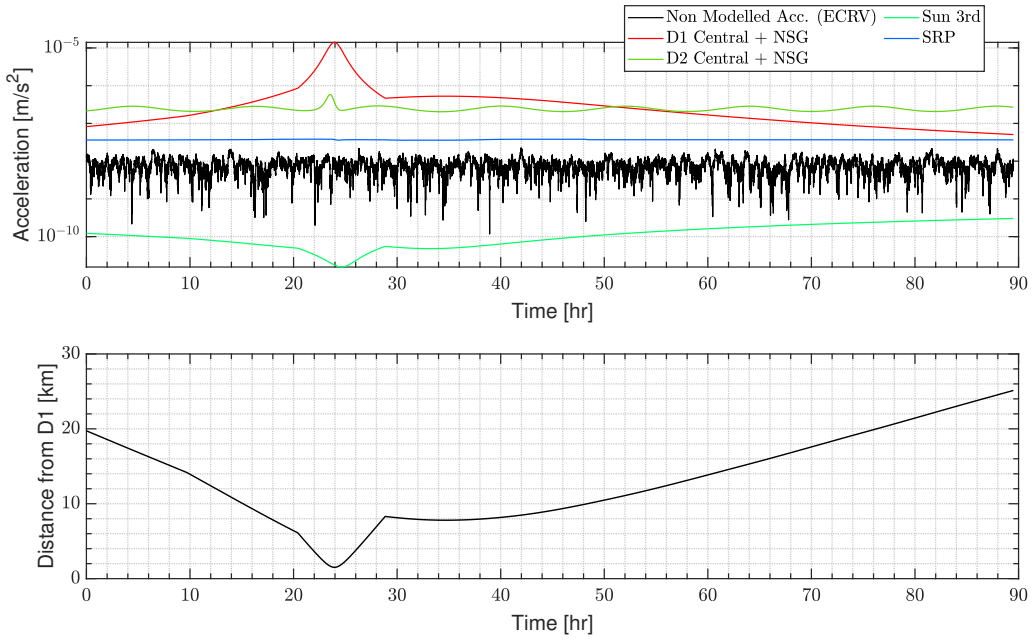


Figure 3.6: Magnitude of perturbation acceleration with the corresponding distance $||\mathbf{r}||$ from CoM during EXP arc 1 trajectory @Didymos CI.

Both Dimorphos and the SRP exert a significant influence in determining the spacecraft trajectory. The green line corresponding to the former clearly reveals the periodicity of the Dimorphos revolution. Figure 3.7 shows the osculating keplerian elements, providing insights into how the orbit is modified by the perturbations. The time history of these elements, assuming two-body motion, is also depicted. This discrepancy was also utilized as a reference for the magnitude of the process noise entries in chapter 4 and served as support for the considerations in chapter 5.
Both the mentioned periodicity and the secular drift induced by the SRP, pushing the spacecraft toward the asteroids, are discernible by inspection of the plots. Finally, a comparison of the trajectories propagated with three simplified dynamics model was conducted to assess how increasing levels of assumptions contribute to errors in predicting the state vector. The manoeuvres are applied at a single time instant as impulsive changes to the $\Delta\mathbf{v}$.

1. Keplerian dynamics assuming the mass of both the primary and the secondary as concentrated in the CoM (i.e. summing the gravitational parameters, 3.1)

$$\begin{bmatrix} \dot{\mathbf{r}} \\ \dot{\mathbf{v}} \end{bmatrix} = \begin{bmatrix} \dot{\mathbf{v}} \\ -\dfrac{\mu_{D1} + \mu_{D2}}{r^3}\,\mathbf{r} \end{bmatrix} \tag{3.1}$$

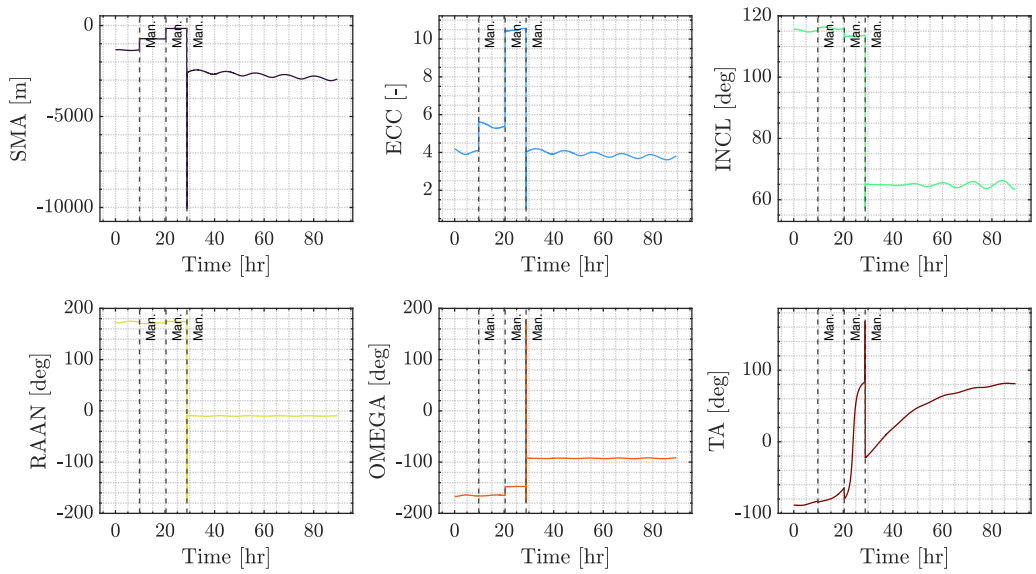


Figure 3.7: Osculating Keplerian elements of the EXP arc 1 trajectory @Didymos CI.

2. Including the $3^{rd}$ body perturbation of the secondary.
3. Including the $3^{rd}$ body perturbation of Dimorphos, the Sun and the SRP.

Eq. 3.2 specifies the third-body gravity perturbation model as derived from the general N-body problem with shifted propagation center [62].

$$\mathbf{a}_{3rd} = \mu_{3rd} \left( \frac{\mathbf{r} - \mathbf{r}_{3rd}}{||\mathbf{r} - \mathbf{r}_{3rd}||^3} - \frac{\mathbf{r}_{3rd}}{||\mathbf{r}_{3rd}||^3} \right) \tag{3.2}$$

The simplified Cannonball model is employed for the SRP contribution (3.3) [62].

$$\mathbf{a}_{SRP} = -P_{SRP}\, C_{SC}\, \frac{A_{SC}}{m_{SC}} \left( \frac{\mathbf{r} - \mathbf{r}_{Sun}}{||\mathbf{r} - \mathbf{r}_{Sun}||} \right) \tag{3.3}$$

where $P_{SRP}$ is the Solar radiation pressure at the distance of the system from the Sun (eq. (3.4) approximates its value at a given distance in AU); $C_{SC}$ is the average coefficient of reflection of the spacecraft, derived from spacecraft properties 3.5; $A_{SC}$ is set equal to the maximum cross section area that can be exposed to the Sun. Since the SRP pushes the spacecraft toward the asteroids system and the evaluation of the closest approach distance is of interest, the latter is deemed to be a conservative assumption.

$$P_{SRP}(AU) = \frac{1}{AU^2} P_{SRP}(1\,AU) = \frac{1367}{AU^2}\ [W/m^2] \tag{3.4}$$

$$C_{SC} = 1 + \bar{\rho}_{reflection} + \frac{2}{3}\bar{\rho}_{diffusion} \tag{3.5}$$

The values assumed for the estimation during the EXP phase are: $P_{SRP} = 1.325 \times 10^{-6}\ W/m^2$ since the EXP takes place when Hera is at approximately 1.8 AU from the Sun; $A_{SC} = 19.57\,m^2$; $C_{SC} = 1.264$ using $\bar{\rho}_{reflection} = 0.2265$ and $\bar{\rho}_{diffusion} = 0.0561$. The mass of the spacecraft changes only of a little amount during the manoeuvres, as a consequence of the very low required $\Delta\mathbf{v}$. Therefore, it is considered constant equal to $m_{SC} = 1102.022\ kg$. Fig. 3.8 shows the trajectories in CI frame, with the time histories of the components of the position error in fig. 3.9. The absolute and relative values

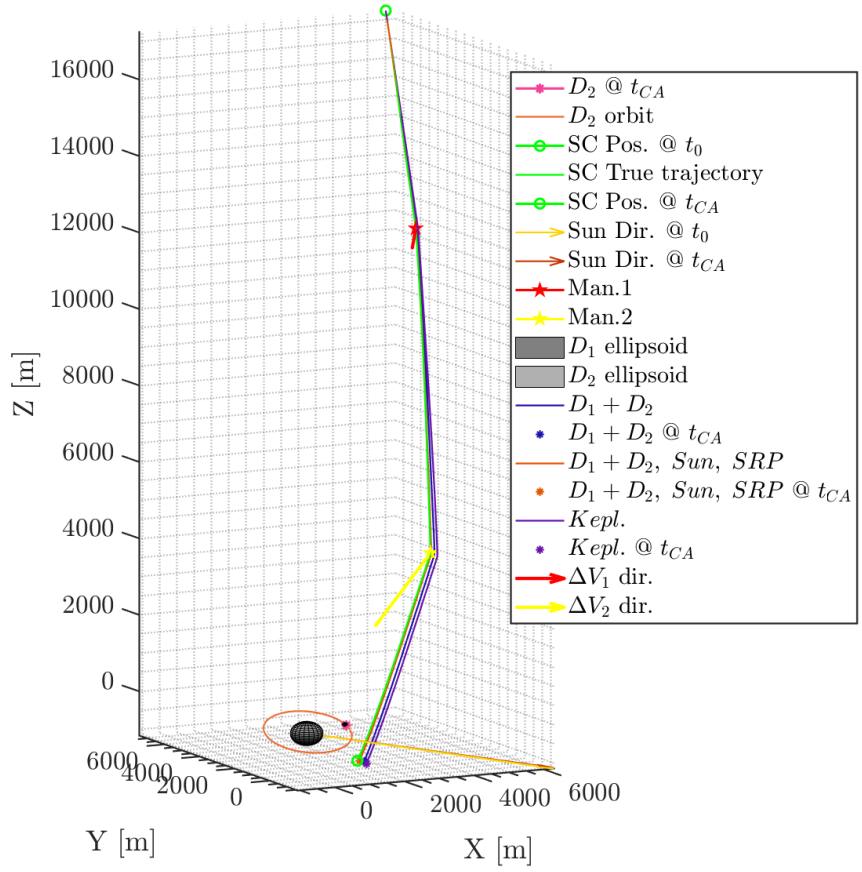


Figure 3.8: EXP arc 1 trajectory propagated up to closest approach with the presented dynamics models @Didymos CI.

of the error norm are reported at the end of each manoeuvre and at the "true" time of closest approach in table 3.2, table 3.3. These are defined as in 3.6 where $\mathbf{x}$ is either the position or the velocity vector in $[m]$ and $[mm/s]$, respectively. Not surprisingly, the SRP determines the greatest reduction in the error due to the fact that its contribution

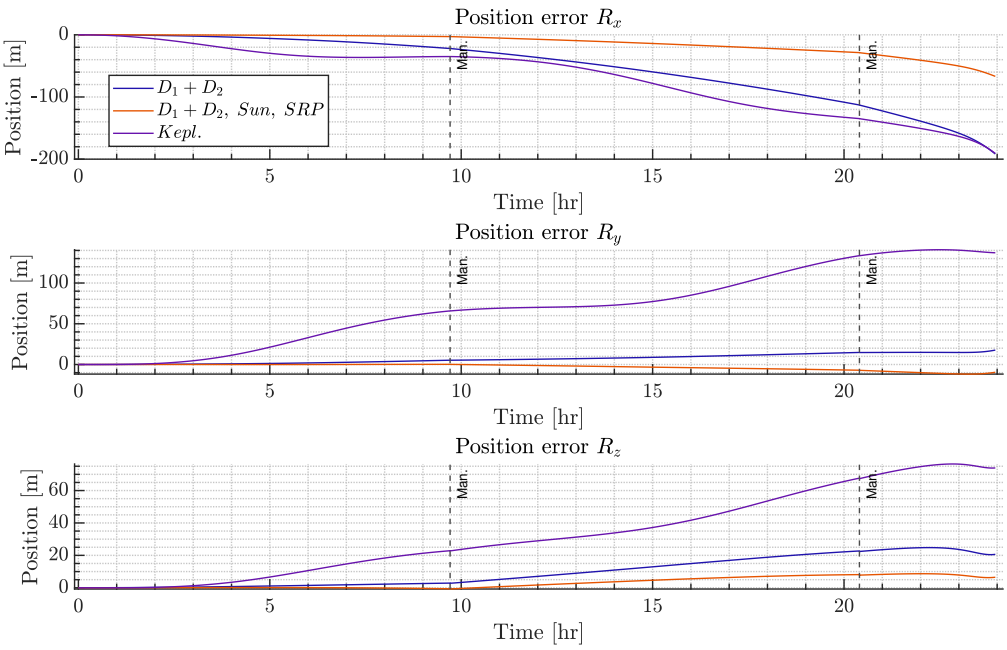


Figure 3.9: Position errors of simplified models with respect to reference trajectory during EXP arc 1 up to CA @Didymos CI.

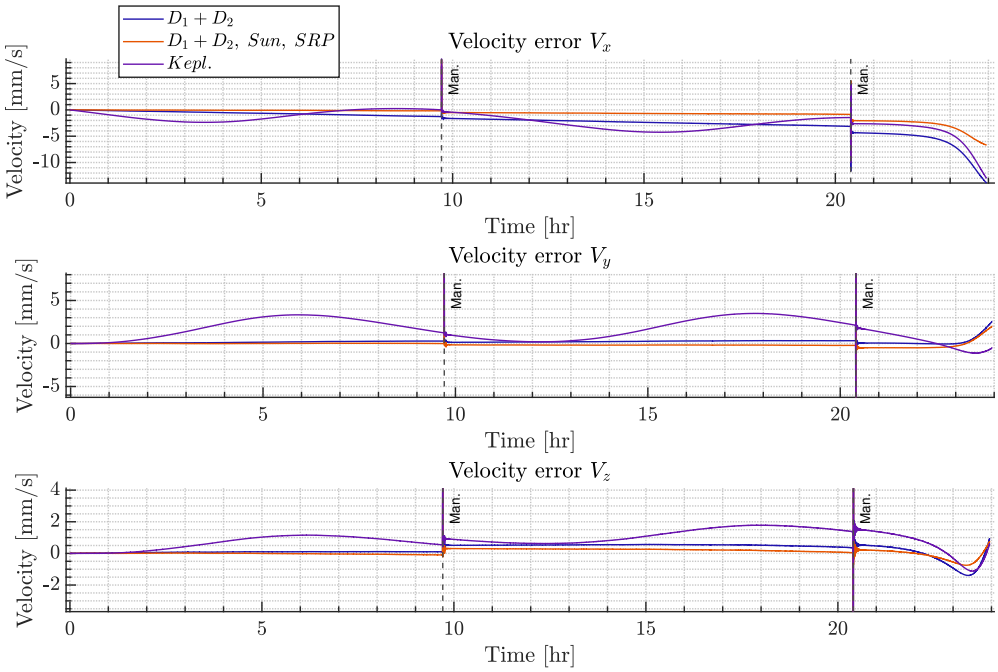


Figure 3.10: Velocity errors of simplified models with respect to reference trajectory during EXP arc 1 up to CA @Didymos CI.

accumulates along the entire trajectory. However, it's noteworthy that due to the shape and orientation of the trajectory, the SRP cannot induce the spacecraft to transition to a closed orbit. Furthermore, the effect of Dimorphos' period of revolution is evident when comparing the Keplerian dynamics propagation with the model including its third body perturbation, mirroring the acceleration oscillation in fig. 3.6.

$$\varepsilon_{abs} = ||\mathbf{x}_{prop.} - \mathbf{x}_{ref}|| \ ; \qquad \varepsilon_{rel} = 100\,\frac{\varepsilon_{abs}}{||\mathbf{x}_{ref}||} \tag{3.6}$$

Table 3.2: Position absolute and relative error norms at manoeuvre point and closest approach wrt reference. Each row corresponds to a model.

| Time Instant | $1^{st}man.$ | $2^{nd}man.$ | Closest approach |
|---|---|---|---|
| Abs. pos. error | $\begin{bmatrix}77.9203\\22.86\\2.9553\end{bmatrix}$ [m] | $\begin{bmatrix}202.1232\\116.2046\\30.6103\end{bmatrix}$ [m] | $\begin{bmatrix}246.2732\\193.1667\\67.3093\end{bmatrix}$ [m] |
| Rel. pos. error | $\begin{bmatrix}0.55\\0.16\\0.02\end{bmatrix}$ % | $\begin{bmatrix}3.30\\1.90\\0.50\end{bmatrix}$ % | $\begin{bmatrix}16.31\\12.79\\4.46\end{bmatrix}$ % |

Table 3.3: Velocity absolute and relative error norm at manoeuvre point and closest approach wrt reference.

| Time instant | $1^{st}man.$ | $2^{nd}man.$ | Closest approach |
|---|---|---|---|
| Abs. vel. error | $\begin{bmatrix}1.344\\1.3080595\\0.2010428\end{bmatrix}$ [mm/s] | $\begin{bmatrix}11.855\\13.91\\12.3475035\end{bmatrix}$ [mm/s] | $\begin{bmatrix}13.018\\14.15\\6.9877062\end{bmatrix}$ [mm/s] |
| Rel. vel. error | $\begin{bmatrix}0.74\\0.77\\0.19\end{bmatrix}$ % | $\begin{bmatrix}4.87\\5.71\\5.08\end{bmatrix}$ % | $\begin{bmatrix}2.63\\2.85\\1.41\end{bmatrix}$ % |

The entire EXP trajectory is affected by Dimorphos $3rd$ body perturbation and SRP in a definitely non-negligible way as anticipated by the perturbations contributions.
In the context of navigation, it is crucial to recognize that the chosen motion model has a substantial impact on the achievable accuracy of sequential filters. Large disparities between the "true" dynamics and the model may hinder the convergence of the filter, preventing it from accurately tracking the trajectory. This is primarily due to two reasons:

- The forward prediction of the state (i.e. propagation of the model) is prone to significant errors, especially during measurement outages.

- The measurement predictions consistently result distant from the actual measurements, making the filter incapable of incorporating the measurements (intuitively: the model cannot "explain" the observations).

This implies that for applications focused on navigating the environment, assumptions like Keplerian dynamics are too simplistic. Nevertheless, it may be noted that the position errors in 3.2 might still be acceptable for trajectory safety FD purposes, particularly before reaching very close distances relative to Dimorphos, as long as an adequate number of measurements is available to avoid pure propagation. Additionally, the relative velocity errors (3.3), which are equally relevant for determining the closest approach distance, do not exhibit a substantial discrepancy as the position ones.

## 3.3. Hera Navigation architecture

### 3.3.1. Sensors suite

**NavCam** The Hera spacecraft is equipped with two Asteroid Framing Camera (AFC) which serve as either payload or navigation camera, depending on the specific operation. This instrument is a direct derivation from the AstroHead sensor built by Jena Optronik[3] [24]. The relevant intrinsic camera parameters for the definition of the calibration matrix $K_{CAM}$ (3.7) are reported in table 3.4.

Table 3.4: Asteroid Framing Camera parameters.

| Parameter | Value |
|---|---|
| Focal length f | 105.60 mm |
| Detector size | 1020 pix |
| Field of Fiew | 5.5 deg |
| Non-dim. $\bar{f}$ | 10560 [-] |
| Centre coords. $[c_x, c_y]$ | $[510, 510]$ pix |

$$K_{CAM} = \begin{bmatrix} \bar{f} & 0 & c_x \\ 0 & \bar{f} & c_y \\ 0 & 0 & 1 \end{bmatrix} \tag{3.7}$$

Both AFC are mounted on the asteroid deck and have their bore-sight aligned with the +Z axis of the SCB. Only one camera is enabled at any time for navigation purposes, the

[3] https://www.jena-optronik.de/products/star-sensors/applications/astrohead.html. Last visited: 10/31/2023

other primarily serving as redundant unit.

**Altimeter** Similarly to the camera, the altimeter measurements are used for both scientific and navigation purposes. The Planetary Altimeter (PALT) is a time-of-flight laser altimeter capable of measuring the range to the surface of the target body up to 14 $km$, with a meter level accuracy [23]. The nominal mounting configuration positions the altimeter bore-sight aligned with the +Z axis of the SCB frame.

### 3.3.2. Observables, filtering and navigation strategy for EXP

**Architecture and algorithms overview** In contrast to the nominal mission phases, the navigation during the experimental phase fully takes advantage of the on-board functionalities. In fact, it relies upon ground orbit determination only for the state and covariance initialization necessary for the estimation filter start-up. The scheme in fig. 3.11 provides a high-level overview of the GNC components of interest for this study. The Cen-

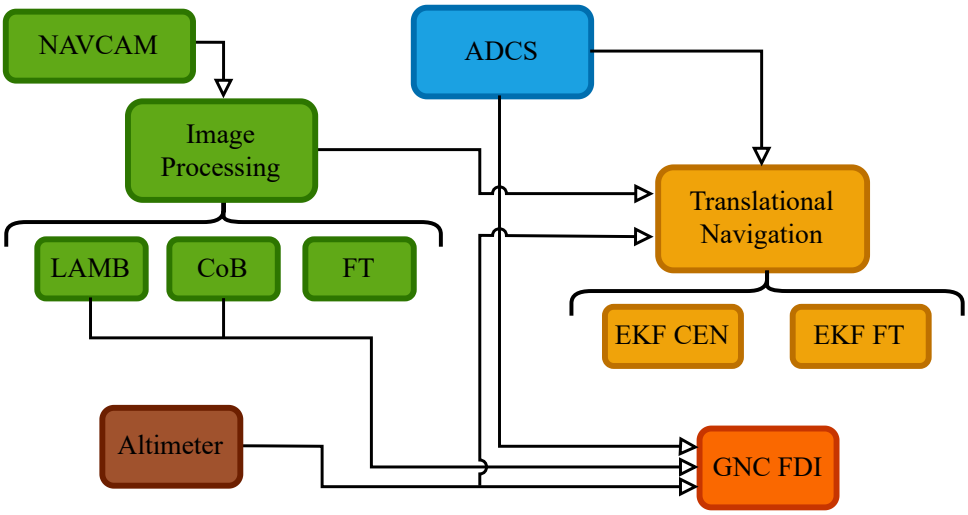


Figure 3.11: Hera on-board Navigation architecture high-level overview.

troiding IP algorithms extract the centroid coordinates in the image plane by processing each acquired image from the AFC. These are equivalent to a line-of-sight direction (unit vector in CAM frame). A time interval of 48 $s$ is assumed in between images. The concepts of the algorithms are briefly explained; for more details refer to [8, 58].

1. **Maximum correlation with Lambertian Sphere** (LAMB): the algorithm uses the visible portion of the body to correlate it with a Lambertian sphere, generated considering the same Sun phase angle of the body. The centre and the radius of the sphere are fitting parameters to optimize with respect to a correlation index. This

algorithm ensures good performance with Sun phase angles up to 120, provided that a sufficiently large limb of the body is imaged.

2. **Centre of Brightness** (COB): it extracts the centroid from "blobs" of bright pixels obtained after thresholding, by weighting their position in the image plane. Contrarily to LAMB, the Sun phase angle significantly impacts the performance, causing the CoB to shift in a direction approximately parallel to the Sun rays. This effect must be accounted for in the observation models.

The observables are fused by an EKF with dynamical model compensation (DMC) for parameters of both dynamical and observation models [68, 70].

**Navigation during EXP** The availability of observables during the navigation window mainly depends upon the distance from Didymos [58]. The camera FoV is in fact "saturated" by Didymos around 9 $km$ and by Dimorphos around 2 $km$. Eq. 3.8 provides the approximate angular size of a target body for a given average diameter and distance. Didymos, considering the average diameter in table 3.1 is used as example.

$$D_{angle} = sin^{-1}\left(\frac{D_{meters}}{Distance}\right) = sin^{-1}\left(\frac{772\ m}{8000\ m}\right) = 5.54\ deg \tag{3.8}$$

Figure 3.12 shows which observables are acquired during nominal navigation in relation to the time elapsed from initial conditions. From the considerations in 3.1.3, the time window of interest for the present work is between the initial time and about 1 hour after the second manoeuvre occurs, identified by the black dashed line. Notice that Dimorphos is eclipsed by Didymos from around $T = +18\ hr$.

### 3.3.3. Sensors models and considered errors

The simulation data used for the analysis of the algorithms, presented in chapter 5 were generated from two sources:

1. The Hera GNC simulator: the Simulink model constituting the Functional Engineering Simulator of the mission. The simulation encompasses the entire GNC hardware and software, as well as the image processing algorithms to be deployed, and the interface with the OBSW. In fact, all simulations are executed in closed-loop with PANGU [48], a rendering software for the generation of high-resolution and fidelity images with the specific scope of testing vision-based GNC architectures. A scheme illustrating the prototype version is reproduced in fig. 3.13 from [58]. It will be referred to as Higher fidelity model (HFM) in the remaining of the work.

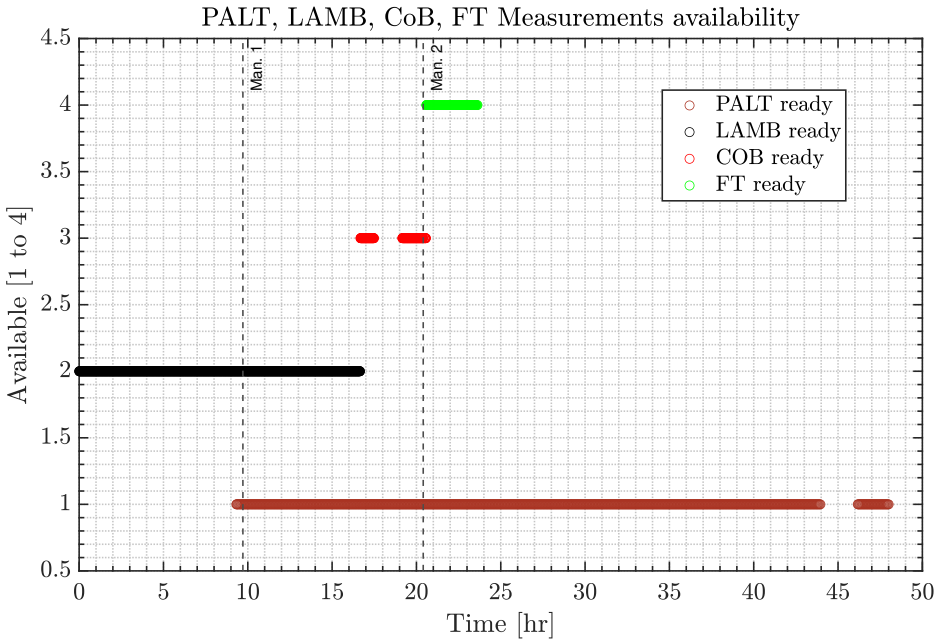


Figure 3.12: Observables availability windows during Nominal EXP arc 1 trajectory.

2. Simplified measurements models, identical to the observation models presented in chapter 4. These are employed either to generate artificial set of measurements from the "truth" provided by the simulator or to evaluate the algorithms on different trajectories not available from the former. This will be referred to as Lower fidelity model (LFM).

## Higher fidelity models

The detailed modeling and list of all the effects considered in the simulator are omitted and a qualitative description is instead provided. The sources of errors which relevantly affect the performance of the proposed methods are the following:

1. IP algorithms running on PANGU images generated based on the NavCam model (including distorsions, thermo-elastic effects, electronics effects). It faithfully reproduces effects related to the Sun Phase angle, morphology, and shape of the bodies, as well as occurrences such as partial or total reciprocal occultations, images, and camera defects.

2. Altimeter measurements generated from accurate shape model and beam modeling, including white noise, constant offset, time-correlated bias process to model the surface roughness (i.e., boulders frequency and size).

3. Attitude quaternion as estimated by attitude determination in closed loop. The de-

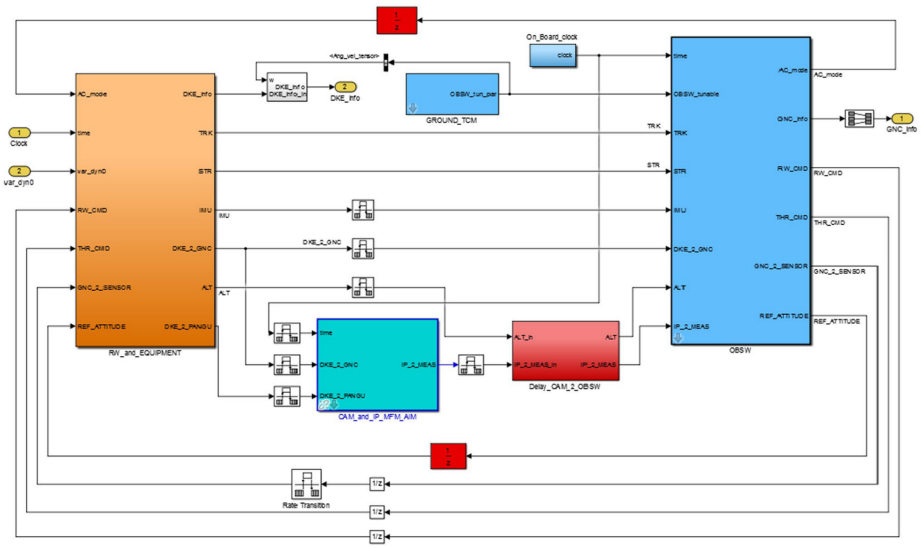


Figure 3.13: Hera GNC FES prototype. Reproduced from [59].

termination is performed by Gyrostellar filter (e.g., [29]) using gyros for propagation and attitude measurements from Star trackers.

4. On-board knowledge errors of Ephemerides of all bodies on both orbit and attitude information (if applicable).

5. The actuators suite is modeled with an equally high level of detail and indirectly affect the simulation through the attitude estimate, measurements, and the executed Delta V (the pulse counted Delta V is used for the manoeuvres instead of the actually performed in the DKE, meaning that actuation errors are included in the evaluation).

6. Configuration misalignments in SCB of all the sensors and actuators. The offset concerning the altimeter and the camera are reported here:

$$\hat{\mathbf{l}}_{Alt} = \begin{bmatrix} -0.00011 \\ 0.00023 \\ 0.99974 \end{bmatrix}; \quad \hat{\mathbf{q}}_{CAMwrtSCB} = \begin{bmatrix} -0.000059 \\ 0.000001 \\ -0.999999 \\ 9.0556 \times 10^{-11} \end{bmatrix}$$

## Lower fidelity models

The LFM replaces the IP, the altimeter and the attitude determination and control loop with simplified models. All the other effects are not considered. The "True" ephemerides for all the bodies are always used. The choice between the HFM and LFM is specified

on a case-by-case basis in the results section. The same observation models detailed in chapter 4 are applied for the centroid simulation, while the altimeter measurements assume a spherical body shape of radius equal to its average value. The attitude estimate is optionally replaced by a simulated one. A white noise error and a correlated bias (as First-Order Gauss-Markov process [10] are added as artificial noise, if desired.

**Attitude estimate** The attitude estimate is constructed "backward" from the camera attitude. Ideal nominal pointing is assumed where the bore-sight $Z_{CAM}$ of the camera is determined by the relative position to the target body. The angular momentum vector is used for the $X_{CAM}$ axis since it is sufficient for $X_{CAM}$ and $Y_{CAM}$ to be orthogonal to the bore-sight.

$$\mathbf{Z}_{CAM} = -\frac{\mathbf{r}_{SCwrtTB}}{||\mathbf{r}_{SCwrtTB}||}; \quad \mathbf{X}_{CAM} = \frac{\mathbf{r}_{SC} \times \mathbf{v}_{SC}}{||\mathbf{r}_{SC} \times \mathbf{v}_{SC}||}; \quad \mathbf{Y}_{CAM} = \mathbf{Z}_{CAM} \times \mathbf{X}_{CAM}$$

The corresponding DCM of the CAM frame attitude wrt CI is assembled and converted to quaternion:

$$\mathrm{DCM}_{CAMwrtCI} = \begin{bmatrix} \mathbf{X}_{CAM} & \mathbf{Y}_{CAM} & \mathbf{Z}_{CAM} \end{bmatrix}$$

$$\mathbf{q}_{CAMwrtCI} = \texttt{DCM2Quat}(\mathrm{DCM}_{CAMwrtCI})$$

`DCM2Quat` is a function implementing the conversion from DCM to quaternions [47]. The "true" configuration quaternion of the CAM wrt SCB is finally used to generate the quaternion of the SCB wrt CI:

$$\mathbf{q}_{SCBwrtCI} = \mathbf{q}_{CAMwrtCI} \otimes \mathbf{q}_{CAMwrtSCB}$$

The "estimated" attitude of the camera is instead simulated by rotating the "true" attitude through a displacement quaternion $\delta q$ (quat. product), and converted to the SCB attitude using the offset configuration quaternion:

$$\delta\mathbf{q}_i \sim N(0, \sigma^2_{ADCS}) \quad i = 1,2,3 \quad \Rightarrow \quad \delta\mathbf{q} = \begin{bmatrix} \delta q_1 \\ \delta q_2 \\ \delta q_3 \\ \sqrt{1 - ||\delta\mathbf{q}_{1:3}||^2} \end{bmatrix}$$

$$\hat{\mathbf{q}}_{CAMwrtCI} = \mathbf{q}_{CAMwrtCI} \otimes \delta\mathbf{q}$$

where $\sigma^2_{ADCS} = (0.0044)^2\ rad^2$ is set to resemble the Hera GNC median pointing error during EXP.

**Altimeter** The altimeter measurement from high fidelity shape model is replaced by tri-axial ellipsoids and a Los intersection model, considering the true attitude from either HFM or LFM. White noise $n(t)$ and FOGM $b(t)$ are added to simulate the presence of noise and effects such as the irregular morphology of the surface [30]:

$$n_{Alt}(t) \sim N(0, \sigma_{Alt}^2)$$

$$\dot{b}_{Alt}(t) = -\frac{1}{\tau_{Alt}} b_{Alt}(t) + n_b(t) \qquad b_{Alt}(t_0) = 0 \tag{3.9}$$

where $n_b \sim N(0, \sigma_{b,Alt}^2)$, $\sigma_{Alt} = 35\,m$; $\sigma_{b,Alt} = 0.5\,m/s$; $\tau_{Alt} = 450\,s$.

**Centroid** The centroiding measurement is generated from a pinhole projection model [34], considering the true attitude from either HFM or LFM. When Dimorphos is the target body, a shift along the Sun direction is added based on the model shown in chapter 4. White noise and FOGM are added to each component independently, using eq. (3.9) with parameters $\sigma_{Cen} = 5\,\text{pix}$; $\sigma_{b,Cen} = 0.1\,\text{pix}/s$; $\tau_{Cen} = 900\,s$.

# 4 | On-board Collision assessment methodologies

## 4.1. Summary of the methods

There are two primary driving requirements:

- Assess the safety of the trajectory based on the available observables (input) according to the specific methodology, yielding a flag suggesting the execution of a CAM as ultimate output in the event of a potential collision risk.
- Maintain a minimal computational cost, ideally significantly lower than the computational load associated with GNC functions.

To meet there requirements, three methodologies were implemented. Each methodology varies in performance, in the information it utilizes, and in its computational cost. This section provides the rationale behind each approach and the details regarding the implementation.

1. **Method 1** (section 4.2): named Measurements-Only Collision risk estimator; it operates without relying on a model of the spacecraft motion. Therefore, it only requires the sensors to acquire range and line-of-sight information to the primary attractor (Didymos) over a specified timeframe.
2. **Method 2** (section 4.3): it employs a Square-Root Unscented Schmidt KF with simplified dynamics. It re-processes the same measurements as the nominal Navigation filter (EKF-based), using observation models adapted for Sigma Points and considered parameters. The variants are analyzed: 1) filtering in Keplerian elements with analytical propagation (kepSRUSKF), 2) filtering in Cartesian coordinates with ODE integration (HF SRUSKF).
3. **Method 3** (section 4.5): referred to as Sequential Hypothesis Test filters bank; it involves two constrained SRUSKF within the framework of binary hypothesis

inferential tests. The PDF of the innovation is exploited to sequentially update the Likelihood ratio, which in turn drives the detection and decision process through the Wald Sequential Probability Ratio Test (SPRT).

## 4.2. Measurements-Only CRE algorithm

The on-line execution of the algorithm can be managed according to the software requirements and is not tied to specific time instants. In this context, the algorithm is run each time a new centroiding measurement is processed. Its initialization occurs only after a buffering process (4.2.3) is complete.

### 4.2.1. Trajectory safety definition and manoeuvre decision

**PoC computation trade-off** The review presented in chapter 2 has identified three potential approaches for computing a probability of collision metric under the Gaussian distribution assumption. Nevertheless, it is noteworthy that all methods designed for "long-term" encounters pose challenges for on-board computation due to their inherent complexity.
In the Hera mission scenario, involving the presence of a secondary body like Dimorphos, these approaches may be applied without particular modification. Additionally, considering the general nature of the formulation, one may also try to apply them for the evaluation of the PoC with respect to the main attractor, by interpreting the Hera orbital state estimate as a *relative* state. However, upon visually inspecting the velocity magnitudes of trajectories around small bodies, particularly in low-gravity environments, it becomes evident that none of the existing techniques are suitable. In fact, the relative velocity between Dimorphos and Hera shown in fig. 4.1 unequivocally reveals that the short-term encounter is *not* valid.
In the context of the Hera mission scenario, the evaluation of miss distance emerges as the only applicable method for defining a trajectory safety metric. This concept can be seamlessly extended to a spacecraft orbiting its primary attractor, where Distance of Closest Approach (DCA) PDF computed through any mean can be interpreted as the miss distance PDF. The same formulation can be readily applied to any object in orbit around the primary.

**DCA prediction method** In the most general case this quantity may be estimated by propagating the current state estimate forward in time until an event function such as the condition of orthogonality of position and velocity vectors, eq. (4.1), is satisfied with

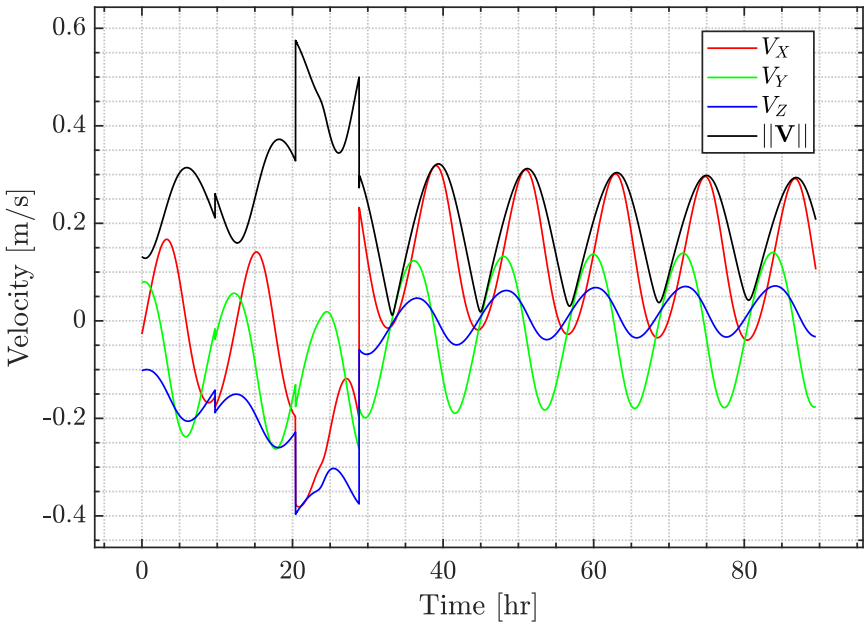


Figure 4.1: Relative velocity components of Hera wrt Dimorphos - EXP trajectory @Didymos CI.

a specified tolerance.

$$\mathbf{r}(t) \cdot \mathbf{v}(t) \leq \epsilon \tag{4.1}$$

Nonetheless, an analytical solution for the computation of the minimum distance given the trajectory appears as the sole viable option to achieve a fast computation, since analytical solutions in Astrodynamics models are limited to cases such as Keplerian dynamics (3.1). The primary issue that prevents the estimation of $\hat{r}_{CA}$ by propagation is the dependency of the integration time from the spacecraft position. The farther the spacecraft is from the actual Time of Closest Approach (TCA) given its current state estimate, the longer the integration time becomes. In the case of the EXP trajectory, this time can extend up to 23 hours, rendering this approach computationally infeasible.
For a qualitative comparison, it's worth noting that the propagation of the mean state through the most comprehensive dynamics described in 3 takes up to 8 seconds, using `ode113` (with a tolerance equal to single machine precision) on an i7 11800H @4.2 GHz. The computational power of the current state-of-the-art space-grade CPUs is considerably more limited [43].

**PoC definition and computation** The formulation of the probability of collision employed in this work is now presented. Let $(\mu_{\hat{r}_{CA}}, \sigma^2_{\hat{r}_{CA}})$ represent the mean and the

variance of the estimated miss distance, so that its Probability Density Function is fully defined under the Gaussian assumption:

$$p(x; \mu_{\hat{r}_{CA}}, \sigma^2_{r_{CA}}) \approx N(\mu_{\hat{r}_{CA}}, \sigma^2_{r_{CA}}) = \frac{1}{\sqrt{2\pi}\sigma_{r\hat{C}A}} \exp\left(-\frac{x - \mu_{\hat{r}_{CA}}}{\sigma^2_{\hat{r}_{CA}}}\right)$$

The Hera mission trajectories require the spacecraft to fly as close as approximately 300 meters from the secondary body during the VCFB, whereas the minimum distance from Didymos equals to 1510 $[m]$. In light of this, the simplest and most conservative approach to conduct a collision assessment relies on the definition of a Keep-out sphere (KoS) of radius $R_{KoS}$ the spacecraft must not cross. This design choice is further substantiated by the constraints posed by the GNC system, the Hera baseline trajectory, and the navigation capabilities outlined in 3: flying below Dimorphos' orbit is not part of the mission objectives and the GNC system has not been validated to deliver sufficient performance under such circumstances.

The $R_{KoS}$ value was determined eq. (4.2) aims at balancing the probability of triggering unnecessary manoeuvres due to false alarms with the risk of overlooking a potential collision. Indeed, this parameter selection inherently include considerations related to both factors.

$$R_{KoS} = r_{D2} + 0.05\, r_{D2} + R_{D2,max} = 1240\, m + 62\, m + 60\, m = 1362\ [m] \tag{4.2}$$

where $r_{D2}$ is the radius of Dimorphos orbit and $R_{D2,max}$ is the largest radius of Dimorphos shape. A 5% uncertainty is assumed on the orbital radius.

Finally, it is important to stress that this parameter must be adjustable during the Operational phase, as further studies of the system, and the Early characterization phase of the mission will likely require its re-tuning.

The evaluation of the probability of the spacecraft to enter the KoS is simply defined in terms of the Cumulative distribution function (CDF) of the miss distance distribution as eq. (4.3).

$$Pr(r_{CA} \leq R_{KoS}) = \int_{-\infty}^{R_{KoS}} \frac{1}{\sqrt{2\pi}\sigma_{r\hat{C}A}} \exp\left(-\frac{x - \mu_{\hat{r}_{CA}}}{\sigma^2_{\hat{r}_{CA}}}\right) dx \tag{4.3}$$

The error function can be used to compute this probability as eq. (4.4) [1].

$$Pr(r_{CA} \leq R_{KoS}) = \frac{1}{2}\left(1 + \texttt{erf}\left(\frac{R_{KoS} - \mu_{\hat{r}_{CA}}}{\sqrt{2}\sigma_{r\hat{C}A}}\right)\right) \tag{4.4}$$

**Threshold-based decision** The CAM decision problem, i.e., whether to issue a flag prompting an avoidance maneuver to the OBSW, is addressed by establishing a probabil-

ity threshold $Pr_{max}$. In other words, the probability value of eq. (4.3) is compared against the tunable value of the maximum acceptable probability resulting in a boolean variable. To enhance the robustness of this evaluation against instantaneous fluctuations in the estimation process, the strategy may involve the introduction of a counter variable. This accumulates the number of consecutive time instants in which the second condition in eq. (4.5) is satisfied. The flag $B_{CAM}$ is raised only when the counter surpasses a specified value, a parameter in turn tunable based on considerations such as the spacecraft's maneuvering capabilities and its proximity to the system at the time of detection.

$$B_{CAM} = \begin{cases} 0 & \text{if } Pr(r_{CA} \leq R_{KoS}) \leq Pr_{max} \\ 1 & \text{if } Pr(r_{CA} \leq R_{KoS}) > Pr_{max} \end{cases} \tag{4.5}$$

Additionally, for added robustness the flag may be raised also in cases the spacecraft is no longer able to acquire observations whenever the second of eq. (4.5) is satisfied even if the counter has not reached its threshold value. The rationale is grounded in the fact that the measurements acquisition process of Hera is intimately linked to its capability of pointing to the asteroids. Consequently, a loss of the measurements information hampers the on-board navigation and may be indicative of a thruster failure.

### 4.2.2. Estimation of miss distance mean and variance

The method described above expects the estimated miss distance and its variance as inputs. In the framework of the Keplerian dynamics, the pericentre distance is analytically linked to the orbit energy and angular momentum, both of which are integrals of motion. Two functions were derived to compute this quantity by leveraging (eq. (4.6), eq. (4.7)). The first function maps the position and velocity vectors ($\mathbf{r}$, $\mathbf{v}$) to the pericentre distance of the trajectory, while the second accomplishes the same task using in-plane trajectory properties, namely the distance $r$, the radial velocity $\dot{r}$ and the orbital angular velocity $\dot{\theta}$.

$$\varepsilon = \frac{v^2}{2} - \frac{\mu}{r} = \text{const.} \quad \text{where } v^2 = \dot{r}^2 + (r\dot{\theta})^2 \tag{4.6}$$

$$h = ||\mathbf{r} \times \mathbf{v}|| = r^2\dot{\theta} = \text{const.} \tag{4.7}$$

**Analytical derivation from trajectory properties** Beginning with eq. (4.6) and eq. (4.7), the orbital energy can be expressed in terms of velocity and position magnitudes at the pericentre of the orbit, noting that the radial velocity component nulls out. Furthermore, by substituting the expression of the velocity derived from Orbit Kinemat-

ics:

$$\varepsilon = \frac{1}{2}\left(\dot{r}^2 + r^2\dot{\theta}^2\right) - \frac{\mu}{r} = \frac{h^2}{2r_p^2} - \frac{\mu}{r_p} = \frac{r^4\dot{\theta}^2}{2r_p^2} - \frac{\mu}{r_p}$$

By solving for $r_p$ after some manipulation, the second order algebraic equation in $r_p$ is found and straightforwardly solved to yield eq. (4.8).

$$\left(\dot{r}^2 + r^2\dot{\theta}^2 - \frac{2\mu}{r}\right) r_p^2 + 2\mu\, r_p - r^4\dot{\theta}^2 = 0$$

$$r_{CA}(r,\dot{r},\dot{\theta}) = r_p(r,\dot{r},\dot{\theta}) = \frac{-\mu + \sqrt{\mu^2 + \left(r^4\dot{\theta}^2\right)\left(\dot{r}^2 + r^2\dot{\theta}^2 - 2\mu/r\right)}}{\left(\dot{r}^2 + r^2\dot{\theta}^2 - 2\mu/r\right)} \tag{4.8}$$

**Analytical derivation from State Vector** The same steps can be replicated by substituting the orbital angular momentum as function of the state vector, and recalling that the norm of the cross product can be alternatively expressed as eq. (4.9).

$$||\mathbf{r} \times \mathbf{v}|| = r^2 v^2 - (-\mathbf{r} \cdot \mathbf{v}) \tag{4.9}$$

Indeed, eq. (4.10) exhibit the same structure as eq. (4.8), with the key distinction being that it can not be utilized solely based on measurements, since not all the components of the state vector can be directly observed. Nevertheless, this characteristic makes the latter form more suitable when a trajectory estimation filter is employed.

$$r_p(\mathbf{r},\mathbf{v}) = \frac{-\mu + \sqrt{\mu^2 + \left(r^2v^2 - (-\mathbf{r}\cdot\mathbf{v})\right)\left(v^2 - 2\mu/r\right)}}{\left(v^2 - 2\mu/r\right)} \tag{4.10}$$

The equivalence between the formulas is proved in figure 4.2a, computing the orbit properties using classical Orbital Mechanics [72] from the reference trajectory. Figure 4.2b shows that the error is only due to finite arithmetic.

**Miss distance variance** Given that eq. (4.10) and eq. (4.8) are two non-linear functions in the general form:

$$\mathbf{y} = \mathbf{f}(\mathbf{x}, \mu)$$

any method for uncertainty propagation can be applied. The Unscented Transform was employed to minimize the linearization error, considering that the computational cost difference compared to the Linear Covariance method is negligible.

$$(\mu_{\hat{r}_{CA}}, \sigma^2_{\hat{r}_{CA}}) = \mathtt{UT}(r_p(\mathbf{x});\, \mathbf{x}, P_x)$$

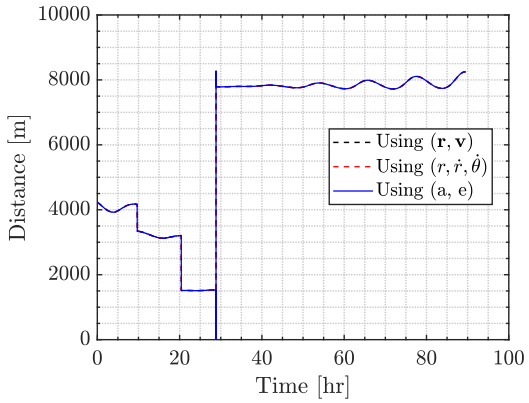


(a) Pericentre distance as 2BP, true trajectory.

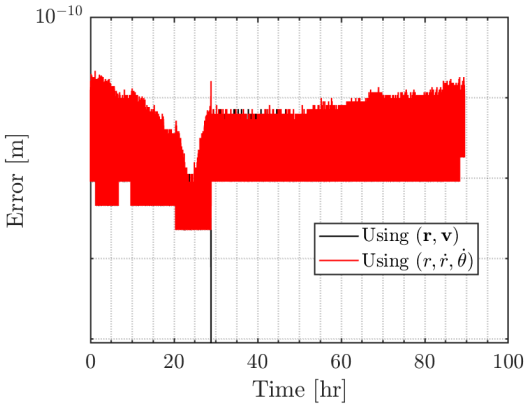


(b) Error with respect to keplerian elements.

where $(\mathbf{x}, P_x)$ are either the state vector or the trajectory properties, and $\mathbf{P_x}$ the respective covariance.

### 4.2.3. Estimation of in-plane properties

**Measurement buffering** The evaluation of eq. (4.8) requires estimation of the three inputs at the specific time instant of interest. However, direct propagation of the quantities is not viable as no motion model is employed. To address this, the altimeter and the centroid measurements are stored in a buffer as soon as they become available along with the timetags corresponding to the acquisition time. Other quantities, including the attitude quaternion involved in the computations, are similarly buffered. Additionally, the oldest measurement in the buffer is overwritten by the most recently acquired one.
The size of the buffers is determined by the number $N_{cen}$ of centroid measurements chosen for the estimation. The number $N_{alt}$ of altimetry measurements is selected to be equal to $\Delta t_{IP} N_{cen}$ to ensure that a certain overlap of timetags between IP front-end and altimeter preventing the need for extrapolation. Moreover, the estimation process only begins after all the buffer arrays have been completely filled.
To improve the robustness of the algorithm, each entry in the buffer is associated with a validity flag based on physical consistency (see . The number of valid measurements is then compared against a tunable threshold to determine whether it is sufficient to initiate the estimation process. In any case, invalid measurements are discarded.

$$N_{valid} \geq 0.95\, N_{size} \Rightarrow \texttt{ExecuteFlag} = 1$$

**Estimation of $r$ and $\dot{r}$** Least Squares (LS) Regression [67] of the altimeter measurements, stacked as vector $\mathbf{y}_{alt}$, is employed at each estimation time $t_{est} \in [t_1, \ldots, t_{N_{alt}}]$. The

regression is used to calculate the smoothed value of the range $r(t_{est})$ and of the range-rate $\dot{r}(t_{est})$. Specifically, the coefficients $\hat{\mathbf{a}}$ of a time-polynomial of order $d_r$ are estimated by solving the LS problem defined in eq. (4.11) [41].
As the focus is on the position magnitude, the mean body radius $\bar{R}_{D1}$ is added to the altimeter measurement: $y_{r,i} = y_{alt,i} + \bar{R}_{D1}$. It's worth noting that a more refined correction could consider the intersection of the altimeter beam with a shape model, fitted to the known shape of the asteroid. Unfortunately, the lack of a position vector estimate, necessary to locate the shape model with respect to the spacecraft before computing the intersection, renders this not feasible.

$$\text{Find} \;\; \hat{\mathbf{a}} = \arg\min_{\mathbf{a}} ||\boldsymbol{\varepsilon}||_2 \quad \text{where} \quad \boldsymbol{\varepsilon} = \mathbf{y}_r - H\hat{\mathbf{a}} \tag{4.11}$$

The observation matrix H is assembled from the row vector $\mathbf{H}_i$, whose entries are computed from the $i^{th}$ timetag of each element $y_{r,i}$.

$$\mathbf{H}_i = \left[1, t^1, \ldots, t^{N_{poly}}\right] \qquad i = 1, \ldots, N_{alt}$$

Therefore:

$$H = \begin{bmatrix} \mathbf{H}_1 \\ \vdots \\ \mathbf{H}_{N_{alt}} \end{bmatrix}$$

eq. (4.12) shows the solution of the problem through inversion of the Normal Equations [67]. In practice, the actual implementation utilizes MATLAB `mldivide` instead of directly inverting the Information matrix. As a final note, it is recommended to scale the entries of the observation matrix to prevent ill-conditioning. In the implementation, a time grid is used in hours instead of seconds for this purpose. Consequently, all subsequent operations must consider this detail.

$$\hat{\mathbf{a}} = (H^T H)^{-1} H^T \mathbf{y}_r \tag{4.12}$$

The resulting time-polynomial (eq. (4.13)) is indeed a smoother of the range measurement over the time window covered by the buffer.

$$r(t) = \sum_{j=0}^{d_r} a_j \, t^j \tag{4.13}$$

By definition, the time-derivative of the range polynomial immediately yields the time-polynomial that approximates the range-rate over the same time window (eq. (4.14))

$$\dot{r}(t) = \sum_{j=0}^{d_r-1} j\,\hat{a}_{r,j}\,t^{j-1} \tag{4.14}$$

The values $r(t_{est})$ and $\dot{r}(t_{est})$ are thus readily computed by evaluating the smoothers in $t_{est}$ when the estimates are required.

**Variance of $r$ and $\dot{r}$** The estimation of the variance [67] is performed from the residuals of the smoothing relying on several assumptions that, while strong, are deemed necessary within this framework:

1. Uncorrelation between measurements in time.
2. The polynomial estimator is assumed to be unbiased.
3. Approximation of the variance of the polynomial estimator as the Root-Mean Square (RMS) of the residuals.
4. The random process is assumed to be stationary with a constant variance $\sigma^2$ over the given time frame.
5. The time variable is assumed as perfectly known (no uncertainty).

This approximation is founded on the understanding that the RMS of the post-fit residuals serves as empirical measure of the dispersion of the errors. Assuming the validity of the assumptions inherent to the Least Squares (LS) problem, this dispersion is caused by measurement noise only.
Initially, the residuals $\boldsymbol{\varepsilon}_r$ are computed for each entry of the observation vector $\mathbf{y}$. Its RMS is defined as eq. (4.15) and is used as approximation of the variance of the range estimate:

$$RMS(\boldsymbol{\varepsilon}_r) = \sqrt{\frac{1}{N_{alt}}\sum_{i=1}^{N_{alt}} \varepsilon_{r,i}} \quad \Rightarrow \quad \sigma_r^2 \approx RMS(\boldsymbol{\varepsilon}_r)^2. \tag{4.15}$$

As for the range-rate variance $\sigma_{\dot{r}}^2$, the model assumes the use of the finite forward difference formula to estimate the derivative (4.16).

$$\dot{r}_k \approx \frac{r_{k+1} - r_k}{t_{k+1} - t_k} \tag{4.16}$$

where $k+1$ and $k$ indicate two generic time instants. Following the aforementioned

assumptions and applying the variance "operator", $Var(x) = E[x - E[x]]$, to the model:

$$\hat{\sigma}_{\dot{r}}^2 \approx Var\left(\frac{r_{k+1} - r_k}{t_{k+1} - t_k}\right) \approx 2\left(\frac{RMS(\boldsymbol{\varepsilon}_r)}{t_{k+1} - t_k}\right)^2 \tag{4.17}$$

**Estimation and variance of $\dot{\theta}$** The same approach as described above is applied to estimate the required input $\dot{\theta}$. The true anomaly of the trajectory is inherently a property that cannot be directly observed. However, it was found that an approximation of its variation over a given $\Delta t$ is possible by computing the displacement of several Line of sight (Los) corresponding to the centroid measurements.
With the centroid coordinates in the image plane obtained from the IP algorithm, the Los is retrieved and rotated to the Inertial frame CI by means of the attitude quaternion estimate (4.18).

$$\begin{aligned} \mathbf{l}^{CI}(t) &= \texttt{DCM}\left(\hat{\mathbf{q}}_{CAMwrtCI}(t)\right)\mathbf{l}^{CAM}(t) \\ &= \texttt{DCM}(\hat{\mathbf{q}}_{CAMwrtCI}(t))\begin{bmatrix} cos(E(t))\ sin(A(t)) \\ -sin(A(t)) \\ cos(E(t))\ cos(A(t)) \end{bmatrix} \end{aligned} \tag{4.18}$$

where the spherical angles $E(t)$ and $A(t)$ identifying the Los in the CAM frame are obtained from the centroid coordinates (u, v) (4.19). Specifically, the line-of-sight expression assumes that the +Z axis of the CAM frame corresponds to the bore-sight of the camera. The camera intrinsic parameters [34] are also necessary, namely: the centre of the image plane $(c_x, c_y)$ and the non-dimensional focal length $f$.

$$\begin{cases} A(t) = atan2\left(\dfrac{u(t) - c_x}{f}\right) \\ E(t) = atan\left(-\dfrac{v(t) - c_y}{f}\ cos(A(t))\right) \end{cases} \tag{4.19}$$

The displacement $\theta_i$ at each $i^{th}$ time instant for the regression is then computed with respect to first valid $\mathbf{l}_{CI}(t_{w0})$ where $t_{w0}$ is the first time instant of the time window (4.20). Figure 4.2 sketches the process.

$$\theta(t) = \cos^{-1}\left(\mathbf{l}_{CI}(t) \cdot \mathbf{l}_{CI}(t_{w0})\right) \tag{4.20}$$

Proceeding through the same step as for the range time-polynomial, the displacement

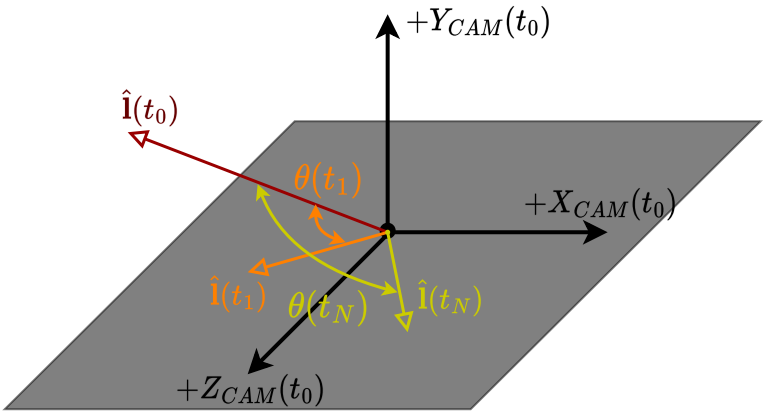


Figure 4.2: Representation of the line-of-sight vectors displacements with respect to the first in a window starting at time $t_0$.

time-polynomial is derived and subsequently differentiated to get the smoother of the displacement rate. This serves as the approximation for the true anomaly rate $\dot{\theta}$ (4.21).

$$\theta(t) = \sum_{j=0}^{d_{cen}} \hat{a}_{\theta,j}\, t^j \quad \Rightarrow \quad \dot{\theta}(t) = \sum_{j=0}^{d_{cen}-1} j\, \hat{a}_{\theta,j}\, t^{j-1} \tag{4.21}$$

Finally, the evaluation of eq. (4.21) at $t_{est}$ provides the value of $\dot{\theta}(t_{est})$ enabling the computation of $r_{CA}(t_{est})$. The variance of the estimate is then approximated similar to the range-rate, from the residuals of the fitting.

$$\hat{\sigma}^2_{\dot{\theta}} \approx Var\left(\frac{\theta_{k+1}-\theta_k}{t_{k+1}-t_k}\right) \approx 2\left(\frac{RMS(\varepsilon_\theta)}{t_{k+1}-t_k}\right)^2 \tag{4.22}$$

## 4.3. Keplerian dynamics "kepSRUSKF"

### 4.3.1. Filter design details

Most filters implementation in literature employs Cartesian coordinates $(\mathbf{r}, \mathbf{v})$ for the position and velocity of the spacecraft. Consequently, any dynamics model, including the simplest one (eq. (3.1)), necessitates numerical integration for time propagation. Indeed, this also represents the main difference in computational cost between the state-of-the-art EKF and Sigma Points filters, despite both having the same algorithmic complexity. Consequently, when analytical propagation is feasible, the second family of estimators becomes a convenient choice in the trade-off between accuracy, robustness and computational cost.

The filter was designed to use Osculating Keplerian elements in place of Cartesian Coordinates, enabling analytical propagation through the solution of Kepler's problem (4.3.3). However, since Hera trajectories are characterized by eccentricities larger than 1, the Hyperbolic anomaly is employed instead of the True anomaly.
Furthermore, to account for the non-negligible uncertainty in the properties of asteroids, the state vector of the filter is augmented to include the gravitational parameter $\mu_{D1}$ of the main body as considered parameter (for which the formulation is defined as "Schmidt"). Therefore, the complete state vector is given as (4.23).

$$\mathbf{z} = \left[a, e, i, \Omega, \omega, H, \mu_{D1}\right]^T \tag{4.23}$$

Another reason of this design choice is the easier and faster computation of the DCA as it is directly determined by the orbit shape states $(a, e)$:

$$\hat{r}_{CA} = \hat{a}(1 - \hat{e}) \;\text{ with } a < 0,\; e > 1 \tag{4.24}$$

Moreover, uncertainty propagation to get $\sigma^2_{\hat{r}_{CA}}$ can be directly carried out from the filter covariance without the need for decomposition. In contrast to the first algorithm, the Sigma Points capturing the state PDF are readily available from the filter steps.
The Square-Root form of the covariance is to be preferred in this context as it well aligns with the goal of minimizing computations compared to the standard Unscented Kalman Filter.

### 4.3.2. Filter initialization

The filter initialization takes place at the first time instant of the estimation process and requires the specification of the state vector and its initial covariance. Both are assigned in Cartesian coordinates assuming estimation accuracy and uncertainty compatible with the Ground orbit determination process (4.25). Furthermore, the correlation terms are set to zero since they are naturally built up during the execution of the filter. The propagation model plays a crucial role to correlate position and velocity states, enabling the estimation of non-observed states.

$$P_{\mathbf{x}_0} = \texttt{diag}\left(\left[300,\quad 300,\quad 300,\quad 0.01,\quad 0.01,\quad 0.01\right]^2\right)\; [m^2, m^2/s^2] \tag{4.25}$$

The gravitational parameter treated as considered state and its uncertainty, derived from the last available solution [36], are reported in 4.26. It's important to note that the

uncertainty on this parameter enters the estimation differently from the additive process noise.

$$\mu_{D1} = 32.3545\ [m^3/s^2] \qquad \sigma_{\mu_{D1}} = 1.4368\ [m^3/s^2] \tag{4.26}$$

Finally, augmentation with the considered parameters is performed. The correlation terms are again set to zero:

$$P_{\mathbf{z}_0} = \begin{bmatrix} P_{\mathbf{x}_0} & \mathbf{0}_{6,1} \\ \mathbf{0}_{1,6} & \sigma^2_{\mu_{D1}} \end{bmatrix} \quad [m^2, m^2/s^2, m^6/s^4]$$

The initial Keplerian state vector is computed through the coordinates transformation by means of the UT. It is important to highlight that the state vector in Keplerian elements necessarily has non-zero correlation terms when converted from Cartesian coordinates. The Square Root of the Covariance matrix is initialized as in eq. (2.4). The initial set of Sigma points $\boldsymbol{\chi}_{i,0}\ , i = 0, \ldots 2N_z$ describing the state PDF is immediately generated, together with the corresponding weights as shown in section 2.3.1.

### 4.3.3. Filter Time Update

The prediction of the state vector over *any* $\Delta t$ only requires the computation of a single component, namely the fast variable $H(t)$. Contrarily to numerical integration, the computational effort for this task is independent of the $\Delta t$ thanks to the analytical solution. From a generic time instant $t_k$ the forward prediction to the subsequent filter time $t_{k+1}$ in discrete form is performed through three steps. Firstly, the Mean anomaly $M_k$ is computed from the current value of the Hyperbolic anomaly $H_k$.

$$M_k = e_k\, sinh(H_k) - H_k \tag{4.27}$$

Secondly, it is updated by means of (eq. (4.28)) propagating for the required $\Delta t_k = t_{k+1} - t_k$.

$$M_{k+1} = M_k + \sqrt{\frac{\mu}{-a_k^3}}\,\Delta t_k \tag{4.28}$$

Finally, the updated Hyperbolic anomaly is computed through Newton-Raphson method, iterating through equation 4.29 with index $j$ until the stopping criterion $|H_{j+1} - H_j| \leq tol$ is satisfied [72]. The tolerance was set to $10^{-8}\, rad$ for this study, to prevent an excessive number of iterations.

$$H_{j+1} = H_j + \frac{M_{k+1} - e_k\, sinh(H_j) + H_j}{e_k\, cosh(H_j) - 1} \tag{4.29}$$

All the other components remain constant during the Time Update and are simply assigned to the array of the propagated state:

$$\begin{cases} a_{k+1} = a_k \\ e_{k+1} = e_k \\ i_{k+1} = i_k \\ \Omega_{k+1} = \Omega_k \\ \omega_{k+1} = \omega_k \end{cases} \tag{4.30}$$

The propagation function defined by the steps 4.28 to 4.30 is denoted as `kepProp`() in the following. Every sigma point is independently propagated.

$$\boldsymbol{\chi}_{i,k+1} = \texttt{kepProp}(\boldsymbol{\chi}_{i,k}, \Delta t) \qquad i = 0, \ldots, 2N_z \tag{4.31}$$

The mean state estimate is then computed as weighted sample mean of the Sigma Points (eq. (4.32))

$$\hat{\mathbf{z}}^-_{k+1} = \sum_{i=0}^{2N_z} W_i^{(m)} \boldsymbol{\chi}_{i,k+1} \tag{4.32}$$

The associated full covariance can be computed as weighted sample covariance (eq. (4.33)) if needed.

$$P_{k+1} = \sum_{i=0}^{2N_z} W_i^{(c)} (\boldsymbol{\chi}_{i,k+1} - \hat{\mathbf{z}}^-_{k+1})(\boldsymbol{\chi}_{i,k+1} - \hat{\mathbf{z}}^-_{k+1})^T \tag{4.33}$$

In the Square-Root form, this operation is replaced by a two-step procedure involving QR decomposition and Cholesky Rank-1 Update algorithm [69, 75]. The reason of the second step is that the weight associated with the mean state $W_1^m$ is always negative for the number of components involved in Orbit determination problems [28] and for the common tuning parameters of the Unscented Transform (section 2.3.1). Therefore, the Time Update is finalized by applying eq. (4.34) and eq. (4.35).

$$S^-_{zz,k+1} = \texttt{QR}\left\{ \left[ \sqrt{W^c_{1:2N_z}} (\boldsymbol{\chi}_{1:N_z,k+1} - \hat{\mathbf{z}}^-_{k+1}) \quad \sqrt{Q_k} \right] \right\} \tag{4.34}$$

$$S^-_{zz,k+1} = \texttt{cholupdate}\left( S^-_{zz,k+1},\ \sqrt{|W^c_0|}(\boldsymbol{\chi}_{0,k+1}) - \hat{\mathbf{z}}^-_{k+1}),\ sign\,(W^c_0) \right) \tag{4.35}$$

where $\sqrt{Q_k}$ is the Square Root matrix of the Process noise covariance matrix. An important detail to recognize is that when using the UT for the Time Update in place of methods that avoid negative weights such as the Conjugate UT, the operation in eq. (4.35)

can disrupt the positive definiteness of the matrix [3]. This is because the `cholupdate` operationis is equivalent to computing the Cholesky decomposition of the matrix difference of two positive definite matrices, which is *not* guaranteed to be positive definite. This investigation found out that this occurrence is the most frequent cause for the filter to stop functioning, specifically in three situations:

1. Process noise not correctly tuned, i.e., far from the optimal value to "cover" the non-modeled effects of the dynamics.
2. Incipient filter divergence in one or more states caused by an excessive sudden drop following a very accurate measurement.
3. When the covariance of states bounded to assume values in a closed interval (e.g. the anomaly for hyperbolic orbits) increases such that it covers unfeasible regions of the state space.

The tuning process was performed in an attempt to cover the "gaps" of the Keplerian parameters with respect to the nominal Osculating values (fig. 3.7), oscillating and drifting respectively due to the $3^{rd}$ body perturbation and the SRP. Specifically, the $Q$ matrix was tuned separately depending on whether the altimeter is enabled. The dimensions of the entries are the squares of the state vector ones.

$$Q_1^{Kep} = \texttt{diag}\left(\left[0.2,\ \ 1\times10^{-5},\ \ 1\times10^{-8},\ \ 1\times10^{-8},\ \ 1\times10^{-8},\ \ 1\times10^{-2}\right]^2\right)$$

$$Q_2^{Kep} = \texttt{diag}\left(\left[1.5,\ \ 1\times10^{-5},\ \ 1\times10^{-6},\ \ 1\times10^{-6},\ \ 1\times10^{-6},\ \ 1\times10^{-3}\right]^2\right)$$

### 4.3.4. Filter Observation Update

The observation update of the filter consists in the incorporation of the altimeter and centroiding measurements as they become available for processing. The general observation models described in the following utilize Cartesian coordinates. Conversion of the Keplerian elements state is therefore performed prior evaluation, even if not explicitly specified.

**Pre-processing and consistency check** Each measurement enters the filter with a timetag indicating the acquisition time and a validity flag. A flag *bHoldUpdate* was added in the conditional statement such that the filter can be forced to skip the Update step (i.e., to work in pure propagation) whenever measurements are labelled as invalid.
If a centroid observation $(u, v)$ is available, the filter manager checks for its physical

consistency. Given the size in pixels of the image plane of the AFC (3), the measurements is accepted if the centroid coordinates are within 0.95 of the image plane size $I_{lim}$ (the coordinates are with respect to the centre position $c_x, c_y$):

$$\begin{cases} |\,(u - c_x)\,| < 0.95\ I_{lim} \\ |\,(v - c_y)\,| < 0.95\ I_{lim} \end{cases}$$

and rejected otherwise, either skipping the update or incorporating the altimeter measurement only.
The altimeter is instead considered valid if the measurement is positive and below the maximum measurable distance:

$$\begin{cases} r_{Alt} > 0 \\ r_{Alt} \leq 16\ km \end{cases}$$

As a side note, the implementation was carried out avoiding the use of variable-size arrays at the input/output interfaces of the filter. Instead, indexing based on the validity flags is exploited. This design allows for the easy addition of any other rejection or pre-processing step if needed.

**Measurement delay handling** In real implementations of navigation filters, measurements are not immediately available as acquired by the sensors. A delay, possibly lasting several seconds (e.g., due to image processing run-time [43]), must be accounted for when incorporating measurements. It is worth noting that this is not strictly necessary if a delay in the Failure detection (FD) assessment is allowed. In this case, the filter runs in a delayed manner, waiting for the measurement to become available. The latter is the default option for the presented design, but the procedure was anyway implemented.
Unlike the EKF for which more efficient alternatives exist e.g., [18]), back-propagation is necessary for Sigma points filters. The timetags of the measurements are first compared to the current OBSW clock time to determine whether a delay $t_d$ between acquisition and availability time exists.

$$t_{d,alt} = t_{alt} - t_{OBSW} \leq 0\,; \qquad t_{d,cen} = t_{cen} - t_{OBSW} \leq 0$$

The propagation function (4.31) is then applied identically by simply selecting $\Delta t = t_d$ to obtain the sigma points at the observation times $t_{alt}$ or $t_{cen}$, indicated as $\boldsymbol{\chi}_{i,m}$ for conciseness.
The observation models for the altimeter and the centroid are finally evaluated at the

time of the measurement to obtain their prediction. The models are presented in the following in their general form for use with either Didymos or Dimorphos, at a generic time instant k (the subscript is omitted).

**Altimeter observation model** The altimeter observation model predicts the altimeter measurement from the spacecraft to the surface of the target body. The attitude quaternion of the spacecraft with respect to the CI frame, $\hat{\mathbf{q}}_{SCBwrtCI}$, is assumed perfectly known from the attitude determination filter. Indeed, there is no alternative when only centroiding measurements are available to the translational navigation.
The shape models used for both Didymos and Dimorphos, detailed in [58], consists in four triaxial ellipsoids. This approach enhances the accuracy compared to a single ellipsoid, since each of the four ellipsoid is tailored to fit only one quadrant of the target body. For computational efficiency, the observation model is evaluated in the target body frame instead of the CI eliminating the need for rotating the ellipsoids.
The altimeter Los is rotated to the TB frame using the knowledge of the DCM describing the attitude of the target at the time instant of interest (4.36).

$$\mathbf{l}_{alt}^{TB} = \mathrm{DCM}_{TBwrtCI}\ \mathrm{DCM}(\hat{\mathbf{q}}_{SCBwrtCI})\ \mathbf{l}_{alt}^{SCB} \tag{4.36}$$

The relative position of the Spacecraft with respect to the target body is computed in the CI frame and similarly rotated to the TB.

$$\hat{\mathbf{r}}_{SCwrtTB}^{TB} = \mathrm{DCM}_{TBwrtCI}\ \left(\hat{\mathbf{r}}_{SC}^{CI} - \mathbf{r}_{TB}^{CI}\right) \tag{4.37}$$

where $\mathbf{r}_{TB}^{CI}$ is a vector of zeros if Didymos is the target, the ephemerides of Dimorphos' position otherwise.
The relative position (4.37) and the altimeter Los are firstly used to approximately determine the quadrant of the intersection to select one of the four ellipsoids. Subsequently, the actual intersection distance $r_{intersec}$ with the shape model is determined along the altimeter Los and subtracted from the position vector norm to obtain the prediction of the altimeter measurement (eq. (4.38)).

$$y_{alt} = ||\hat{\mathbf{r}}_{SCwrtTB}|| - r_{intersec} \tag{4.38}$$

In case no intersection solution is found, a flag is raised prompting the filter to skip the altimeter measurement incorporation. A subsequent check of the physical consistency of the prediction based on the sizes of the target bodies is added through the same flag. The

prediction is marked as invalid if the intersection distance exceeds a threshold determined by the diameter of the target bodies:

$$\begin{matrix} r_{intersec} \geq 800\ [m] & \text{if D1} \\ r_{intersec} \geq 400\ [m] & \text{if D2} \end{matrix} \Rightarrow \text{Reject meas.}$$

**Centroiding observation models** The centroiding model provides the predicted coordinates of the centre of mass for Didymos and the centre of brightness for Dimorphos, considering that two different IP are employed (see chapter 3). Both models are based on the pinhole projection model, the only difference being that the second needs to account for the Sun Phase angle by including a centroid correction term.
The pinhole projection [34] is the simplest camera model possible allowing the computation of image plane coordinates for any point with known coordinates in the camera reference frame given the Intrinsic and Extrinsic camera parameters. The former are contained in the Camera calibration matrix $K_{CAM}$, while the latter includes the position of the camera frame origin and the attitude of the CAM frame in CI. The filter estimates the first of these two states.

$$\begin{bmatrix} x_p \\ y_p \\ z_p \end{bmatrix}_{CAM} = K_{CAM}\, \text{DCM}\ (\hat{\mathbf{q}}_{CAMwrtCI}) \begin{bmatrix} I_3 & -\hat{\mathbf{r}}_{SC}^{CI} \end{bmatrix} \begin{bmatrix} \mathbf{p}^{CI} \\ 1 \end{bmatrix} \tag{4.39}$$

where $\mathbf{p}^{CI}$ is the position vector in CI of the point to project. Since the center of the two asteroids is the target that the IP algorithms attempt to extract, $\mathbf{p}^{CI}$ must be equal to $[0,0,0]^T$ if Didymos is the target; and equal to the position of Dimorphos $\mathbf{r}_{SB}^{CI}$ as available from the on-board ephemerides. The pixel coordinates in the image plane are finally computed by normalizing with respect to the $3^{rd}$ components, as monocular cameras are not able to provide distance information:

$$\begin{bmatrix} u \\ v \end{bmatrix} = \begin{bmatrix} \frac{x_p}{z_p} \\ \frac{y_p}{z_p} \end{bmatrix} \tag{4.40}$$

**Centre of Brightness correction** The coordinates obtained by (4.40) must be shifted to account for the Sun Phase angle when the CoB algorithm is being applied. More in detail, eq. (4.41) corrects the prediction to make it closer to the output of the IP. The magnitude of the correction is computed based on an analytical model of the centre of brightness shift for a spherical body illuminated by the sunlight. The direction of the shift

line corresponds to the projection of the unit direction toward the Sun onto the image plane $\mathbf{u}_{Sun} = [x_{Sun},\ y_{Sun}]^T$.

$$\begin{bmatrix} u \\ v \end{bmatrix}_{CoB} = \begin{bmatrix} u \\ v \end{bmatrix} + \frac{4}{3\pi}\left(1 - cos\,\theta_{SB}\right)\bar{R}_{SB,pix}\,\mathbf{u}_{Sun} \tag{4.41}$$

Eq. 4.41 shows the correction term expression, in which $\theta_{SB}$ is the Sun phase angle with respect to the secondary body (4.42); $\bar{R}_{SB,pix}$ is the average size of Dimorphos in pixels, computed as (eq. (4.43)) and $\bar{R}_{SB} = 82$ [m].

$$\theta_{SB} = cos^{-1}\left(\frac{\hat{\mathbf{r}}^{CI}_{SC} - \mathbf{r}^{CI}_{SB}}{||\hat{\mathbf{r}}^{CI}_{SC} - \mathbf{r}^{CI}_{SB}||} \cdot \mathbf{l}^{CI}_{Sun}\right)\ [rad] \tag{4.42}$$

$$\bar{R}_{SB,pix} = sin^{-1}\left(\frac{\bar{R}_{SB}}{||\hat{\mathbf{r}}^{CI}_{SC} - \mathbf{r}^{CI}_{SB}||}\right)\frac{N_{pix}}{FoV}\ [pix] \tag{4.43}$$

The Sun Phase angle value for the secondary body is also compared to $\pi/2$ as consistency check. The update is rejected if the condition $\theta_{SB} \geq \pi/2$ is satisfied, as it is not be possible to have CoB observation without Sun illumination.

**Innovation computation and outliers detection** Depending on the validity flags computed during the pre-processing, the Altimeter and the Centroid observation models are evaluated for each a priori Sigma point $\boldsymbol{\chi}^{-}_{i,k}$ $i = 0, \ldots, 2N_z$ to obtain their mapping $\boldsymbol{\Upsilon}_{i,k}$ in the Observation space. This set of sigma points in turn describes the map of the state PDF necessary for the computation of the Innovation. The approximation of the predicted mean and Square Root covariance of the innovation is retrieved through (4.44, 4.45) [28, 75].

$$\hat{\mathbf{y}}_k = \sum_{i=0}^{2N_z} W_i^{(m)} \boldsymbol{\Upsilon}_{i,k} \tag{4.44}$$

$$\begin{aligned} S_{yy,k} &= \mathtt{QR}\left\{\left[\sqrt{W^c_{1:2N_z}}(\boldsymbol{\Upsilon}_{1:N_z,k} - \hat{\mathbf{y}}_k) \quad \sqrt{R_k}\right]\right\} \\ S_{yy,k} &= \mathtt{cholupdate}\left(S_{yy,k},\ \sqrt{|W^c_0|}(\boldsymbol{\Upsilon}_{0,k} - \hat{\mathbf{y}}_k),\ sign\left(W^c_0\right)\right) \end{aligned} \tag{4.45}$$

where $R_k$ is the measurements noise covariance. The design assumes a diagonal matrix with altimeter $\sigma_{Alt} = 40\,m$; the centroiding covariance sub-matrix is computed through a non-linear function of the prior estimated state, given the expected covariance at a specified distance. The $\sigma_{Cen}$, identical for both coordinates, ranges from 2 to 200 pixels. TWhile the details are omitted, it is noted that this approach enhances the filter performance by accounting for the fact that the measurement noise statistics vary dur-

ing the navigation window. The Innovation vector $\boldsymbol{\upsilon}_k$ is simply the difference between observations and its predicted mean:

$$\boldsymbol{\upsilon}_k = \tilde{\mathbf{y}}_k - \hat{\mathbf{y}}_k$$

In practical application, the quality of the state estimation is often improved adopting a measurements outlier rejection strategy (i.e., "editing" [10]). Conceptually, the filter evaluates a distance metric based on how large the residual is compared to the Innovation covariance and decides whether to reject the update. It is crucial to note that both the measurement noise covariance $R_k$ associated to the actual observables and the map of the state estimate covariance $P_{zz,k}$ play a role in this regard. The expression of the first order linearization (EKF) makes these two contributions more evident, whereas in the SRUSKF they are embedded in the $S_{yy}$ computation step:

$$P_{yy,k}^{EKF} = H_k^T P_{zz,k}^- H_k + R_k \tag{4.46}$$

where $H_k = \left.\dfrac{\partial \mathbf{h}}{\partial \mathbf{z}}\right|_{\hat{z}_k^-}$ is the jacobian of the observation function with respect to the state vector. Indeed, the editing step must be carefully designed to avoid incorrect rejection of new observations by the filter.
The squared Mahalanobis distance [15, 21] is employed to assess the residuals for potential outliers. If the condition (eq. (4.47)) is met, the filter accepts the update.

$$M^2\left(\boldsymbol{\upsilon}_k, S_{yy,k}\right) = \boldsymbol{\upsilon}_k^T P_{yy}^{-1} \upsilon_k \ \leq M_{thr}^2 \tag{4.47}$$

where $M_{thr}$ is selected equal to 4. As for the implementation, it's worth noting that the inversion of the full covariance is avoided. Instead, the equivalent linear system involving the Square root covariance (upper triangular) is solved in two steps using MATLAB `mrdivide` (4.48).

$$M^2\left(\boldsymbol{\upsilon}_k, S_{yy,k}\right) = \left(\left(\boldsymbol{\upsilon}_k^T / S_{yy,k}\right) / S_{yy,k}^T\right) \boldsymbol{\upsilon}_k \tag{4.48}$$

**State and covariance update** After determining the accepted residuals entries using the validity flags, the state-observation cross-covariance and the optimal Kalman gain are computed with eq. (4.49), eq. (4.50), respectively.

$$P_{\mathbf{zy},k} = \sum_{i=0}^{2N_z} \left(\boldsymbol{\chi}_i - \hat{\mathbf{z}}_k^-\right) \left(\boldsymbol{\Upsilon}_{i,k} - \hat{\mathbf{y}}_k\right)^T \tag{4.49}$$

$$K_k = \begin{bmatrix} K_{\mathbf{x},k} \\ K_{\mathbf{p},k} \end{bmatrix} = \left(P_{\mathbf{zy}}/S_{yy,k}\right)/S_{yy,k}^T \tag{4.50}$$

The Kalman gain can be partitioned in two sub-matrices, one for the state vector and one for the parameters, respectively. This partition is necessary because the second gain must be set to zero when the additional parameters are considered and not solved for. The mean state estimate is then updated as given in (4.51).

$$\hat{\mathbf{z}}_k^+ = \hat{\mathbf{z}}_k^- + \begin{bmatrix} K_{\mathbf{x},k} \\ 0_{N_p,N_\nu} \end{bmatrix} \boldsymbol{\upsilon}_k \tag{4.51}$$

where $N_p$ is the number of parameters, $N_\nu$ is the size of the innovation vector. The state covariance is updated in two stages by means of the auxiliary matrices $U_1$ and $U_2$ (4.52). Depending on the Innovation covariance and the Kalman gain, the first stage (4.53) shrinks the uncertainty, while the second (eq. (4.54)) expands it by an amount dependent on the consider parameters variance [80].

$$U_{1,k} = K_k S_{\mathbf{yy}_k} \qquad U_{2,k} = \begin{bmatrix} 0_{N_x} \\ K_p \end{bmatrix} S_{\mathbf{yy}_k} \tag{4.52}$$

Cholesky Rank-1 Update is used column by column to update the Square Root covariance.

$$S_{\mathbf{zz}_k}^+ \leftarrow S_{\mathbf{zz}_k}^- \Rightarrow S_{\mathbf{zz}_k}^+ = \texttt{cholupdate}\left(S_{\mathbf{zz}_k}^+, U_{1,k}, -1\right) \tag{4.53}$$

$$S_{\mathbf{zz}_k}^+ = \texttt{cholupdate}\left(S_{\mathbf{zz}_k}^+, U_{2,k}, +1\right) \tag{4.54}$$

This completes the execution of one Time-Observation update cycle of the filter, yielding the posterior state and Square Root covariance estimates. The latter ones are then used to start the next cycle from 4.3.3.

### 4.3.5. Manoeuvre execution

As explained in chapter 3 the baseline trajectory of the EXP phase includes two autonomous manoeuvres commanded by the GNC. Therefore, it is necessary to incorporate them in the estimation process, accounting for both mean state adjustments and added dispersion. The on-board guidance computes the commanded $\Delta\mathbf{v}$, which is then mapped to a thrust vector command.

To include this input in the estimation, the discrete $\Delta\mathbf{v}_k$ is added at each time step $k$ to the set of Sigma points parameterizing the state PDF. Specifically, the set is ini-

tially computed given the mean state and Square Root covariance in Keplerian elements, Subsequently, it is mapped to Cartesian coordinates and the $\Delta\mathbf{v}_k$ is added:

$$\boldsymbol{\chi}_{i,k}^{Cart} = \boldsymbol{\chi}_{i,k}^{Cart} + \begin{bmatrix} \mathbf{0}_{3,1} \\ \Delta\mathbf{v}_k \\ 0 \end{bmatrix} \tag{4.55}$$

The full covariance is reconstructed using (2.8). The dispersion introduced by the manoeuvre expands the orbital state covariance sub-matrix by an amount $P_{man}$ (4.56). $P_{man}$ is computed based on the dispersions $\sigma_{mag}^2$ and $\sigma_{dir}^2$ (4.57 to 4.59). It's important to note that the simple addition assumes no correlation between the state vector covariance and $P_{\text{man}}$.

$$P_{\mathbf{zz}} = P_{\mathbf{zz}} + \begin{bmatrix} P_{man} & \mathbf{0}_{6,1} \\ \mathbf{0}_{1,6} & 0 \end{bmatrix} \tag{4.56}$$

The dispersion $\sigma_{mag}^2$ represents the uncertainty in $||\Delta\mathbf{v}||$ along the thrust vector direction $\mathbf{Z}_{\Delta\mathbf{v}} = \Delta\mathbf{v}/||\Delta\mathbf{v}||$; $\sigma_{dir}^2$ represents the uncertainty in the knowledge of this direction (4.1). The matrix $P_{man}$ is assembled as diagonal in a reference frame attached to the thrust vector direction (4.57).

Table 4.1: Dispersion values for manoeuvres.

| | |
|---|---|
| $\sigma_{mag}$ | 0.005 $[m/s]$ |
| $\sigma_{dir}$ | 2.5 $[deg]$ |

$$P_{man}^{\Delta\mathbf{v}} = \frac{1}{2}||\Delta\mathbf{v}||^2 \texttt{diag} \left( \begin{bmatrix} \sigma_{dir}^2(\sigma_{mag}^2 + 1 - \sigma_{dir}^2) \\ \sigma_{dir}^2(\sigma_{mag}^2 + 1 - \sigma_{dir}^2) \\ \sigma_{mag}^2(1 - \sigma_{dir}^2) + \frac{3}{4}\sigma_{dir}^4 \end{bmatrix}^T \right) \tag{4.57}$$

Any choice of the axes $+X_{\Delta\mathbf{v}}$ and $+Y_{\Delta\mathbf{v}}$ is allowed, provided that they are orthogonal to the thrust vector direction. To achieve this, a random axis $\mathbf{l}_{rnd}$ is first generated, from which the component perpendicular to the $\mathbf{Z}_{\Delta\mathbf{v}}$ axis is then computed (4.58).

$$\mathbf{X}_{\Delta\mathbf{v}} = \mathbf{l}_{rnd} - (\mathbf{l}_{rnd} \cdot \mathbf{Z}_{\Delta\mathbf{v}})\, \mathbf{Z}_{\Delta\mathbf{v}} \tag{4.58}$$

The third axis completes the triad, such that the rotation matrix between the spacecraft Body frame and the thrusting THR frame is completely specified: $\mathbf{Y}_{\Delta\mathbf{v}} = (\mathbf{Z}_{\Delta\mathbf{v}} \times \mathbf{X}_{\Delta\mathbf{v}})/||(\mathbf{Z}_{\Delta\mathbf{v}} \times \mathbf{X}_{\Delta\mathbf{v}})||$. Finally, the diagonal matrix (4.57) is rotated to the SCB to

compute $P_{man}$ (4.59).

$$R_{Man2CI} = \left[\mathbf{X}_{\Delta\mathbf{v}},\ \ \mathbf{Y}_{\Delta\mathbf{v}},\ \ \mathbf{Z}_{\Delta\mathbf{v}}\right] \ \Rightarrow\ P_{man} = R_{Man2CI}\, P_{Man}^{\Delta\mathbf{v}}\, R_{Man2CI}^{T} \tag{4.59}$$

## 4.4. Higher Fidelity SRUSKF

A slightly modified filter was implemented to assess the extent of the accuracy degradation resulting both from using Keplerian elements state compared to Cartesian coordinates and from the simplified dynamics.
The key distinction lies in the Time Update as detailed in the following 4.4.1. While the Observation Update remains unchanged, the transformation of the state to Cartesian coordinates for the evaluation is no longer necessary. For brevity, this section exclusively highlights the relevant modifications.

### 4.4.1. Filter design details

The augmented state vector in Cartesian coordinates becomes:

$$\mathbf{z} = \left[r_x,\, r_y,\, r_z,\, v_x,\, v_y,\, v_z,\, \mu_{D1}\right]^T$$

Two tuning sets are defined for the process noise covariance matrix. The first is used when only centroid information is available, the second after the altimeter activation:

$$Q_1^{HF} = \texttt{diag}\left(\left[10,\ \ 10,\ \ 10,\ \ 5\times10^{-11},\ \ 5\times10^{-11},\ \ 5\times10^{-11}\right]^2\right)$$

$$Q_2^{HF} = \texttt{diag}\left(\left[15,\ \ 15,\ \ 15,\ \ 1\times10^{-12},\ \ 1\times10^{-12},\ \ 1\times10^{-12}\right]^2\right)$$

An additional practical consideration regarding the tuning of the process noise pertains to the physical interpretation of the state vector. Unlike Keplerian elements, Cartesian coordinates offer an intuitive understanding of how the process noise impacts the estimation which definitely aids the procedure.

### 4.4.2. Time Update

The Time update now requires the solution of the numerical integration of an ODE system at each time step. A simple Euler integration scheme is employed. The timestep $\Delta t$ is fixed equal to the base frequency of the GNC functionality execution, namely $1\,s$.

The dynamical characterization in chapter 3 shows that a more refined dynamical model of the system shall comprise at least the $3^{rd}$ gravitational attraction of Dimorphos and the SRP due to their significant contributions to the total acceleration. The OBSW has to provide the position ephemerides of both bodies. The Sun gravitational attraction is included as well since all the required data for its computation are already necessary for the SRP.

$$\dot{\mathbf{z}}(t) = \begin{bmatrix} \mathbf{v}(t) \\ -\frac{\mu_{D1}}{r^3}\mathbf{r}(t) + \mathbf{a}_{D2,3rd}(t) + \mathbf{a}_{Sun,3rd}(t) + \mathbf{a}_{SRP}(t) + \frac{\mathbf{T}(t)}{m_{SC}} \\ 0 \end{bmatrix} \tag{4.60}$$

Eq. 4.60 presents the dynamics model in continuous time, including the acceleration due to the thrust $\mathbf{T}(t)$. Specifically, this term is computed based on the thrust vector commanded by the translational control during impulsive manoeuvres since the Hera spacecraft has no "closed-loop" information on the actual thrust. The perturbation acceleration terms are computed as previously described in chapter 3, without any variation in the parameters values.
The discrete propagation function corresponding to (4.60) is finally obtained by applying the Euler integration scheme (4.61). The propagation function is applied to each sigma point and the state PDF then reconstructed by means of (2.7 and 2.8).

$$\mathbf{z}_{k+1} = \mathbf{z}_k + \Delta t\ \dot{\mathbf{z}}_k \tag{4.61}$$

### 4.4.3. Closest approach assessment

In this context the estimation of the state vector is an intermediate step as the primary objective is to determine the distance at closest approach. The presented filter formulation offers a significant advantage due to its Square Root form: it allows the representation of the state PDF in terms of Sigma points at any time through simple addition operations (2.5). Uncertainty propagation for the computation of ($\mu_{\hat{r}_{CA}}$, $\sigma^2_{\hat{r}_{CA}}$) is readily performed through functions (4.24) and (4.10) downstream of the kepSRUSKF and the HF SRUSKF, respectively. Finally, the same strategy presented in section 4.2.1 is applied to address the decision problem.

## 4.5. Wald Sequential Probability Ratio Test (SPRT) using constrained filters bank

The third strategy builds upon the previously described filters (4.2.3). In this approach, two identical filters are combined in a bank, meaning they run in parallel to process the acquired observations. Unlike the former methods the "CAM flag", which determines the suggestion to the OBSW to maneuver, comes directly as the output of the SPRT. In other words, the threshold-based decision is replaced eliminating the need for all the assumptions described in section 4.2.1. The mathematical framework and the tailoring for the collision assessment problem are explained next (section 4.5.1).

**Mathematical formulation** Given a set of realization of random variables $\mathbf{Y_{1:k}} = \{\mathbf{y}_1, \ldots, \mathbf{y}_k\}$, which in the present case are the Innovations (i.e. difference between measured and predicted measurements) at each time instant, the unconstrained Joint Probability density function can be expressed sequentially:

$$p(\mathbf{Y_{1:k}}) = p(\mathbf{y}_k|\mathbf{Y}_{1:k-1})p(\mathbf{Y}_{1:k-1}) \tag{4.62}$$

The measurements can be processed by either the filter, regardless of their state vector. Any practical application requires assumptions about these probability density functions (PDFs).
In principle, the innovation vector $\boldsymbol{\varepsilon_k}$ of the estimator should exhibit the characteristics of a Gaussian zero-mean white noise. This allows the approximation of eq. (4.62) by a Gaussian distribution with a mean equal to the residual vector and a covariance given by the Innovation covariance.

$$p(\mathbf{y}_k|\mathbf{Y}_{1:k-1}) \simeq N\left(\boldsymbol{\varepsilon}_{k|1:k-1}, W_{k|1:k-1}\right) \tag{4.63}$$

Note that both are outputs of the observation step of *any* Kalman sequential estimator. The key difference lies in the way the innovation and its covariance are formed. In the EKF linearization (4.46) is used, while the UKF employs the Unscented Transform. The Innovation covariance is formed from the square root: $W_{k|1:k-1} = S^T_{k|1:k-1}S_{k|1:k-1}$ where $S_{k|1:k-1}$ is upper triangular.
Therefore, the Likelihood ratio at time $t_k$ used in the evaluation of the test, is expressed in its general and approximated form by eq. (4.64). The PDFs of the innovations of the

two filters must be constrained to the respective hypotheses, as described next.

$$\Lambda_k = \frac{p\left(\mathbf{Y}_{1:k}|H_1\right)}{p\left(\mathbf{Y}_{1:k}|H_0\right)} \simeq \frac{N\left(\boldsymbol{\varepsilon}_{k|1:k-1,H_1}, W_{k|1:k-1,H_1}\right)}{N\left(\boldsymbol{\varepsilon}_{k|1:k-1,H_0}, W_{k|1:k-1,H_0}\right)} \tag{4.64}$$

The significance of this ratio derives from the interpretation of the innovation PDFs of the two filters. A higher computed value is obtained if the mean innovation gets closer to zero with an upper bound determined by the covariance. Since the integral of a PDF over the entire space equals to 1 by definition of probability, the maximum absolute value the PDF can assume is limited by its "spread". In filtering terms, as the evaluation point moves farther from the mean and the innovation covariance increases, the value entering the ratio for the $i^{th}$ filter decreases. Hence, the constraint (i.e., hypothesis) makes one of the two filters matching more the actual observations, up to the extreme point in which the complementary may no longer predict physical measurements. This aspect is further discussed in section 4.5.5. In this work the evaluation of the PDF (Gaussian, eq. (4.65)) is performed at zero for the assumptions on the residual process at steady state, yielding a value in the interval $[0, 1]$ after each observation update.

$$N(\mathbf{x}; \boldsymbol{\mu}, \Sigma) = \frac{1}{(2\pi)^{1/N} det(\Sigma)} exp\left((\mathbf{x} - \boldsymbol{\mu})\Sigma^{-1}(\mathbf{x} - \boldsymbol{\mu})^T\right) \tag{4.65}$$

with N being the number of dimensions and $\mathbf{x}$ the point of evaluation. Following from eq. (4.62), the $\Lambda$ ratio is updated sequentially:

$$\Lambda_k = \frac{N\left(\mathbf{0};\ \boldsymbol{\varepsilon}_{k|k-1,H_1}, W_{k|k-1,H_1}\right)}{N\left(\mathbf{0};\ \boldsymbol{\varepsilon}_{k|k-1,H_0}, W_{k|k-1,H_0}\right)} \Lambda_{k-1}$$

**Decision step** Based on the targeted missed detection and false alarm probabilities, the decision bounds of the test, $A$ and $B$, are computed as 4.66 and 4.67, respectively. These expressions are suggested by A. Wald [78], but there is no established method to compute them. Intuitively, these thresholds signify that the alternative hypothesis $H_1$ is accepted if it is A times more likely than the Null one; conversely one should accept the Null hypothesis $H_0$ if it is $1/B$ times more likely that the alternative.

$$A = \frac{1 - \bar{P}_{fa}}{\bar{P}_{md}} \tag{4.66}$$

$$B = \frac{\bar{P}_{fa}}{1 - \bar{P}_{md}} \tag{4.67}$$

where $\bar{P}_{md}$ and $\bar{P}_{fa}$ are the targeted missed detection and false alarm probabilities.
It can be proved that the procedure terminates with probability equal to 1 (i.e., a decision is made), if either of the following conditions is satisfied:

$$\begin{cases} \Lambda_k \geq A \;\Rightarrow\; H_0 \text{ rejected} \\ \Lambda_k \leq B \;\Rightarrow\; H_1 \text{ rejected} \end{cases} \tag{4.68}$$

Otherwise, if the likelihood ratio does not exceed any of the two boundaries:

$$B < \Lambda_k < A \;\Rightarrow\; \text{Uncertain: seek new observations}$$

A note about the guarantees of the method in terms of rate error is now in order. As noted by [12], the relations (4.66, 4.67) cannot guarantee that the error rates are exactly within the accepted probabilities of error. In fact, eq. (4.68) leads to decision that satisfies the "true" (but unknown) bounds:

$$A \leq \frac{1 - P_{fa}}{P_{md}} \qquad B \geq \frac{P_{fa}}{1 - P_{md}}$$

In other words, the test does not guarantee that the ideal inequalities $P_{fa} \leq \bar{P}_{fa}$ and $P_{md} \leq \bar{P}_{md}$ hold, but only the weaker conditions:

$$P_{fa} \leq \frac{\bar{P}_{fa}}{1 - \bar{P}_{md}} \qquad P_{md} \leq \frac{\bar{P}_{md}}{1 - \bar{P}_{fa}}$$

The consequence is that at most one of the true error rates, namely the ones associated to the false alarm and to the missed detection, can exceed the target value. However, assuming that both the targets are much lower than one, the discrepancy should be bounded.

### 4.5.1. Tailoring for the trajectory safety problem

In the current context of evaluating whether a trajectory leads to an unsafe state, defined as the spacecraft entering a specified keep-out sphere with a radius of $R_{KoS}$ around the attractor, the problem is formulated as described below.
The two hypothesis are straightforwardly defined in terms of the distance at closest approach, analytically computed under the Two body problem assumption (as in 4.2.1). Therefore, at $t_{CA}$ or equivalently when the anomalies zero out, $H(t_{CA}) = \theta(t_{CA}) = 0\ rad$,

the hypothesis can be formulated in relation to the keep-out sphere radius $R_{KoS}$:

$$\begin{aligned} H_0 &: r_{CA} = ||\mathbf{r}(t_{CA})|| \leq R_{KoS} \\ H_1 &: r_{CA} = ||\mathbf{r}(t_{CA})|| > R_{KoS} \end{aligned} \tag{4.69}$$

As typical in inferential test, the Null hypothesis is associated to the most risky condition, that if accepted leads to increased but "sustainable" cost. In the collision assessment problem, it is therefore associated to the spacecraft being on an unsafe trajectory, entering the KoS, and is interpreted as the "pessimistic" hypothesis.
On the other hand, the alternative represents the complementary condition where the spacecraft traverses the point of closest approach without entering the unsafe state space region. Analogously, this can be seen as the "optimistic" hypothesis.
From a state space point of view, the conditions (4.69) generate a *partition* (also in Probability terms) visually resembling a sphere. This partition is equivalent to imposing an inequality constraint on the PDF of the random variable of interest. In this case, the latter is clearly the position vector of the spacecraft at the time of closest approach, thus classifying the problem in the framework of constrained state estimation.

### 4.5.2. Inequality constraint evaluation and enforcement

The Current-State filter formulation was chosen due to its adaptability to the presented workflow, especially in evaluating and enforcing constraints. In this approach, the filters in the bank process measurements as they arrive at each "current" timestep $t_k$, and the constraint is enforced after each update.
From the various methods available to ensure state constraints [5], the Sigma-Point projection is selected as it seamlessly integrates with the implementation of the Square-Root Unscented Kalman Filter. The algorithm is summarized in the following steps:

1. Generate Sigma points $\boldsymbol{\chi}_{i,k|H_j}$ of the state PDF as current time $t_k$.
2. Evaluate the constraint function $\mathbf{c}(\boldsymbol{\chi}_{i,k|H_j})$ for the $i^{th}$ sigma point. If the constraint given by $H_j$ is already satisfied at $t_{constr}$, the sigma point is added to the projection set $\mathbf{P}_{k|H_j}$ without any modification.
3. If the constraint given by the hypothesis is not satisfied a projection function $\mathbf{p}(\boldsymbol{\chi}_{i,k|H_j})$ is applied firstly to obtain the constrained sigma point on the constraint and secondly to compute its map backward to the current time.
4. The state PDF at time $t_k$ is then reconstructed from the projection set $\mathbf{P}_{k|H_j}$ and is guaranteed to satisfy the constraint.

**Cartesian coordinates constraint function** A strategy for calculating the position vector direction and the time to the closest approach is required, utilizing the state knowledge at any given time. As already pointed out, time propagation is computationally infeasible and reliance on the Keplerian dynamics assumption is necessary, irrespective of the filter's dynamical model.
The adopted method, chosen for its simplicity and robustness, involves the geometrical derivation of the required direction. Specifically, formulas from Two-body problem and orbit kinematics (4.70, 4.71, 4.72) are used to compute the orbital angular momentum direction (normal to the plane) and the True anomaly.

$$\mathbf{h} = \mathbf{r} \times \mathbf{v} \tag{4.70}$$

$$\mathbf{e} = \frac{1}{\mu}\left(\left(v^2 - \frac{\mu}{r}\right)\mathbf{r} - r(\mathbf{r}\cdot\mathbf{v})\mathbf{v}\right) \tag{4.71}$$

where recall that $\mathbf{r}\cdot\mathbf{v}$ is the radial velocity $v_r$.

$$\theta = \begin{cases} cos^{-1}\left(\dfrac{\mathbf{e}}{e}\cdot\dfrac{\mathbf{r}}{r}\right) & \text{if } v_r \geq 0 \\ -cos^{-1}\left(\dfrac{\mathbf{e}}{e}\cdot\dfrac{\mathbf{r}}{r}\right) & \text{if } v_r < 0 \end{cases} \tag{4.72}$$

Finally, Rodriguez's formula (4.73) is utilized for applying a 3D rotation of a vector around a unit direction [51]. The current position vector $\mathbf{r}(t_k)$ is rotated through the true anomaly around the normal to the orbital plane $\hat{\mathbf{h}}$. The result is normalized using the `normalize` operator and multiplied by the analytically computed pericentre radius $r_p = h^2/\mu(1+e)$.

$$\hat{\mathbf{r}}(t_{CA}) = \texttt{normalize}\left(\mathbf{r}(t_k)cos\,\theta(t_k) + \hat{\mathbf{h}}\times\mathbf{r}(t_k)sin\,\theta(t_k) + \hat{\mathbf{h}}(\mathbf{r}(t_k)\cdot\hat{\mathbf{h}})\,(1 - cos\,\theta(t_k))\right) \tag{4.73}$$

$$\mathbf{r}(t_{CA}) = r_p\,\hat{\mathbf{r}}(t_{CA})$$

The constraints (4.69) are evaluated based on $r_p$ value for both the $H_0$ and the $H_1$ filters. It is to be noted that only one of them undergoes constraining at any time due to the complementary nature of the hypotheses.

**Keplerian elements constraint function** The constraint evaluation becomes slightly easier when a keplerian state vector is used as direct evaluation is possible (4.24). The time to $CA$ is obtained from the Hyperbolic anomaly through the time law.
The computation of the position vector at $CA$ necessitates the conversion to cartesian coordinates after zeroing out the anomaly, since the chosen projection function strictly

requires it.

**Projection function and application** The problem of mapping the constrained state (sigma point) backward in time up to the current time instant $t_k$ is identifiable as a two point boundary value problem (TPBVP), and specifically a targeting problem. In fact, the position vector at $t_{CA}$ is completely defined, as well as the position vector at current time $t_k$ and the time required for the spacecraft to move from one to the other, $\Delta t_{CA} = t_{CA} - t_k$. The velocity vectors are the only degrees of freedom that need to be determined.
For a motion governed by a generic dynamical system, Differential correction technique must be employed to iteratively solve the TPBVP. However, when sigma points are of concern, solving the same problem independently for each becomes computationally challenging. A potential solution, left for future work, might involve the use of Taylor maps (i.e., Differential Algebra) to solve the Differential Correction problem only once, with the remaining points obtained through the simple evaluation of the polynomial map.
The keplerian dynamics assumption enables the use of a Lambert's problem solver [7]. Therefore, for each sigma point $\boldsymbol{\chi}_{i,k} = [\mathbf{r}_{i,k}, \mathbf{v}_{i,k}]^T$ under $H_j$ that does not satisfy the corresponding constraint, the targeted position vector $\bar{\mathbf{r}}_{i,CA}$ is initially determined by scaling up or down the magnitude of the position vector obtained from the constraint function. Specifically, it must be such that the sigma point state lies on the constraint manifold (i.e., the Keep-out sphere):

$$\bar{\mathbf{r}}_{i,CA} = R_{KoS} \frac{\mathbf{r}_{i,CA}}{||\mathbf{r}_{i,CA}||}$$

Lastly, Lambert's solver yields the constrained sigma point $\bar{\boldsymbol{\chi}}_{i,k}$ at the current $t_k$:

$$[\bar{\mathbf{v}}_{i,k},\ \bar{\mathbf{v}}_{i,CA}] = \texttt{Lambert}(\mathbf{r}_{i,k},\ \bar{\mathbf{r}}_{i,CA},\ \Delta t_{CA}) \ \Rightarrow\ \bar{\boldsymbol{\chi}}_{i,k} = \begin{bmatrix} \mathbf{r}_{i,k} \\ \bar{\mathbf{v}}_{i,k} \end{bmatrix}$$

If Keplerian elements are being used, an additional conversion step from Cartesian coordinates must be carried out. In the case where considered parameters $\mathbf{p}$ are included in the state vector, no operation is performed on them. The only difference is that the unconstrained sigma points will have additional dimensions capturing the uncertainty in those states. These must be preserved and reattached when applying the constraint. Therefore, the constrained sigma point would be defined as $\bar{\boldsymbol{\chi}}_{i,k} = [\mathbf{r}_{i,k}, \bar{\mathbf{v}}_{i,k}, \mathbf{p}_i]^T$.

### 4.5.3. Filter design considerations

During the investigation, it was noted that two commonly used features in navigation filters, namely process noise and editing, are detrimental for the test evaluation. The same is true for any kind of adaptive filtering technique, for the following reasons:

1. **Process noise** serves the purpose of artificially enlarging the covariance during the Time Update step. This is essential for proper estimation in navigation scenarios where the dynamics of the filter is greatly affected by model errors. However, in the present case, process noise accelerates the divergence of the constrained filter when measurement predictions become inconsistent. Furthermore, it may increase the chance of the test reaching an incorrect decision, by artificially making one of the two filter more "capable of explaining" the observations.

2. **Measurements editing** shall not be employed unless a third unconstrained filter is used. The test execution relies on the fact that even the filter with a trajectory farther from the actual one still incorporates measurements. The key point is that the comparison of the Innovation PDFs drives the decision. Using measurements editing would essentially mark all measurements as outliers in the constrained filter. This is why Carpenter et al. [12] emphasize the need for a third unconstrained filter for this purpose.

3. **Adaptive filters** perform on-line adjustment of measurement and process noise covariance, based on the residuals of the Observation update step. While this capability could potentially improve estimation error and filter consistency, it is incompatible with the present framework due to reasons similar to process noise. Additionally, the assumptions underlying many adaptive methods are inherently undermined by constraint enforcement.

Therefore, the filters employed to construct the bank were implemented in the simplest formulation possible. They estimate the orbital state vector only, with constant measurement noise covariance, and without the addition of process noise.

### 4.5.4. Filters measurements prediction consistency issue

The formulation presented in the current study and adapted from previous literature [12–14, 49], exhibits a significant limitation regarding the filters capability to predict measurements through the designed observation models. In the application to conjunction assessment between two objects, the filters process measurements acquired from "external sources" and estimate their relative state. The constraint is enforced on it but has little

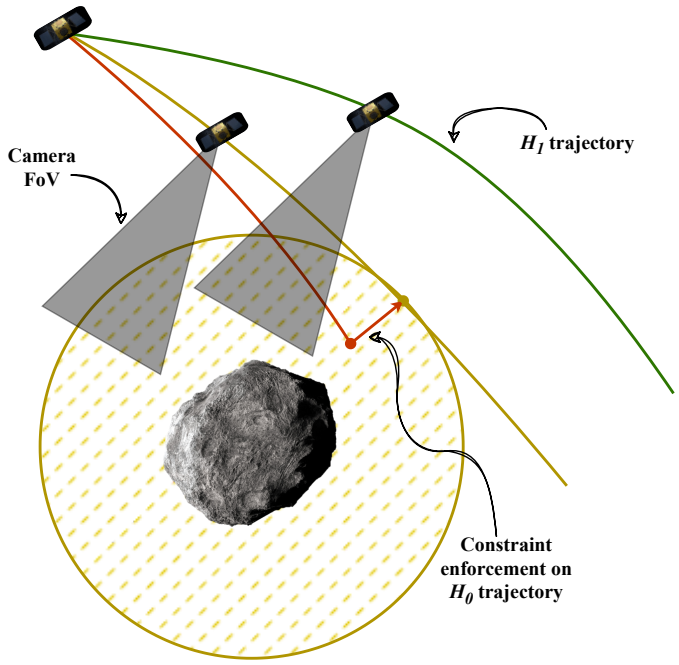


Figure 4.3: Two-dimensional representation of the spacecraft loosing the target body due to constraint enforcement in the Nominal EXP (safe).

influence on the measurements prediction. Contrarily, the on-board application have the peculiarity that the capability of the estimators to predict the measurements *fundamentally* depends upon the filter state estimate (i.e. trajectory) and the attitude knowledge. The attitude knowledge is assumed to be provided by an independent attitude estimator and must be common to both failure detection filters *and* the navigation system. The immediate consequence is that if the estimated trajectory differs too much from the real one, either of the two filter stops predicting physically consistent measurements even though sensors and IP provide a valid input.
Figure 4.3 depicts in 2D what may occur in the Hera scenario, which determines two issues:

1. The altimeter prediction results in either "no intersection" or a completely non-physical range. This is the most likely between the two, given the small size of the asteroids: even a slight change of position could cause the line-of-sight not to intersect the target body.

2. The centroid prediction results out of the image plane, i.e., the spacecraft should not be able to see the target.

In both cases, the filters have to reject the update and the sequential update of the Likelihood ratio may stop before having reached a decision or ends up being "stuck" with

the last made decision. Finally, perhaps not surprisingly, it was noted that in practice this event occurs *only* for the constrained filter of the bank, i.e., the filter whose hypothesis is the farther from the actual "truth". This was deemed to be a relevant information for the failure detection system, and was in fact exploited for the countermeasures to mitigate the mentioned issue, described in the next section.

### 4.5.5. Test execution and reset capability

Several alternatives for the implementation of the methodology were considered and traded-off from an operational point of view:

1. **Decoupled** execution: The filters bank initialization takes place at the Navigation filter start-up from ground knowledge. It works completely independently from the GNC. Reset of both the Ratio test and the filters state is applied at maneuvering time, using a nominal trajectory uplinked by Ground.

2. **Partially coupled** execution: similar to the decoupled case, the filters bank initialization occurs at Navigation start-up. Reset and re-initialization at maneuvering point rely on the last available navigation solution.

3. **Coupled** execution: the only difference compared to the partially coupled is in the frequency and in the condition of the resets, which are not limited to maneuvering points. At each reset, the constrained bank retrieves the navigation solution and resumes testing.

To appreciate the necessity of the reset at the maneuvering points, it is essential to consider that the commanded $\Delta v$ for a maneuver is always based on a nominal or estimated trajectory (for Flight-dynamics planning or on-board corrections, respectively). Consequently, applying a constrained trajectory significantly deviating from the nominal trajectory leads to rapid divergence of the filter. This divergence can rapidly result in a covariance that becomes non-positive definite, as was observed in this study.
Among the three alternatives, only the last two were deemed sufficiently interesting for two reasons:

- The correction provided by the guidance is based on the estimated state; the latter could potentially be sufficiently different from the nominal trajectory computed off-line to make both the filters in the bank not accepting measurements after the re-initialization.

- The presented framework of hypothesis testing seems more suitable as a mechanism to continuously check the current navigation solution only considering batches of

measurements, rather than all the measurements prior to reset.

Therefore, chapter 5 was focused on the coupled configuration in that the partially-coupled can be intended as a particular case of the former.

**Reset condition** The test reset is commanded based on a decision counter threshold. Specifically, each time the Likelihood ratio is compared against the boundaries, a counter is either increased by one or re-initialized to zero if the outcome of the comparison in 4.68 changes at one step. The threshold is intended as tunable parameter linked to the designed measurement update frequency. The decision is effectively considered as "reached" only after the threshold is exceeded.

**Secondary decision mode** A secondary, simpler detection method is activated when either of the constrained filters ceases to execute a measurement update. This situation becomes more frequent as the spacecraft approaches the asteroids, with the trajectory playing an increasingly crucial role in determining whether the bodies are within the altimeter beam and camera view.
Upon the skipping of a Likelihood ratio, a second counter is initiated and consecutively incremented at each timestep if the event consistently originates from the same filter. A tunable threshold on the elapsed time is defined and a decision is inferred based on which of the two filters, hence hypothesis, is failing.

### 4.5.6. Constraint enforcement verification

The verification of the constraint enforcement algorithm involved checking the constraint value of the reconstructed state after the enforcement, specifically for the Cartesian state filter in the coupled configuration. Twenty simulations were conducted in both the nominal and unsafe scenarios, using HFM measurements and random initialization conditions for the filters bank.
In the first scenario, represented in fig. 4.4, $H_1$ state do not require the constraint application as a consequence of the trajectory being safe; conversely, the $H_0$ state is constrained to remain below the $R_{KoS}$ radius at all times. On the other hand in the second scenario, in fig. 4.5, the trajectory becomes unsafe after the $1^{st}$ manoeuvre. Therefore, it is expected that $H_1$ state starts to be constrained after this event, as soon as the violation of the hypothesis is detected. As desired, the constraints enforced by the hypothesis are reflected by the constrained mean state at any time, proving that the strategy is effective.

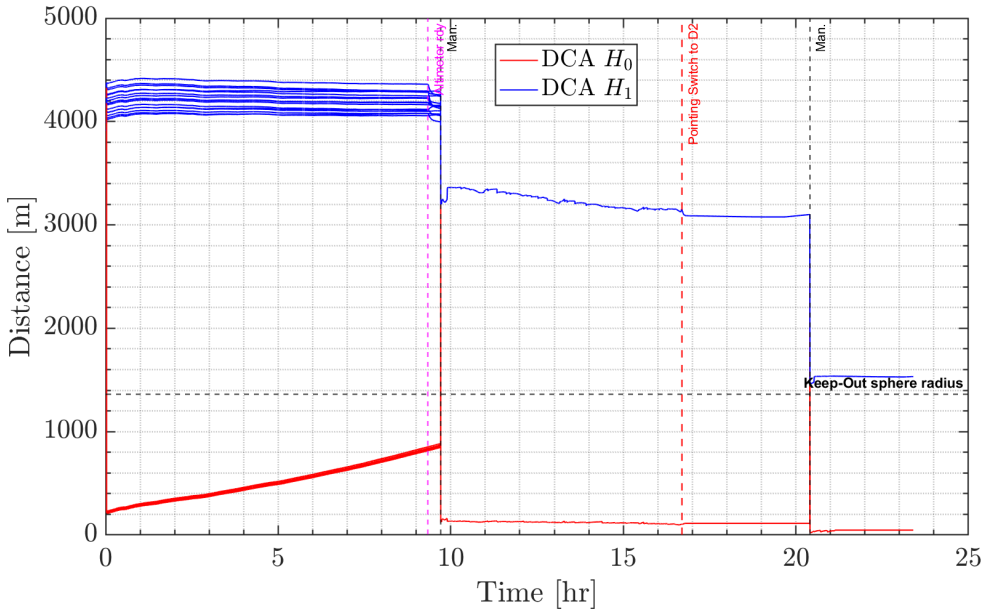


Figure 4.4: Constraint evaluation after enforcement during Nominal EXP.

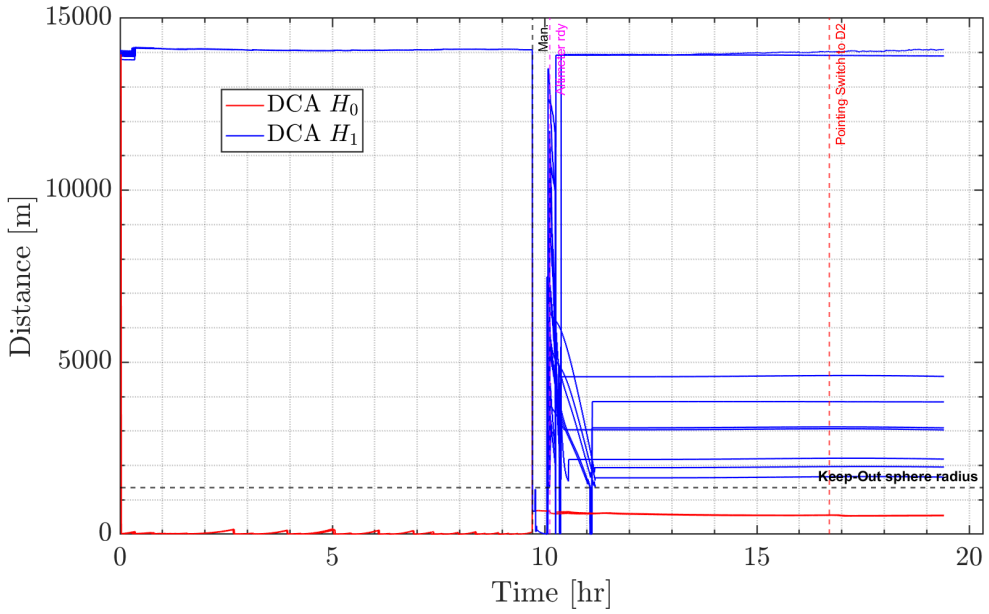


Figure 4.5: Constraint evaluation after enforcement during Unsafe EXP.

# 5 | Results, analysis and discussion

This chapter presents the results of the analysis of the algorithms to evaluate their accuracy and reliability. Two scenarios were used depending on the analysis:

1. **Nominal** EXP trajectory. The reference trajectory does not pose any risk. The expected output is therefore, that no alarm is triggered.
2. **Unsafe** EXP trajectory. Since it was not possible to obtain such a trajectory by chance in MC simulations, the semi-autonomous guidance was intentionally forced to target an unsafe position during the $1^{st}$ manoeuvre.

**Unsafe EXP trajectory details** The unsafe trajectory is depicted in figure 5.1. The second manoeuvre is reported as well, but it is not of interest for the analysis. The arc after the first manoeuvre evidently results in a risky closest approach, while also being very steep toward the asteroids. The measurements available during the trajectory are

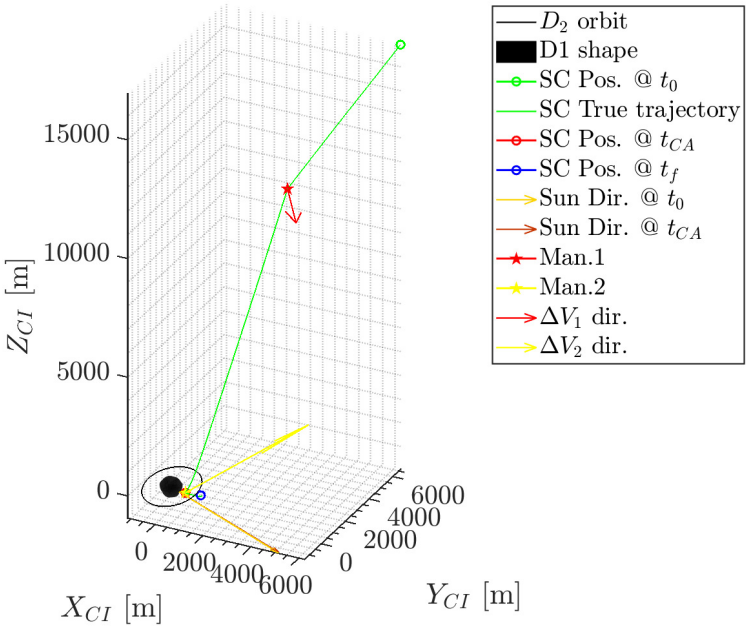


Figure 5.1: Unsafe EXP trajectory, D1 and D2 at $t_{CA}$ @Didymos CI.

reported in fig. 5.2. It is important to notice that the centre of brightness measurements on Dimorphos are not recovered after the outage, in contrast to the nominal trajectory (3.12). Due to the trajectory, the availability of the altimeter is expected to play a relevant role in allowing a sufficiently accurate range estimation as will be shown in section 5.2.

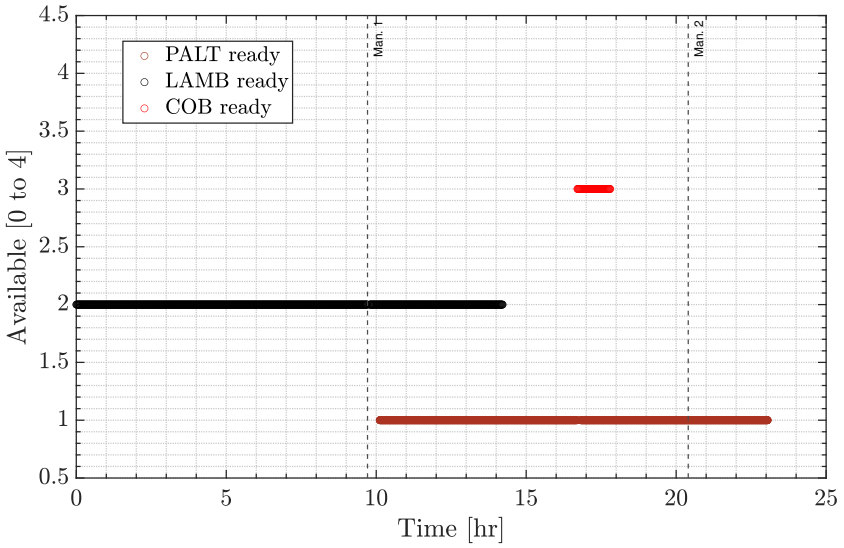


Figure 5.2: Observables availability windows during unsafe EXP trajectory.

## 5.1. Performance of Measurements-Only CRE

**Tuning parameters** The algorithm has several tuning parameters which significantly influence the results. The default values maintained throughout the analysis are now explained.

- $N_{d,r}$, $N_{d,\theta}$: the degrees of the polynomial fitting were chosen based on simulations, evaluating the "shapes" of the signals and the "stability" of the fitting. Default values: $N_{d,r} = 1$, $N_{d,\theta} = 3$.
- $N_\theta$: the number of samples for the displacement was set considering a trade-off between the noise reduction capability and bias introduced by the smoother, in addition to the time corresponding to the window: 1 *hour* of acquired measurements. Default value $N_\theta = 75$.
- $N_r$: the number of samples for the range measurements is in principle independent. For simplicity, it was selected from $N_\theta$ to have a frequency of 1 $Hz$. Default value $N_r = 3600$. Note that this is the most relevant parameter in determining the computational time.

### 5.1.1. Performance using ideal measurements

A preliminary evaluation was performed in the nominal scenario to assess the validity and correct implementation of the algorithm. The LFM was used to simulate the measurements without any error source other than the assumptions required by the method (including the spherical shape of the target body). Simultaneously, this also provided information about its limitations in terms of applicability.

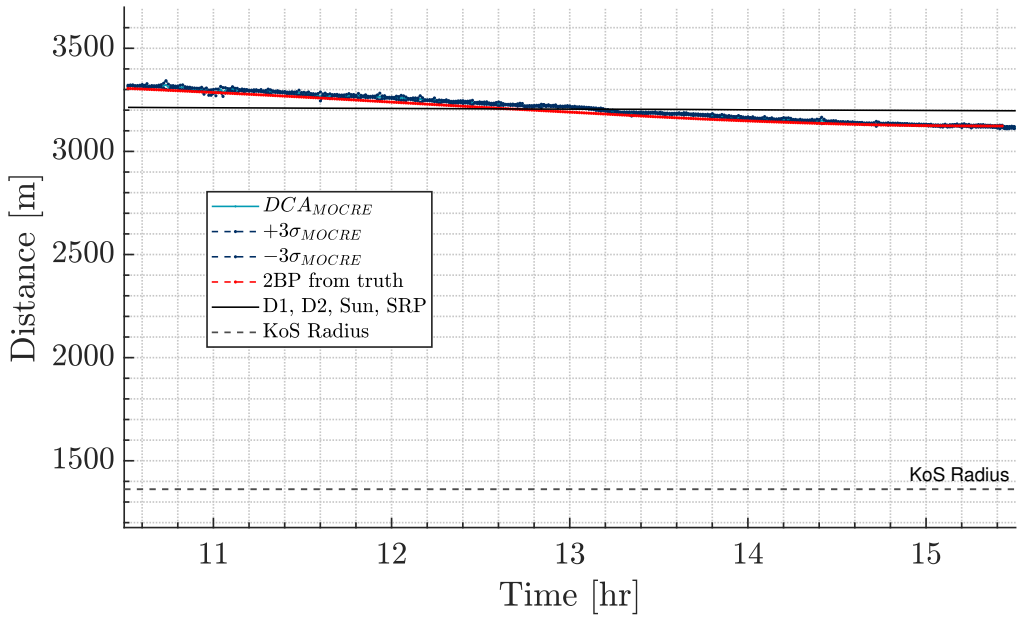


Figure 5.3: MOCRE closest approach distance evaluation with ideal measurements - Nominal EXP (Default tuning).

Figure 5.3 shows the results of a single run, presenting both the reference closest approach distance "$DCA_{HF}$" calculated through propagation ($3^{rd}$ dynamical model presented in chapter 3) and closest approach distance derived from the reference trajectory through the 2BP assumption "$DCA_{KEP}$". The variance bound is visibly zero, as no noise is considered in this idealized scenario.

Table 5.1: Statistics of MOCRE DCA estimation error wrt $DCA_{KEP}$ - Nominal EXP.

| Metric | Mean | Median | Std. Dev. | Max |
|---|---|---|---|---|
| Absolute [m] | 14.6 | 16.2 | 6.80 | 27.5 |
| Relative % | 0.45 | 0.50 | 0.21 | 0.86 |

Absolute and relative errors, as defined in eq. (3.6), were computed for two cases: 1) the algorithm prediction with respect to the $DCA_{KEP}$ and 2) the $DCA_{KEP}$ with respect

Table 5.2: Statistics of $DCA_{KEP}$ estimation error wrt $DCA_{HF}$ - Nominal EXP.

| Metric | Mean | Median | Std. Dev. | Max |
|---|---|---|---|---|
| Absolute [m] | 48.7 | 53.1 | 24.9 | 91.7 |
| Relative % | 1.52 | 1.66 | 0.78 | 2.85 |

to $DCA_{HF}$. Table 5.1 and 5.2 report the statistics of the two errors, respectively. The objective was to evaluate the contribution of the Keplerian dynamics assumption in determining the prediction error. Although the maximum value of the error due to the latter contribution may not be negligible during a closest approach of few hundreds of meters, it is deemed small enough to be managed by adding a margin to the keep-out sphere radius. Under ideal conditions, the method exhibits minimal error, primarily associated with the assumptions made and, secondarily, with the finite-size window of the estimation. Indeed, it would converge to the red curve in 5.3 if all the measurements samples were fitted to obtain the regression polynomial. As final note, figure 5.3 already indicates that the output probability of collision is consistently zero throughout the entire estimation: the $3\sigma$ boundary is significantly distant from the keep-out sphere radius.

### 5.1.2. Performance using measurements adding white noise

A second analysis was performed to assess the effect of artificially noisy measurements serving as a bridge between the ideal case performance and the results obtained from the HFM simulation. White noise only was added to the altimeter measurement ($\sigma_{Alt} = 25$ m) and the centroid measurement ($\sigma_{Cen} = 10$ pix).

**Nominal case** Figure 5.4 illustrates the estimation performance in the Nominal case, demonstrating the smoother's capability to predict the DCA on average. However, it also confirms that the method quickly becomes unreliable as the noise level increases. Moreover, the variance approximation from the fitting residuals appears to be a major limitation as it determines a large uncertainty bound the estimator cannot reduce. Consequently, the PoC computation is highly influenced by the size of the latter, potentially leading to numerous false alarms.

Nevertheless, fig. 5.5 shows that the algorithm still performs adequately because this issue arises in scenarios where the actual minimum distance is very close to the KoS radius.

**Unsafe case** Similarly to the previous case, the estimator is able to detect the safety issue as the computed probability is in practice equal to 1. The noise reduction capability remains unchanged with the estimation error oscillating within an interval of approxi-

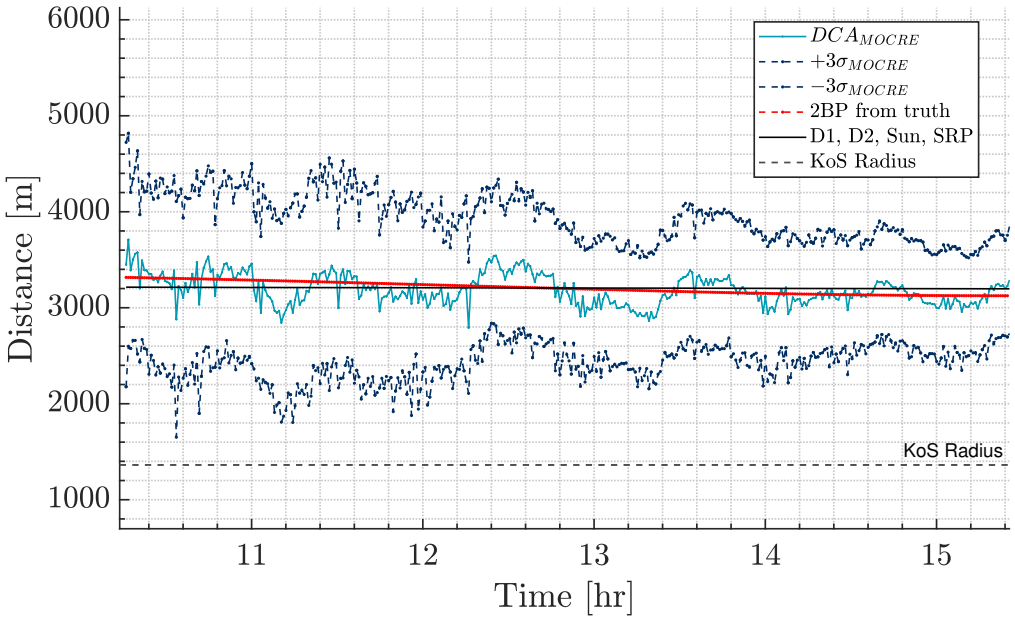


Figure 5.4: MOCRE closest approach distance evaluation with noisy measurements - Nominal EXP (Default tuning).

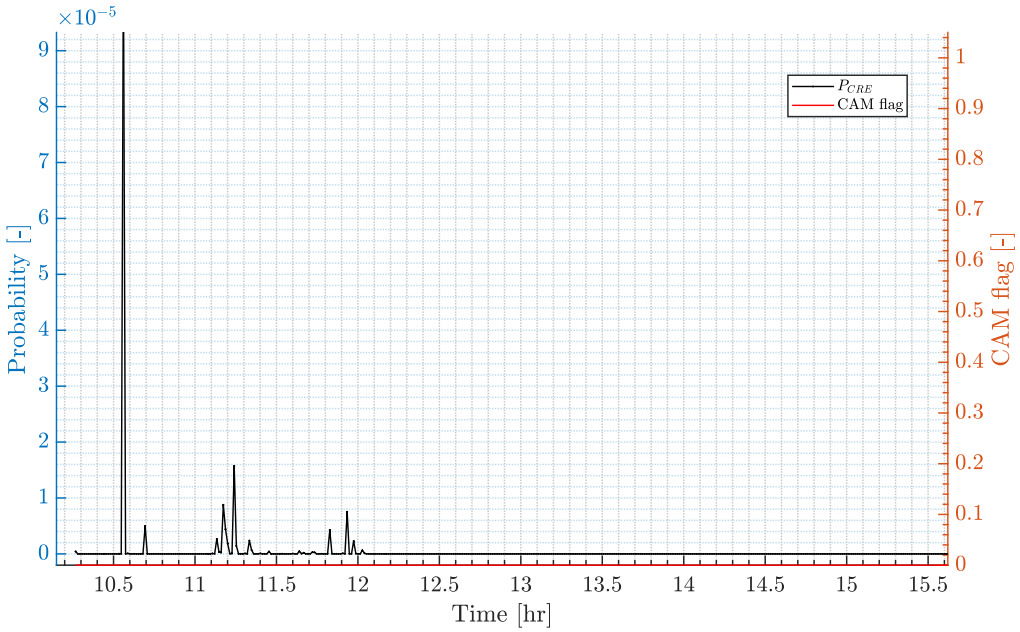


Figure 5.5: PoC and CAM flag from MOCRE output with noisy measurements - Nominal EXP (Default tuning).

mately 500 meters.

Furthermore fig. 5.6 also indicates that the estimated PDF of the signal does not ac-

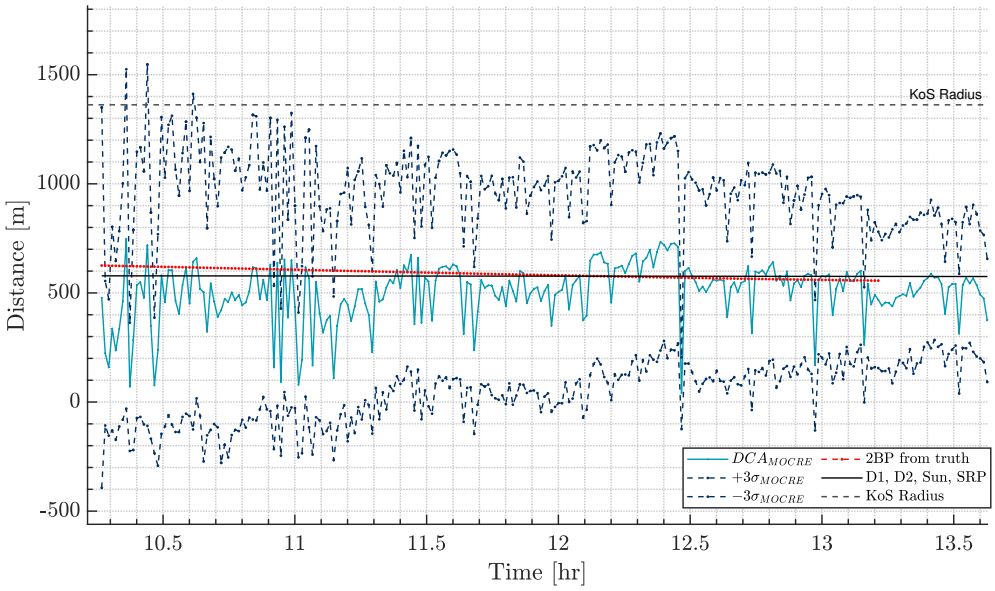


Figure 5.6: MOCRE closest approach distance evaluation with noisy measurements - Unsafe EXP (Default tuning).

count for the physical constraint of the minimum distance being greater than 0, as the uncertainty bound covers negative values.

### 5.1.3. Performance using HFM observables

**Nominal case** The HFM measurements were finally used to test the method in a mission-relevant case. Figure 5.7 reports the nominal case results, which reveals a noticeable degradation of performance compared to fig. 5.4. The effects of the additional error sources (i.e., misalignments, correlated noise) significantly invalidate the LS assumptions, leading to an inconsistency in the estimates. Unlike the previous cases, the error bounds no longer encompass the reference value due to the substantial estimation error.

Similarly, figure 5.9 highlights the impact on the probability computation, where the threshold-based decision mechanism fails, resulting in multiple false alarms. The primary contributor to the estimation error was identified as the centroiding measurements. Notably, a correlation was observed between the motion of the centroid (i.e., line-of-sight) in the image plane and the significant oscillations in the nominal estimate. This correlation could be attributed to a combination of pointing errors, variations in the target body's attitude, and the execution of the image processing algorithm. A visual inspection of the time evolution of the samples of the line-of-sight displacement $\theta$ compared with the same quantity computed from the position vector in figure 5.8 confirms the hypothesis. The

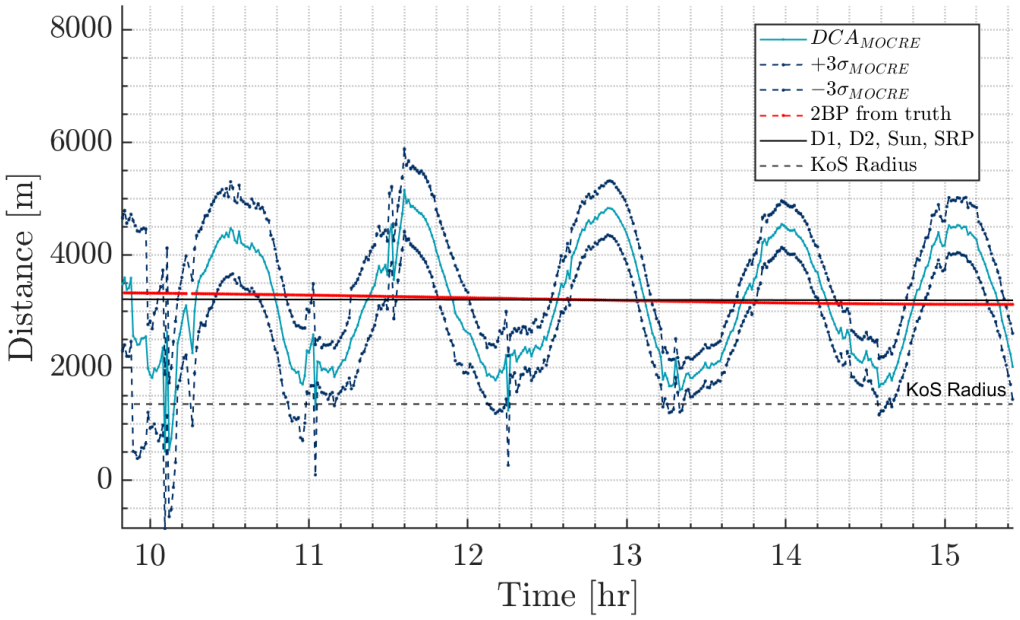


Figure 5.7: MOCRE closest approach distance evaluation with HFM measurements - Nominal EXP (Default tuning).

variations in the samples used for estimation and the estimation error exhibit the same periodicity. Additionally, this is consistent with the observation that a larger window helps in mitigating this issue, as discussed later in section 5.1.3.

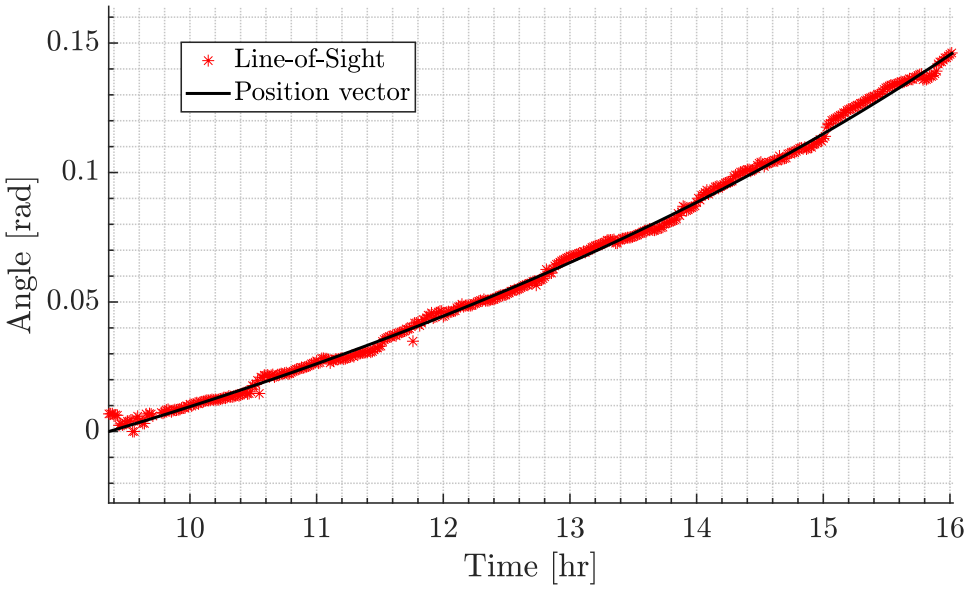


Figure 5.8: Samples of displacement $\theta$ computed from position vector and line-of-sight - Nominal EXP.

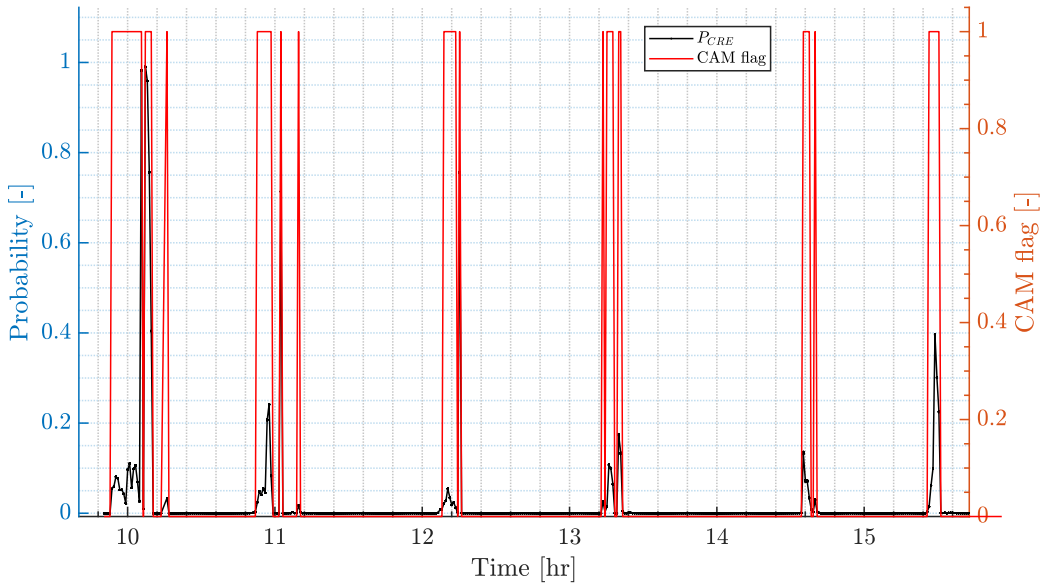


Figure 5.9: PoC and CAM flag from MOCRE output with HFM measurements - Nominal EXP (Default tuning).

**Unsafe case** The unsafe case results are reported in the appendix, figures A.1 and A.2, as they only confirm the previous analysis without adding particularly relevant information. Table 5.3 presents a comparison of the total estimation error obtained in the

Table 5.3: Statistics of DCA total estimation error in Nominal and Unsafe cases.

| Case | Mean | Median | Std. Dev. | Max |
|---|---|---|---|---|
| Nom. absolute [m] | 906.6 | 957.3 | 464.4 | 2701 |
| Unsafe absolute [m] | 600.5 | 533.0 | 432.5 | 1327 |
| Nom. relative [%] | 28.9 | 29.8 | 14.5 | 84.0 |
| Unsafe relative [%] | 104 | 92.4 | 75.3 | 231 |

Nominal and Unsafe cases, indicating a complete failure of the method to deliver a reliable and accurate estimate. Notably, the relative error reveals that as Hera gets closer the absolute error does not decrease proportionally, leading to an excessive growth in the relative values. It is important to note that the lower absolute error statistics in the Unsafe case can be attributed to the bounded nature of the estimated quantity, rather than an actual improvement in the estimation accuracy.

**Nominal case: Increased Window** The previous paragraphs illustrated that the method does not yield a sufficiently smoothed solution for reliable assessments with the default tuning. A final analysis was performed by increasing the window length to $N_\theta = 150$

(i.e., effectively doubling the time window to cover $2\,hr$). Figure 5.10 shows a reduction in the nominal value of the estimation error, eliminating all the false alarms.
However, as expected, the uncertainty bound does not shrink since it is entirely dependent on measurement precision (i.e., measurement noise covariance), which is directly propagated to the estimate with limited filtering capability. Table 5.4 presents the statistics

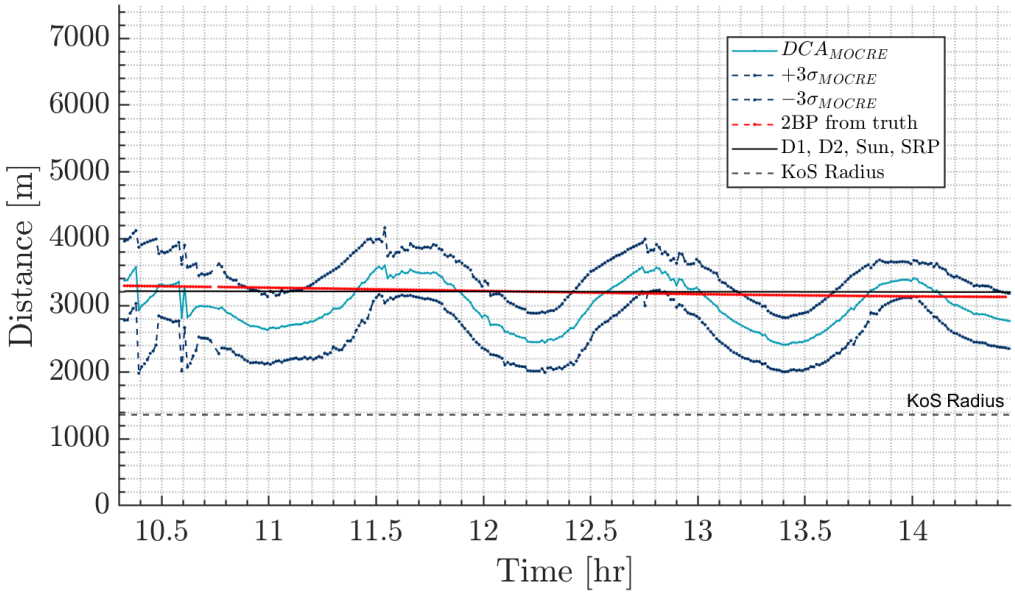


Figure 5.10: MOCRE closest approach distance evaluation with HFM measurements - Nominal EXP (Extended window).

Table 5.4: Total relative % error statistics of MOCRE default vs extended window - Nominal EXP.

| $N_\theta$ | Mean | Median | Std. Dev. | Max |
|---|---|---|---|---|
| 75 | 28.3 | 29.8 | 14.5 | 84.0 |
| 150 | 8.97 | 8.70 | 5.16 | 19.1 |

of the relative error in percentage between the default window size and the extended size, clearly indicating a significant improvement in the estimation capability. However, extending the sliding window also comes with several drawbacks:

1. The buffer size, thus the amount of memory dedicated to temporarily store the measurements, must be increased accordingly.

2. The computation time scales up. As qualitative *relative* figure of merit, the default tuning requires $6.6\,ms$ per cycle while the extended window size results in an increase to $11.68\,ms$ per cycle.

3. The estimate may become biased. In fact, this effect is visually noticeable when comparing figure 5.10 against figure 5.7.

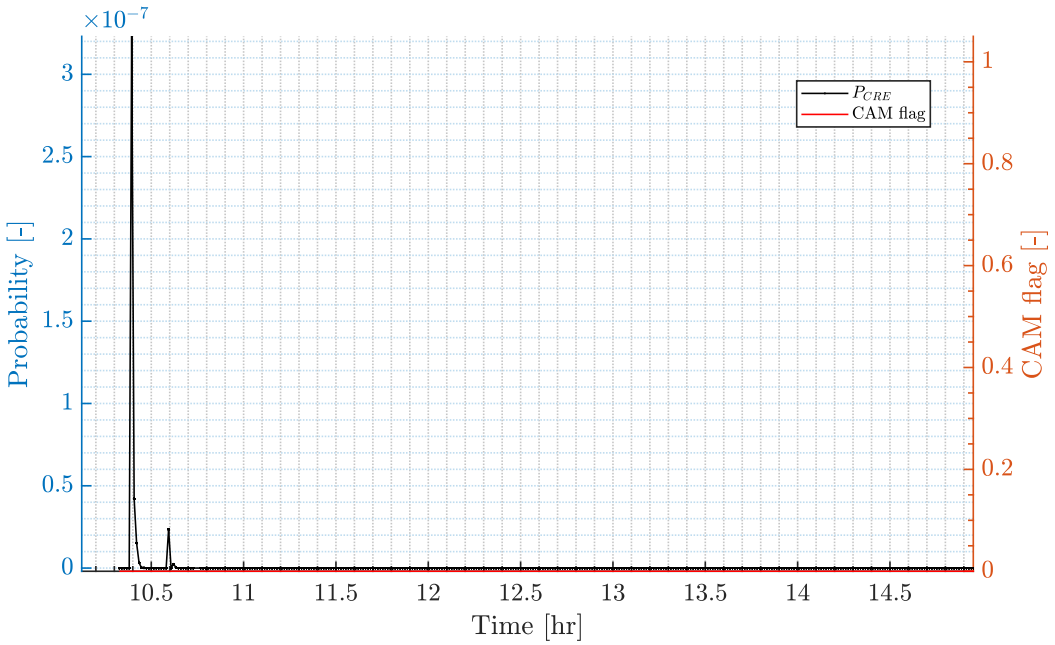


Figure 5.11: PoC and CAM flag from MOCRE output with HFM measurements - Nominal EXP (Increased window).

**Discussion** Several important considerations can be drawn:

1. The algorithm consistently produces results in line with the Keplerian dynamics assumption for evaluating the DCA. The limited-bandwidth smoother (sliding window) and the approximations of the line-of-sight and of the shape model alone do not hinder the capability to perform a correct assessment.

2. The Keplerian dynamics assumption is the primary contributor to the prediction error when the measurement noise is very low. This sets a lower bound on the achievable accuracy, which depends upon the magnitude of the accelerations along the trajectory linking the current state to the closest approach point. The accuracy improves when the Two-Body Problem (TBP) better describes the motion. Additionally, the drift in the error caused by the SRP inevitably increases with the propagation time.

3. The algorithm can be effective provided that the smoother is able to reduce the measurement noise and that the KoS radius is not within the error boundary determined by the Keplerian dynamics assumption.

4. The noise reduction capability and the variance estimation play relevant roles: the presented implementation does not manage to provide a fine accuracy and could easily trigger false alarms in case the simple threshold-based decision is applied. On the other hand, it correctly identifies collision cases based on measurements alone.
5. The increase in the number of samples is the main tuning parameter as its increase leads to a strong improvement in the noise reduction capability.
6. All the sensors must acquire measurements for the method to work; that is the translational navigation filter must ensure a sufficient pointing accuracy. This implies that the conditions under which the algorithm operates are the same as those ensuring the performance of the navigation filter.
7. The pointing must target the main attractor. While the method could be extended through geometrical considerations involving the position of the secondary, this would only add to the sources of error.

## 5.2. Parallel filter approach performance

**Analysis setup** The performance, consistency and DCA prediction accuracy of the delayed filters were evaluated for both scenarios through multiple MC analysis with different state initialization. Specifically, three variants of the motion model were compared:

1. The Keplerian elements state filter (KEP).
2. The Cartesian coordinates filter with Two-body motion model (Cartesian KEP).
3. The Cartesian coordinates filter with the more accurate motion model including gravitational perturbations of D1, D2 and the Sun and the SRP effects (Cartesian HF).

The initial state vectors were randomly generated from a Gaussian distributions with covariance matrix simulating the output of the ground orbit determination process:

$$P_{\mathbf{x}}(t_0) = \texttt{diag}\left(\begin{bmatrix} 39 \\ 101 \\ 119 \\ 1.00 \times 10^{-3} \\ 1.25 \times 10^{-3} \\ 1.40 \times 10^{-3} \end{bmatrix}^2\right) \; [m^2,\, m^2/s^2]$$

The sample size was set to 100 cases, deemed sufficient to characterize the ensemble be-

haviour. Random number generator seeds were fixed such that the influence of random errors in the comparison is minimal. It is important to note that the processed measurement time series were not changed from run to run, as they are decoupled from the estimation process.

### 5.2.1. Nominal case - HFM

#### Filter Consistency evaluation

The consistency of a filter is defined as its ability to maintan a correct representation of the state error covariance, ensuring that the estimation error stays within the $3\sigma$ bounds at all times. An initial visual assessment of the filter consistency involves plotting the estimation error of the $i^{th}$ component of the estimated state against the $3\sigma$ value derived from the square root of the $i^{th}$ entry of the covariance matrix diagonal. For evaluating vision-based navigation systems, the Camera frame is preferred over the Inertial frame, as it provides a clearer insight into the estimation process.
Figures 5.12, 5.13 and 5.14 illustrate the position estimation errors per axis over time in the camera frame for the nominal EXP. Here, Z corresponds to the boresight, nominally pointing toward the target body. In all the presented figures, vertical dashed lines indicate

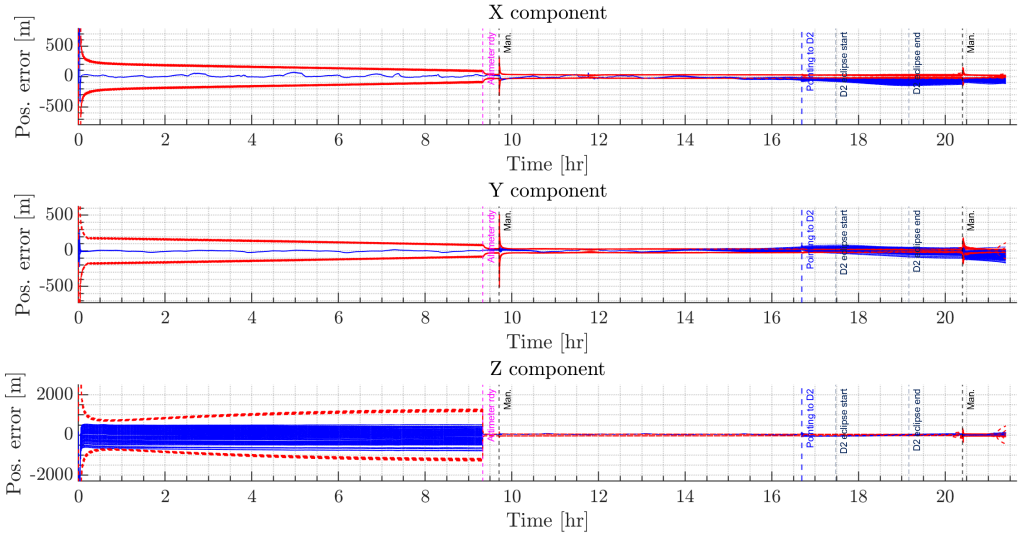


Figure 5.12: KEP: Position Estimation errors (blue solid) and $3\sigma$ covariance bounds (red dashed) - Nominal EXP @CAM frame.

the major events during the navigation window, namely:

- The manoeuvres, in black;
- The first altimeter measurement, in magenta;
- The switch of the pointing to Dimorphos and change of IP, in blue;
- The start and the end of eclipse of Dimorphos due to Didymos, in dark blue (if any).

In the nominal scenario, the eclipse determines a centroid measurement outage between $T = 17.48\ hr$ and $T = 19.16\ hr$.

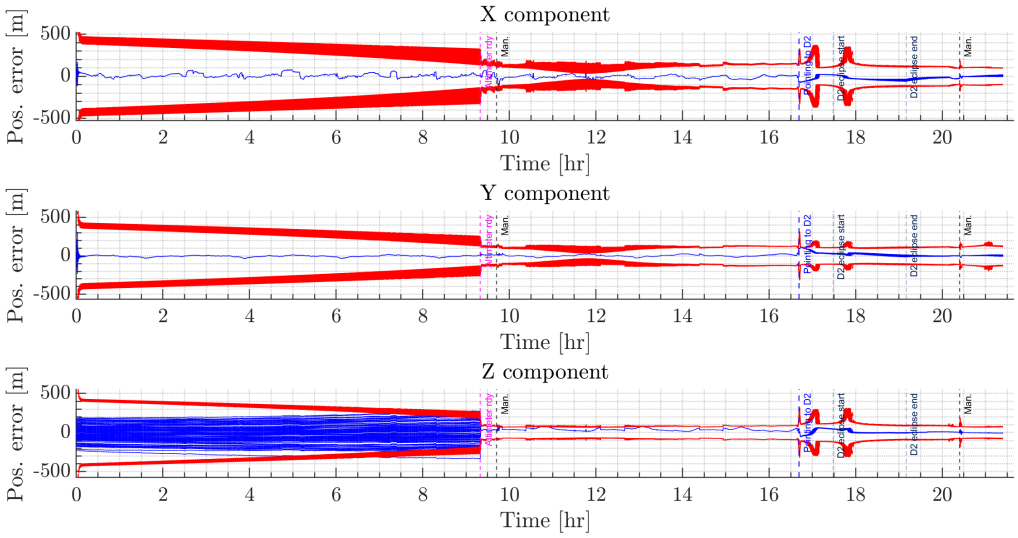


Figure 5.13: Cartesian KEP: Position Estimation errors (blue solid) and $3\sigma$ covariance bounds (red dashed) - Nominal EXP @CAM frame.

In all cases, the error along the Z boresight reveals the lower observability of the distance when only the centroid is available, followed by a rapid decrease in error when the altimeter measurement is incorporated into the estimation process. In fact, the flown trajectory lacks significant changes in parallax, a necessary condition for observing range with monocular cameras. Simultaneously, the state error covariance evolution emphasizes the difference in measurement noise covariance between the two observables, with the altimeter providing a more precise measurement.

The visual inspection of the estimation error already indicates the presence of an estimation bias in all cases, and that the filters are unable to converge to the "true" trajectory. Despite being undesirable for navigation purposes, this feature is expected "by design", as only State Noise compensation is applied to strike a balance between accuracy and

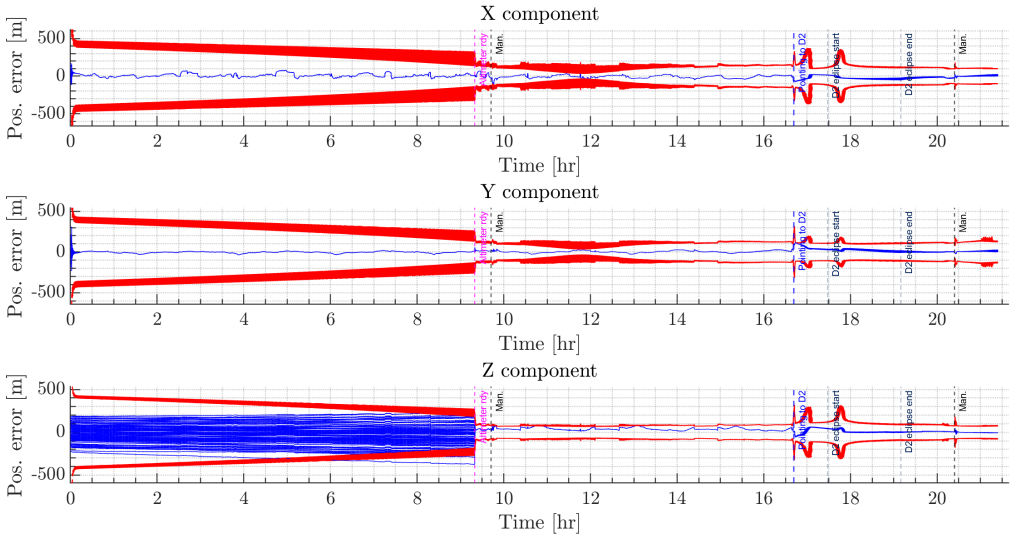


Figure 5.14: Cartesian HF: Position Estimation errors (blue solid) and $3\sigma$ covariance bounds (red dashed) - Nominal EXP @CAM frame.

computational cost. In other words, the design attempts to "cover" error sources through covariance inflation rather than estimating their states.
The objective was partially achieved in all cases, as the position estimation error remains bounded for most of the trajectory, with some caveats:

1. The Keplerian state filter begins to fail as the spacecraft approaches the system, due to the covariance reaching excessively low values.

2. Changing the process noise tuning is crucial in maintaining a sufficiently large covariance bound after the altimeter activation in the Cartesian state filters.

3. In the Cartesian filters, the boresight range starts to lose consistency slightly before the altimeter activation, due to the covariance shrink and the estimation error not being corrected. This effect is absent in the Keplerian state filter due to the process noise and the different way measurements enter the state estimation (see discussion below). It's worth noting that computing the position error in the latter case involves a non-linear transformation in addition to the rotation from CI to CAM frames.

4. The large process noise affects the smoothness of the estimated trajectory, causing worse (but expected) filtering capability. This effect is particularly noticeable after altimeter activation.

Finally, it is interesting to note that there is little difference in the evolution of the estimation error and of the covariance between the Cart. KEP and HF filters, despite the

former accumulating position error more quickly during the measurement outage. Two reasons contribute to this result:

1. The measurements frequency is high enough to correct the larger error accumulation during the Time Update.
2. The SNC masks the modeling errors of the first motion model, essentially hindering the more accurate motion model from yielding better estimation results.

### Limitations of filtering in Keplerian elements

The present analysis also revealed one of the major differences between keplerian elements and cartesian coordinates. Intuitively, the "information" the filter can extract from the observables is significantly different in the two cases, regardless of the fact that the dynamics underlying the motion is the same. Notably, none of the Keplerian elements is directly observable and at the same time, little correlation between the states builds up. This characteristic is easily understandable by considering that the State Transition Matrix of the system has zero off-diagonal entries, except for those corresponding to the anomaly. From this standpoint, figures 5.12 and 5.13 provide a first evidence that:

1. The choice of the state space parametization significantly influences whether and how the estimator corrects the initialization error.
2. The keplerian state filter loses the tracking of the trajectory during the last part of the navigation. Significantly this occurs in the X-Y axis of the camera, despite them being directly observed.

Furthermore, the non-linear transformations required in the conversions between Keplerian and Cartesian coordinates pose challenges for the feasibility of the Keplerian filter. These include accumulation of errors and increased computational burden. The measurement update of the keplerian filter in fact nullifies the advantage of the analytical propagation when a small propagation time is used (1 second in this implementation). It is to be stressed that the differences in performance are also related to different tuning, with process noise in the Keplerian state filter proving particularly difficult to set.

In conclusion, the state trajectories of the keplerian elements, which determine the position of the spacecraft in the orbital plane, are depicted in fig. 5.15 with a colormap highlighting the minimal corrections provided by the observations. This is evident by observing their time evolution from the initialization value.

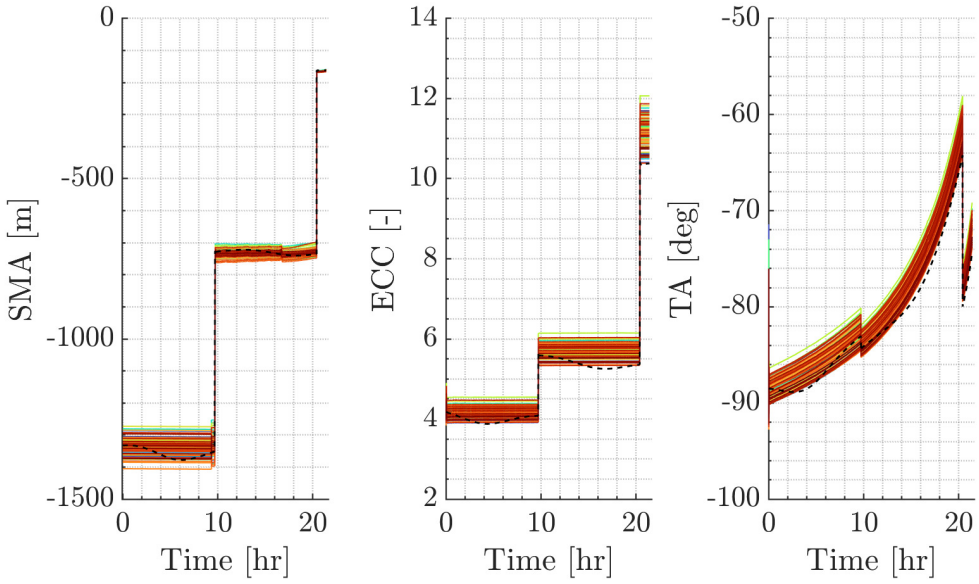


Figure 5.15: KEP: Semi-major axis, Eccentricity and True anomaly trajectories compared to "truth" Osculating Kepl. Elements - Nominal EXP @Didymos CI.

## DCA prediction performance

**DCA prediction** The DCA prediction module initiates its operation only after the initial convergence of the covariance, minimizing the risk of triggering the CAM flag due to excessively large uncertainty. Depending on the magnitude of dispersion introduced by a manoeuvre, the prediction module might be temporarily disabled soon after for a specified amount of time.
The prediction of the distance at closest approach from each "current" state is displayed for the three filter as designed in 4 in figures 5.16, 5.17 and 5.18, respectively. The first figure notably confirms again the previous considerations: the Keplerian state filter struggles to correct the initial error and continues to predict a DCA, primarily influenced by the initial state and the $\Delta\mathbf{v}$ of the manoeuvres.

Contrarily, the DCA predictions from both Cartesian state filters gradually converge towards the true value in all the initialization error samples. However, a significant issue is immediately evident, as explained next.

Despite the convergence, figures 5.17 and 5.18 highlight a significant issue with the design. The inclusion of the gravitational parameter as a considered state leads to excessively large covariance bounds of the velocity states. This in turn, causes the Unscented Transform to capture non-linear effects and fail, as evidenced by 1) the magnitude of the DCA prediction for the Cartesian state filters and 2) the negative values of the prediction, which

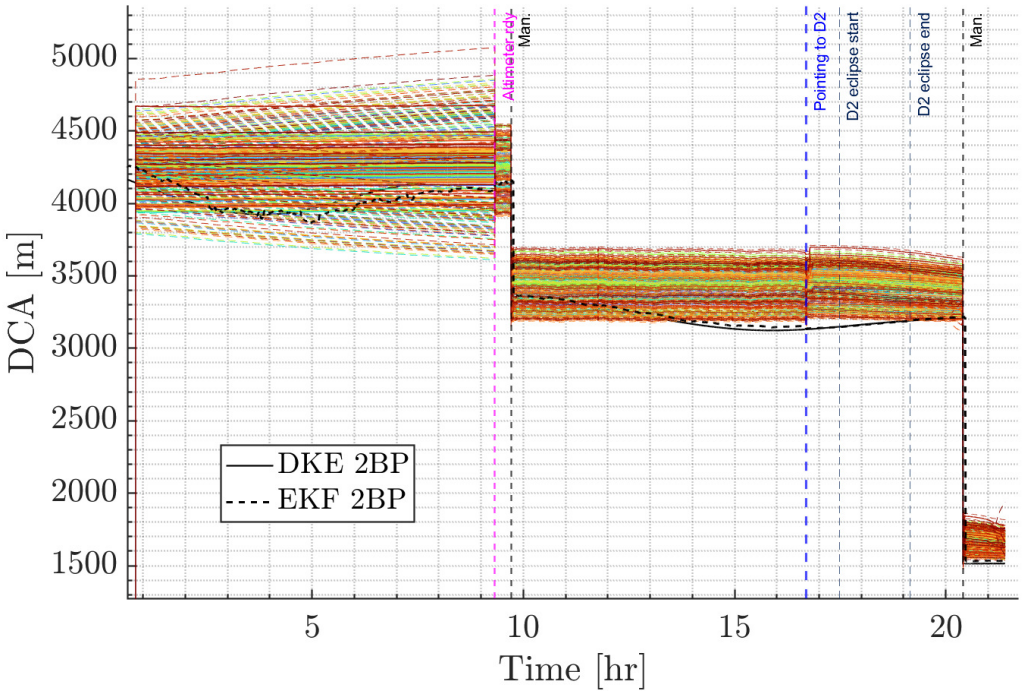


Figure 5.16: KEP: prediction of distance at closest approach with $3\sigma$ bound (dashed lines) compared against Hera EKF prediction and projection from "truth" - Nominal EXP.

have no physical meaning.
The reason was identified in the velocity covariance bounds, whose value reaches the order of km/s shortly after the filter start-up. The velocity error for the Cartesian HF filter is presented here (fig. 5.19) to illustrate the effect (see Appendix A.2 for the other cases). From a theoretical perspective, this is deemed consistent with the fact that the uncertainty in the gravitational parameter directly affects the velocity components, while state correlation determines the transfer of information to the position components. The computation of the PoC and corresponding CAM flag is not reported, as it is already evident that the PoC always exceeds the threshold.

Simulation results of the DCA prediction error and covariance bounds with the exclusion of the gravitational parameter and re-tuning of the process noise covariance, are presented in 5.20 and 5.21 for the Cartesian state filters. Except for the specified changes, no other modifications were applied compared to the previous cases. The adjustments have minimal impact on the position estimation errors, as demonstrated, while the plots for the velocity components are available in appendix A.2. This further supports the earlier observations: the estimation error in position exhibits little variation, whereas the covariance

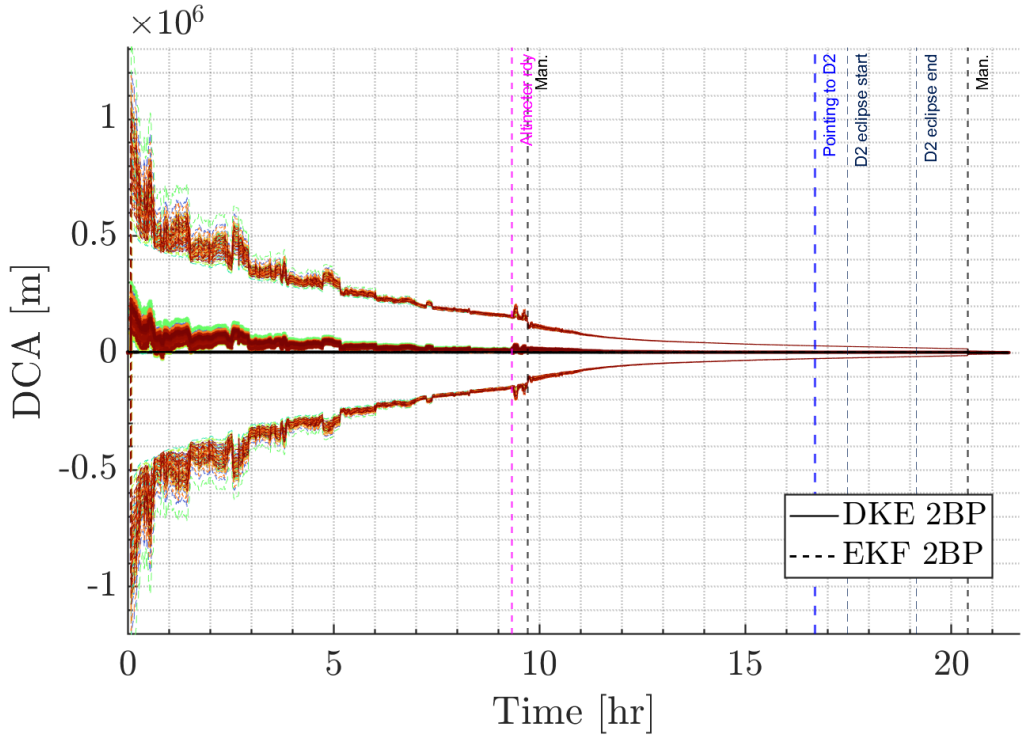


Figure 5.17: Cartesian KEP: prediction of distance at closest approach with $3\sigma$ bound (dashed lines) compared against Hera EKF prediction and projection from "truth" - Nominal EXP.

bounds undergo significant alterations. Additionally, the results reveal that the filter does not manage to reduce uncertainty in the velocity components. The corresponding computation of the PoC for the two cases is illustrated in 5.22, emphasizing that, correctly, no false alarm is triggered for the first two arcs. However, the persistently large covariance relative to the new DCA after the second manoeuvre causes the algorithm to surpass the decision threshold. Evidently, a conflict exists between the permissible process noise for consistent estimation and the necessity of avoiding false alarms.

In this regard, the HF filter counter-intuitively performs worse. Although the nominal trajectory is more accurate, the covariance does not shrink rapidly enough, leading to the probability threshold being exceeded for a longer duration. The implication is that the filters would be unable to prevent false alarms in the initial hours of navigation due to the persistent large covariance. This, however, is necessary to maintain the filter's consistency in estimating the range along the camera bore-sight.

Table 5.5 reports the absolute and relative median and standard deviation of the DCA prediction errors, computed through ensemble and time averaging for the three arcs characterized by a different DCA, separated by the manoeuvres:

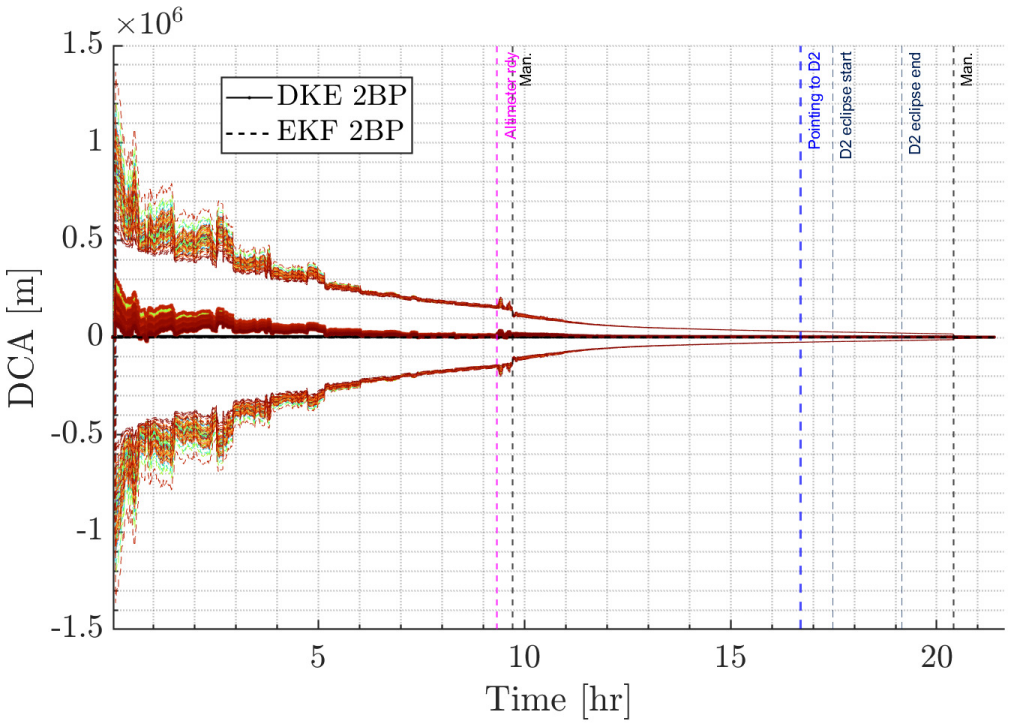


Figure 5.18: Cartesian HF: prediction of distance at closest approach with $3\sigma$ bound (dashed lines) compared against Hera EKF prediction and projection from "truth" - Nominal EXP.

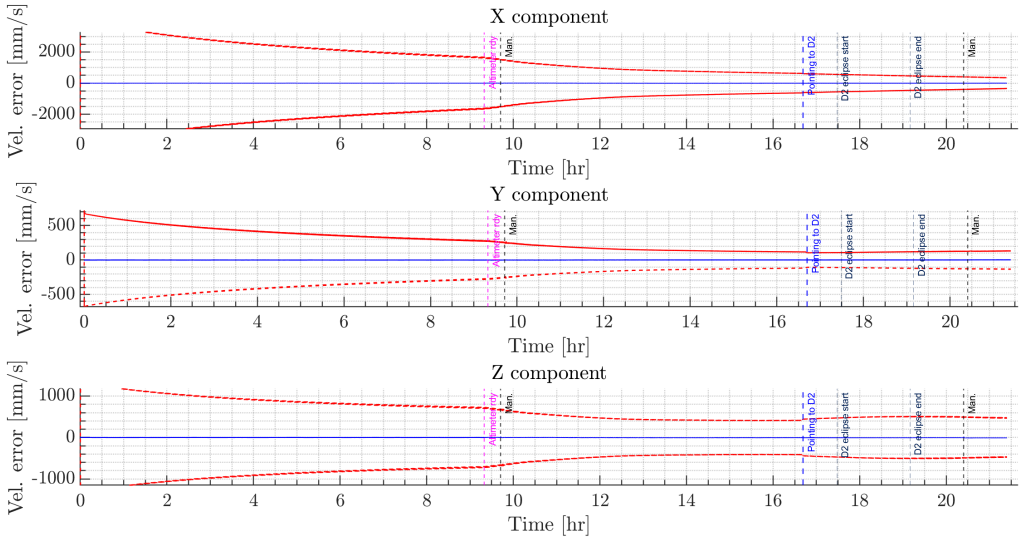


Figure 5.19: Cartesian HF: Velocity estimation errors and $3\sigma$ covariance bounds with $\mu$ parameter uncertainty - Nominal EXP @CAM frame.

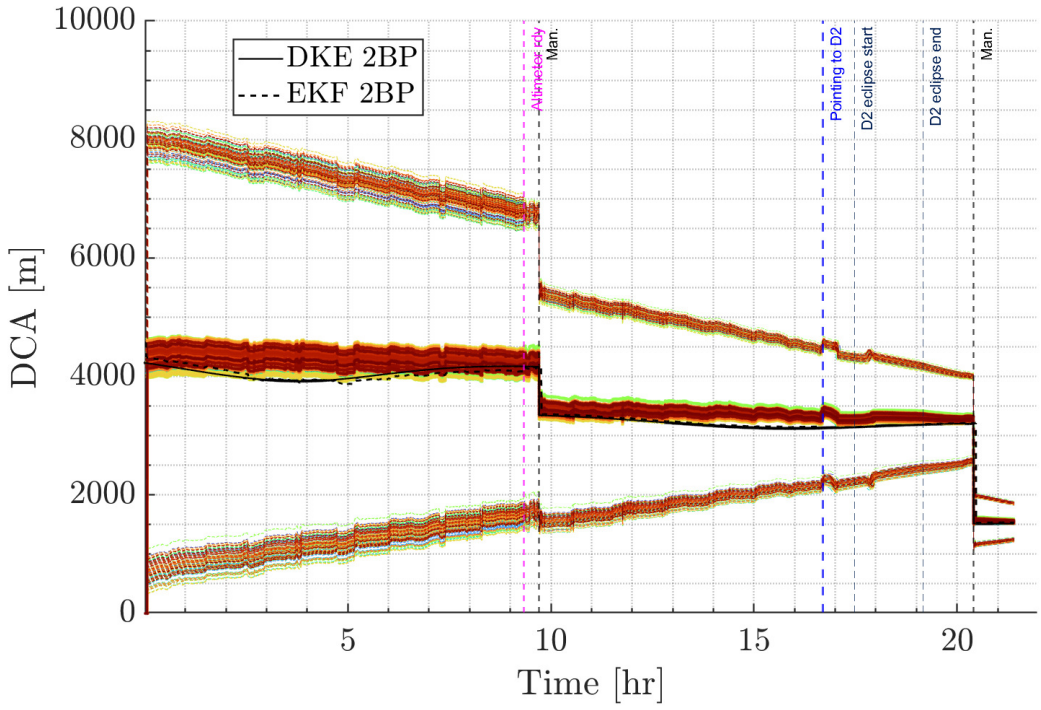


Figure 5.20: Cartesian KEP removing $\mu$ parameter uncertainty: prediction of distance at closest approach with $3\sigma$ bound (dashed lines) compared against Hera EKF prediction and projection from "truth" - Nominal EXP.

Table 5.5: Ensemble Statistics of DCA prediction error without $\mu$ parameter uncertainty, before the $1^{st}$ man. (A), before and after $2^{nd}$ man. (B and C) - Nominal EXP.

| Case | Med. Abs. [m] | Sigma Abs. [m] | Med. Rel. [%] | Sigma Rel. [%] |
|---|---|---|---|---|
| 1A | 147.5 | 156.5 | 3.624 | 3.874 |
| 2A | 231.4 | 128.0 | 5.658 | 3.233 |
| 3A | 135.5 | 115.4 | 3.324 | 2.914 |
| 1B | 239.7 | 122.5 | 7.521 | 3.845 |
| 2B | 154.8 | 54.8 | 4.820 | 1.749 |
| 3B | 76.18 | 52.84 | 2.383 | 1.687 |
| 1C | 165.2 | 67.16 | 10.91 | 4.429 |
| 2C | 50.70 | 17.18 | 3.347 | 1.134 |
| 3C | 32.55 | 16.30 | 2.149 | 1.076 |

- A: before first manoeuvre, $T_0 = 0$ to $T_1 = 9.71$ hr.
- B: after first manoeuvre and before the second, $T_1 = 9.71$ to $T_2 =$ hr.
- C: after the second manoeuvre, $T_2 = 20.40$ to $T_3 = 21.40$ hr.

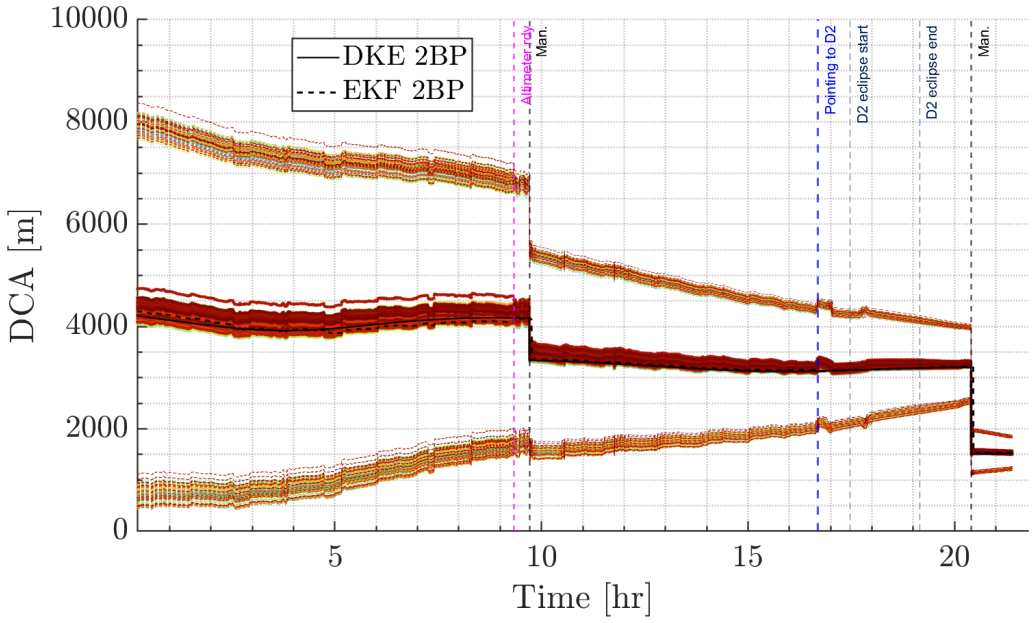


Figure 5.21: Cartesian HF removing $\mu$ parameter uncertainty: prediction of distance at closest approach with $3\sigma$ bound (dashed lines) compared against Hera EKF prediction and projection from "truth" - Nominal EXP.

The errors are computed with respect to the "true" DCA, obtained by projecting each true state under the 2BP assumption. The relative errors are computed normalizing by the same quantity.
The failure of the Keplerian state filter to converge to the trajectory becomes apparent through the persistent relative spread of estimated trajectories. Unlike the Keplerian filter, the Cartesian filter shows a diminishing spread over time. The initial apparent superiority of the Keplerian filter is merely a consequence of the reduced observability of range. Conversely, the Cartesian filters exhibit a progressive enhancement in accuracy over time. In particular, the HF model excels in predicting the DCA owing to its more precise motion model. Despite a position error comparable to that of the simplified motion model, the ensemble statistics demonstrate that the latter does not attain equivalent prediction accuracy. Notably, the disparity between the two diminishes as the spacecraft approaches the asteroids, suggesting that the simplification may still be acceptable.

## Normalized Error Square (NES) test

A further insight into the behaviour of the cartesian state filter is provided by the Normalized (Estimation) Error Square at a generic time $t_k$, given the reference state $\bar{\mathbf{x}}_k$, the

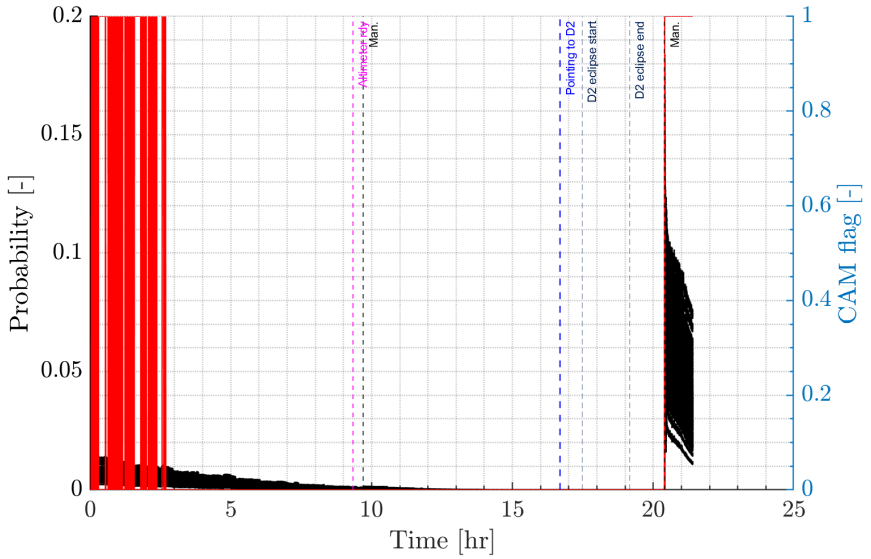


(a) Cartesian filter with 2BP dynamics.

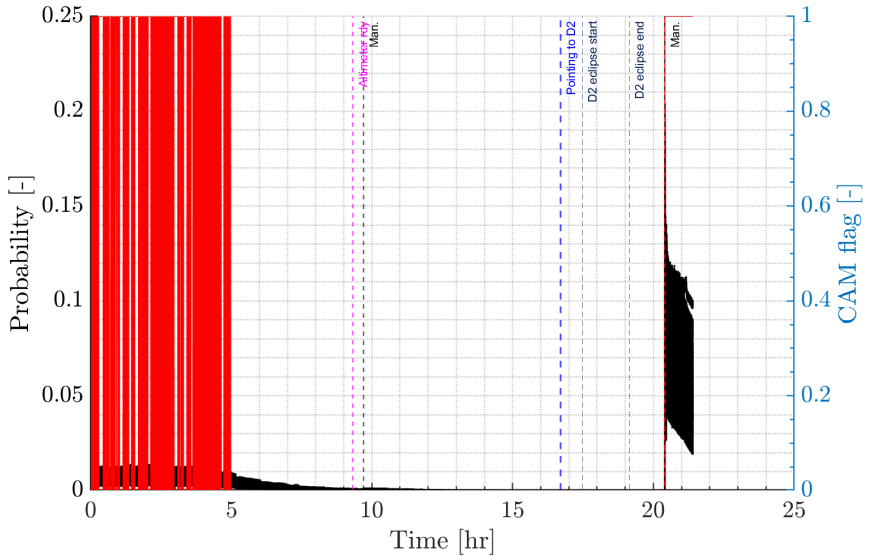


(b) Cartesian filter with refined dynamics.

Figure 5.22: PoC (black) and CAM flag (red) from DCA prediction of Cartesian filters without $\mu$ parameter uncertainty - Nominal EXP.

posterior estimated state $\hat{\mathbf{x}}_k^+$ and its covariance $P_k^{-1}$:

$$\varepsilon_k = (\hat{\mathbf{x}}_k^+ - \bar{\mathbf{x}}_k)\, P_k^{-1}\, (\hat{\mathbf{x}}_k^+ - \bar{\mathbf{x}}_k)^T$$

The definition and the test proposed in [80] were applied. Figure 5.23 shows the averaged NES statistics over the 100 samples and the hypothesis test bounds from a Chi-Squared

distribution with a 95% confidence level.

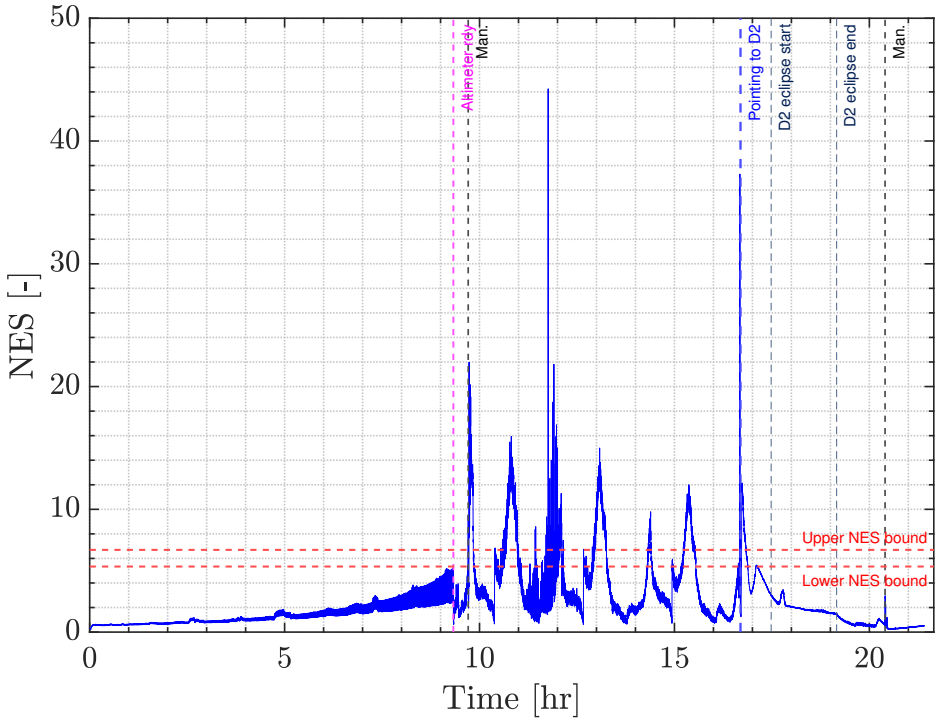


Figure 5.23: NES test of Cartesian HF filter - Nominal EXP @CAM frame.

As explained by [80], the NES manages to reveal both the presence of a bias in the estimated state and the possible insurgence of divergence due to filter over-confidence (i.e., precisely the case of the estimation error not being covered by the uncertainty bounds). Therefore, the evolution of the average NES confirms that systematic errors are strongly undermining the accuracy of the filter.

### 5.2.2. Unsafe case - HFM

The unsafe case unveiled another non-negligible issue in the use of the Keplerian state space, namely the fact that the filter is not able to cope with large uncertainties in combination with a low value of the eccentricity. During the $1^{st}$ manoeuvre of the test case, the trajectory's eccentricity drops below 1.5 while simultaneously the dispersion increases. Moreover, the method used for propagation through the Time law is not well suited at the boundary between elliptical and hyperbolic orbits [72], further hindering the robustness of the implementation. The present investigation found out that, irrespective of the process noise, a strong manoeuvre inevitably causes the filter estimate to become complex due to divergence.

For these reasons, the subsequent analysis focused on the Cartesian state filter only.

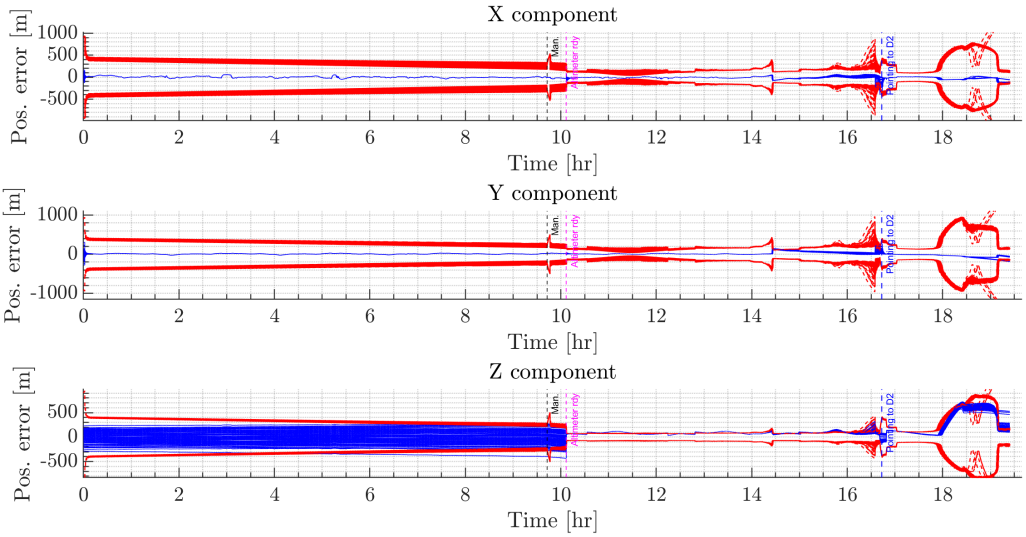


Figure 5.24: Cartesian HF: Estimation errors and $3\sigma$ covariance bounds with $3\sigma$ bound-Unsafe EXP @CAM frame.

Figures 5.24 and 5.26 show the results of the Cartesian HF filter consistency and the predicted DCA. Similarly to the nominal scenario, the simplified dynamics yields results consistent with the previous considerations.

At the same time, the information derived from centroiding facilitates accurate estimation along the X and Y CAM axes, but the limitations in observability along the boresight direction remain unaltered. The activation of the altimeter helps again to reduce the estimation error of this component. Nevertheless, the estimate bias is more pronounced compared to the nominal scenario and largely surpasses the uncertainty bounds. This error amplifies as the spacecraft approaches the asteroids. Figure 5.25 presenting the averaged NES statistics, further illustrates and supports these observations. The transition to pointing towards Dimorphos, influenced by the non-nominal Sun illumination conditions, initiates a gradual yet noticeable divergence in the filter. This divergence is more prominent in the bore-sight component. Nevertheless, it is important to emphasize that, in principle, such a situation should not occur, as the system would be designed to command a CAM well before the spacecraft reaches such a critical point.
Overall, the filter succeeds in maintaining the tracking of the trajectory after the $1^{st}$ manoeuvre. Unlike the Nominal case however, the state noise compensation falls short of ensuring consistency of the position states if the nominal tuning is maintained. Regarding the DCA prediction, the filter exhibits effective performance in tracking the trajectory changes resulting from the manoeuvre and in identifying the associated safety issue.

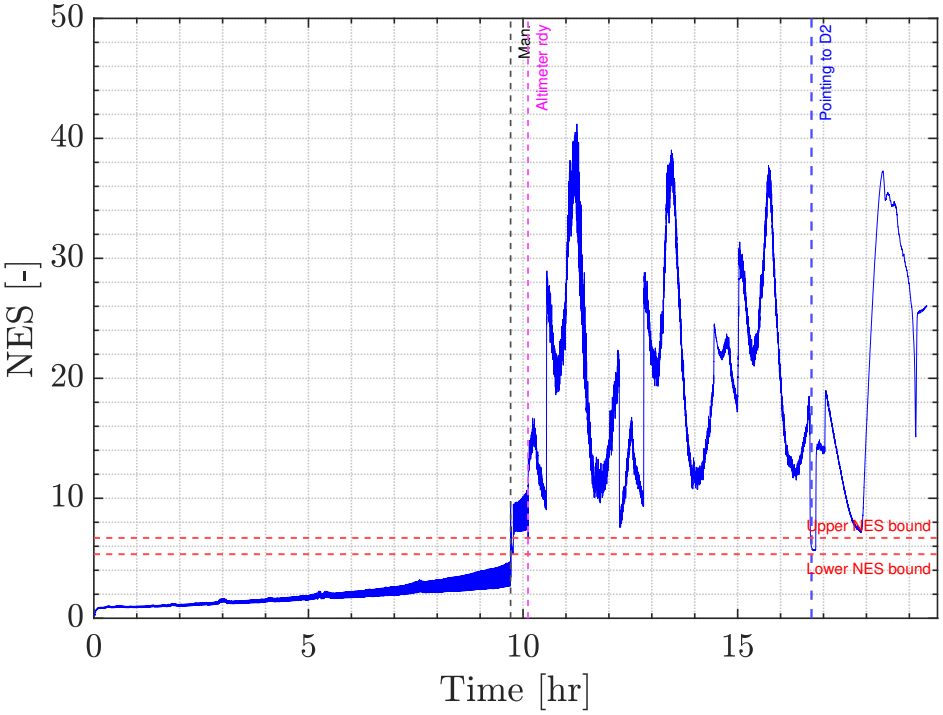


Figure 5.25: NES test of Cartesian HF filter - Unsafe EXP @CAM frame.

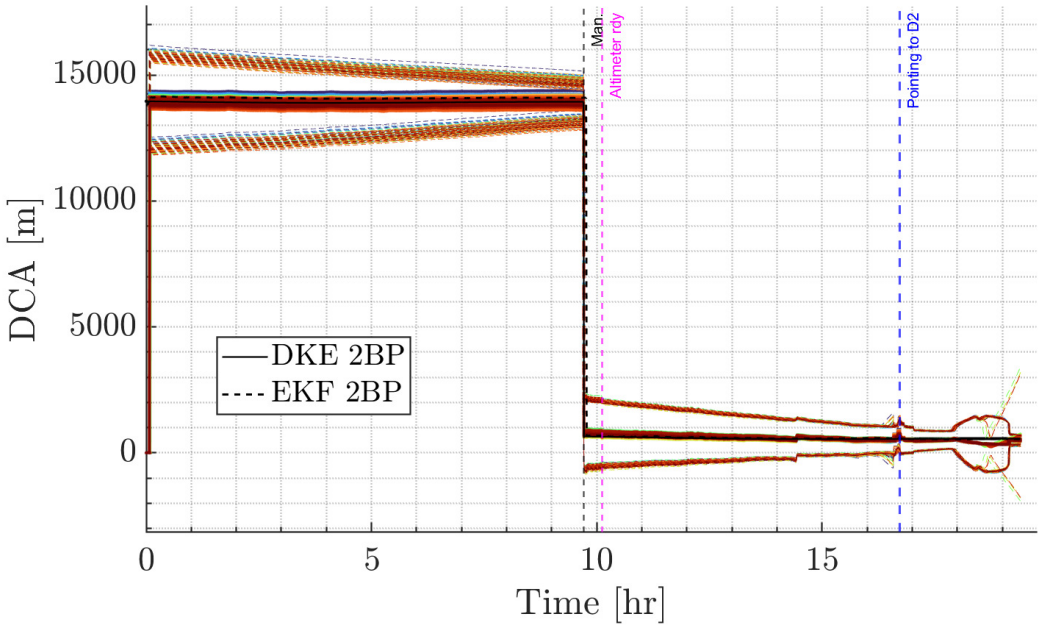


Figure 5.26: Cartesian HF: prediction of distance at closest approach (dashed lines) compared against Hera EKF prediction and projection from "truth" - Unsafe EXP.

However, it is essential to acknowledge that the scenario where the $\Delta\mathbf{V}$ applied to the spacecraft is precisely known represents a relatively straightforward condition. Excluding the occurrence of filter divergence, the likelihood of missed detection in instances of such close approaches is low.

Table 5.6: Ensemble Statistics of DCA prediction error without $\mu$ parameter uncertainty before (A) and after (B) the critical manoeuvre - Unsafe EXP.

| Case | Med. Abs. [m] | Sigma Abs. [m] | Med. Rel. [%] | Sigma Rel. [%] |
|---|---|---|---|---|
| 1A | - | - | - | - |
| 2A | 19.90 | 130.4 | 0.143 | 0.939 |
| 3A | 21.92 | 181.3 | 0.158 | 1.305 |
| 1B | - | - | - | - |
| 2B | 79.43 | 33.69 | 14.115 | 6.135 |
| 3B | 26.38 | 29.60 | 4.750 | 5.363 |

The PoC and CAM flag plots in the unsafe EXP are reported in appendix (A.6, A.7). These only confirm that both the simplified and the HF models correctly trigger the flag when required. However, since the covariance evolution essentially mirrors the nominal case, in this instance this is primarily attributable to the significantly larger DCA during the initial segment of the trajectory.

## 5.3. Filters bank Hypothesis testing

The results discussed in section 5.2 showed that the keplerian state space leads the filter to fail in conditions deemed relevant for this study. Therefore, only the filter using cartesian state vector were examined in evaluating the filters bank concept. Specifically, the simplified 2BP motion model was employed since achieving enhanced accuracy is not a strict requirement: the SPRT focuses on the comparison of performance of one filter *relative* to its complementary counterpart.

**Tuning parameters** The tuning parameters of the method, namely the targeted probability of false alarm and missed detection, were set equal to values aimed at minimizing the likelihood of a missed detection in the unsafe scenario:

$$\bar{P}_{fa} = 1 \times 10^{-4} \qquad \bar{P}_{md} = 1 \times 10^{-10}$$

The boundary values follow from (4.66, 4.67): $A = 9.999 \times 10^{+9}$, $B = 1 \times 10^{-4}$. For the reasons explained in chapter 4, neither process noise nor consider parameters were used.

The threshold of the decision counter for the coupled configuration was set equal to 6 measurement updates when only centroid information is available, and to the corresponding 288 after the altimeter activation (i.e., to have the equivalent elapsed time). In other words, a test restart would be triggered *if* a decision is reached *and* no change occurs before the threshold is exceeded. Moreover, the test is only activated 2 hours after the start of the navigation to guarantee the navigation filter convergence. This parameter was decided heuristically and must vary on a case-by-case basis. The last tuning parameter is the time threshold for the decision mode switch, deemed necessary when one of the two filters stops accepting measurements as explained in section 4.5.5. The latter was fixed to 1 hr.
For each sample run, a random scattering of the initial errors was performed as in section 4.2.3. Notice that this causes the time instant and possibly the total number of resets to differ despite the measurements and tuning being the same. The number of "reached decisions" as well as the number of errors (either false alarm or missed detection according to the scenario) were counted.

### 5.3.1. Nominal EXP trajectory test

The analysis was primarily focused on the coupled configuration. In fact, the partially-coupled one is truly only a particular case of the first, in which the reset is executed once in correspondence of a manoeuvre. In particular, the test is halted during whole duration of the manoeuvres and re-initialized from the navigation filter mean state and covariance immediately after.

The likelihood ratio driving the decision is plotted over time in figure 5.27 in logarithmic scale. The decision bounds A and B correspond to the horizontal dashed lines, whereas, identically to section 5.2, the major events are reported as vertical lines. Firstly, it is notable that the effect of the scattering is primarily visible during bearing-only navigation, likely due to the larger spread in the position error. Subsequently, the differences after the altimeter activation become almost negligible and all the sample run attain similar decisions. This was deemed possibly related to the shrinkage in the position error spread, as also exhibited in section 5.2. It is evident that an incorrect decision systematically occurs between $T = 3\,hr$ and $T = 4\,hr$. A second false alarm is triggered around $T = 12\,hr$, whereas, in all the other cases, the test correctly evaluates the trajectory as safe. Table 5.7 reports the corresponding statistics, supporting the above considerations. Since all the measurements are incorporated by the filters without any editing, the possibility of the incorrect decisions being caused by measurements outliers was deemed likely but cannot be verified within the scope of the present study.

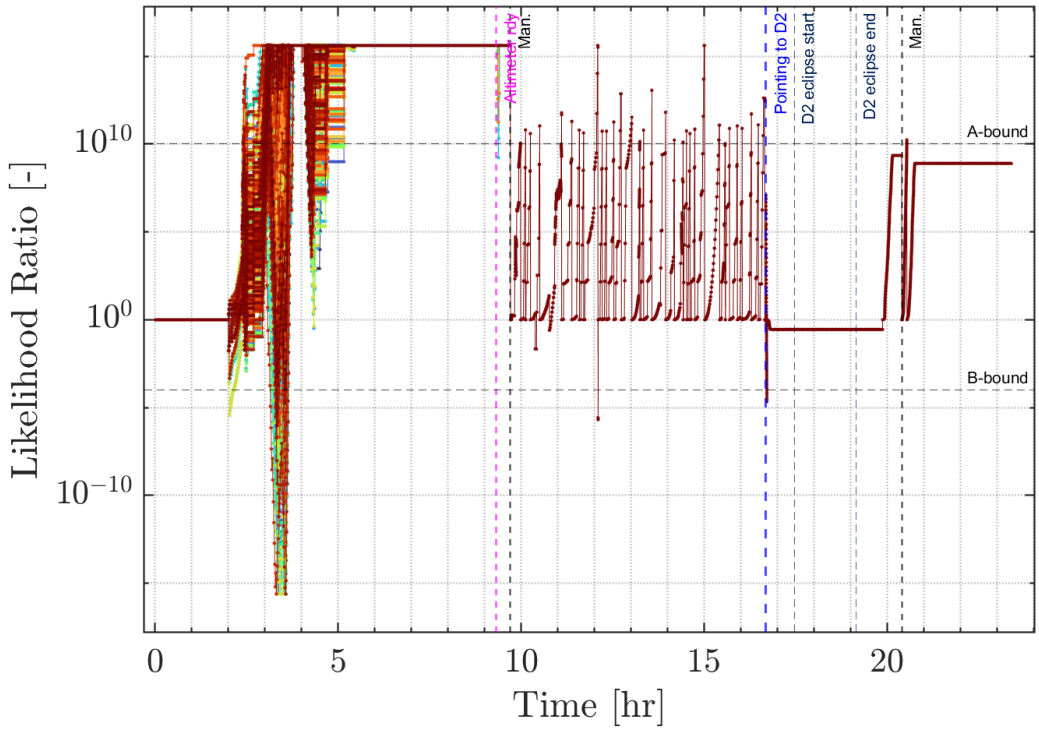


Figure 5.27: Evolution over time of the Innovations Likelihood ratio - Nominal EXP (Coupled).

The selection of tuning parameters were found to have a significant influence on the test performance, with the targeted probabilities almost entirely determining the number of incorrect decisions. Similarly, the thresholds for the decision to be tagged as "taken" are the driving factor of the number of decisions and resets occurring during each execution.

Figures 5.28 and 5.29 illustrate the number of accepted measurements by the two filters. The centroiding coordinates are counted separately, meaning that a single measurement indicates the altimeter availability. It is important to recall that the $H_0$ filter is the one being constrained as it hypothesizes an unsafe trajectory. After the switch of the pointing toward Dimorphos, the number of accepted measurements drops to zero for the majority of the remaining hours of navigation. In this case, the test adjusts the decision mode to utilize the information about which filter is no longer performing updates due to physically inconsistent measurements (section 4.5.5), which is not reflected in the likelihood ratio. No false alarm occurs in this mode, suggesting that the chosen tuning might be appropriate. The dots denoting acceptance of measurements after the event are a result of the reset occurrences.

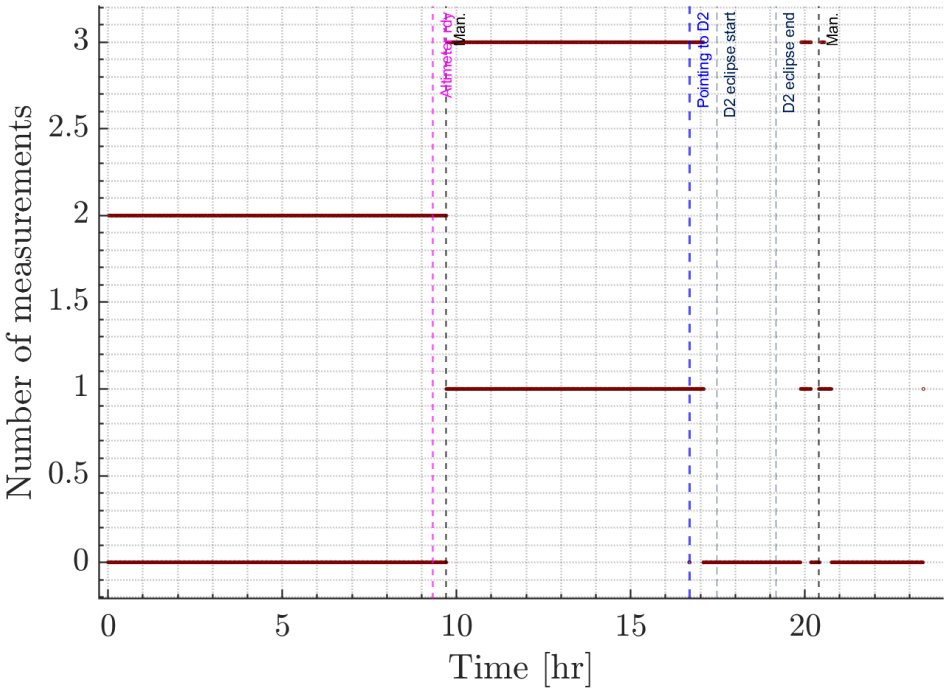


Figure 5.28: Number of measurements accepted by $H_0$ filter over time - Nominal EXP (Coupled).

Finally, figure 5.30 shows that the CAM flag evolution is consistent with the Likelihood ratio and the statistics.

Table 5.7: Statistics of performance of filters bank - Nominal EXP (Coupled).

| | |
|---|---|
| N° samples | 1000 |
| Total N° decisions | 37000 |
| Total N° f.a. | 2000 |
| Ratio N° f.a./dec | 5.4% |
| Med. of N° dec./sample | 37 |

### 5.3.2. Unsafe EXP trajectory test

The same analysis was conducted for the unsafe scenario. In this case, the trajectory is safe until the first maneuver, after which Hera follows a very steep trajectory toward Didymos. Consequently, it was necessary to evaluate the two phases separately. Figure 5.31 shows the Likelihood ratio resulting from the filters bank in logarithmic scale of the 100 samples. A visual inspection confirms that the safety of the first window is correctly

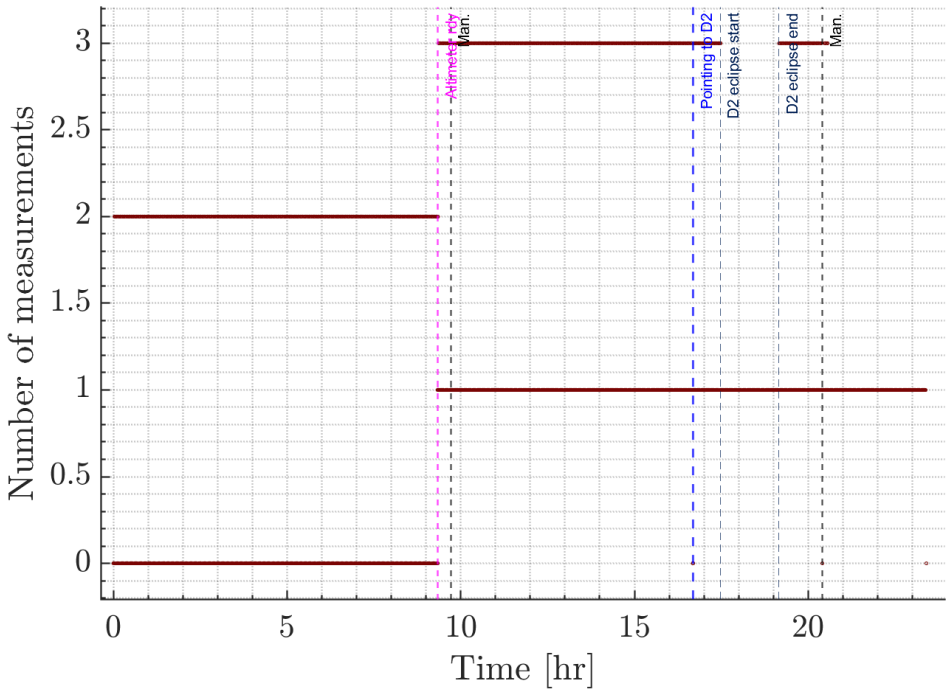


Figure 5.29: Number of measurements accepted by $H_1$ filter over time - Nominal EXP (Coupled).

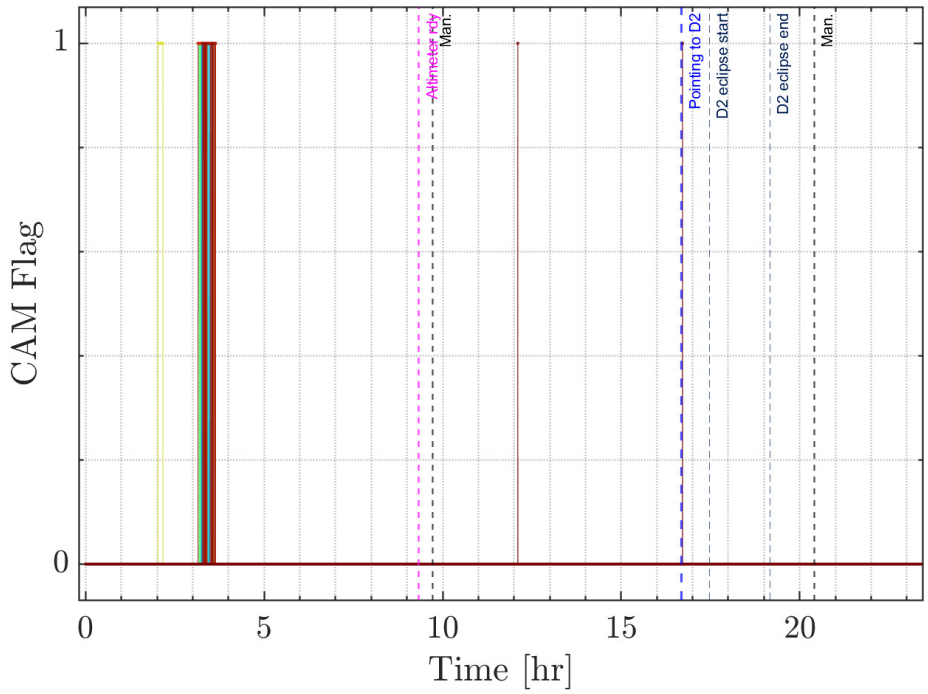


Figure 5.30: CAM flag - Nominal EXP (Coupled)

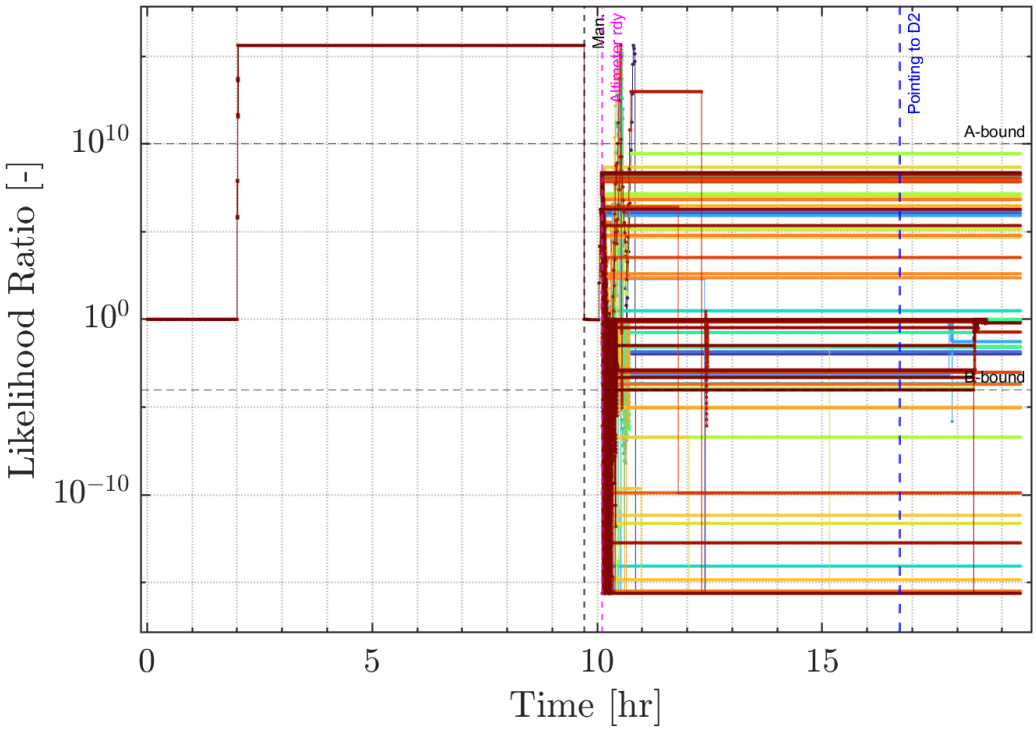


Figure 5.31: Evolution over time of the Innovations Likelihood ratio - Unsafe EXP (Coupled).

assessed in all cases, with no false alarm being triggered. Similarly to the single filter approach, the farther the minimum distance is from the Keep-out sphere radius, the easier the evaluation becomes.

As designed, no decision occurs during the maneuvering phase as the test is reset at each $\Delta\mathbf{v}$ execution. Once the range information becomes available, the ratio for most sample runs quickly moves toward accepting the $H_1$ hypothesis; however, several sample runs show a single incorrect decision being taken. Additionally, the nominal decision mode does not last long: as figure 5.33 demonstrates, the $H_1$ filter quickly stops accepting measurements. This is what causes the Likelihood ratio to remain constant after $T \simeq 10.344\,hr$. Nevertheless, it is significant that multiple resets occur in this short time frame and all lead to the same correct evaluation. The FD may eventually conclude that the trajectory is indeed unsafe based on all the available information.

The CAM flag history shown in fig. 5.34 reveals a shortcoming of the selected value for the secondary mode of the test: the threshold of $1\,hr$ for the decision based on the measurement outage is apparent in the fact that not all sample runs eventually achieve the correct decision after the last test restart. This seems the most reasonable explanation, as some of the simulations experience a reset within $1, hr$ from the end of the run.

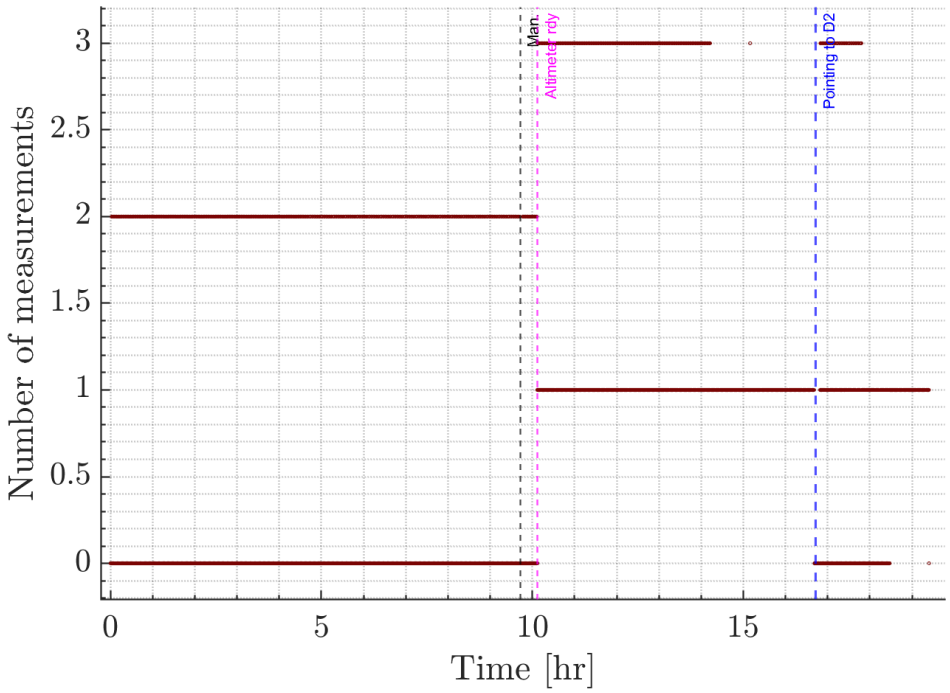


Figure 5.32: Number of measurements accepted by $H_0$ filter over time - Unsafe EXP (Coupled).

Table 5.8: Statistics of performance of filters bank - Unsafe EXP (Coupled).

| | |
|---|---|
| N° samples | 1000 |
| Total N° decisions | 42510 |
| Total N° m.d. | 8 |
| Ratio N° m.d./dec | 0.0188% |
| Med. of N° dec./sample | 69 |

At the same time, the interpretation is substantiated by the statistics in table 5.8. The results also confirm that the test is more prone to produce a conservative decision leaning toward a false alarm rather than a missed detection as desired. In the majority of cases, no decision error occurs. Despite the positive performance, the current analysis was not exhaustive enough to thoroughly verify the method, but was deemed sufficient to prove that concept can work as intended. The effect of the tuning to reduce the occurrence of missed detection cases is indeed reflected by the results although it cannot be conclusively stated that the targeted probabilities are attained by the test performance.

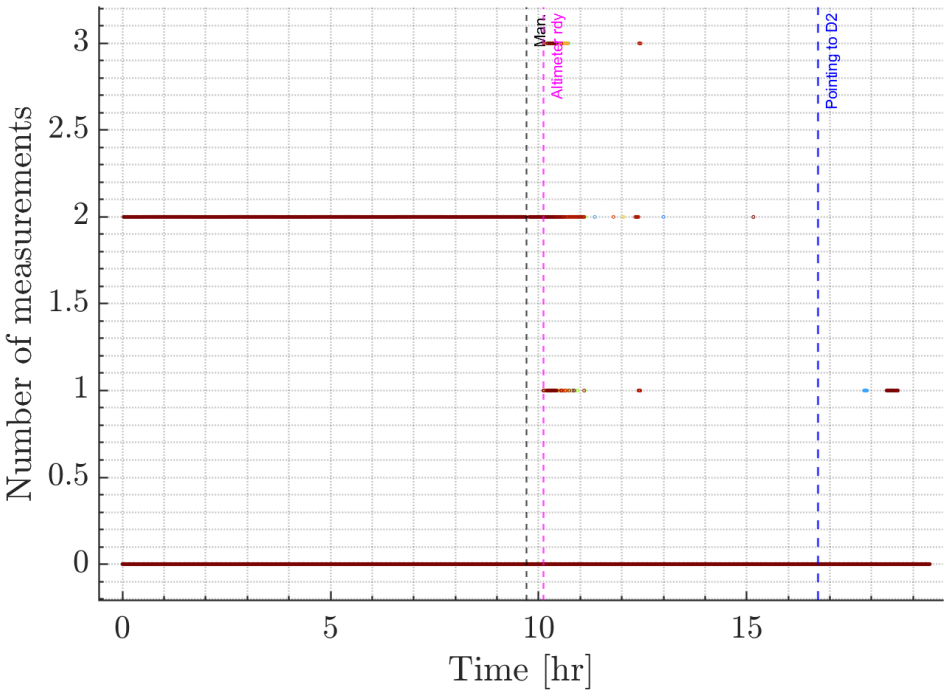


Figure 5.33: Number of measurements accepted by $H_1$ filter over time - Unsafe EXP (Coupled).

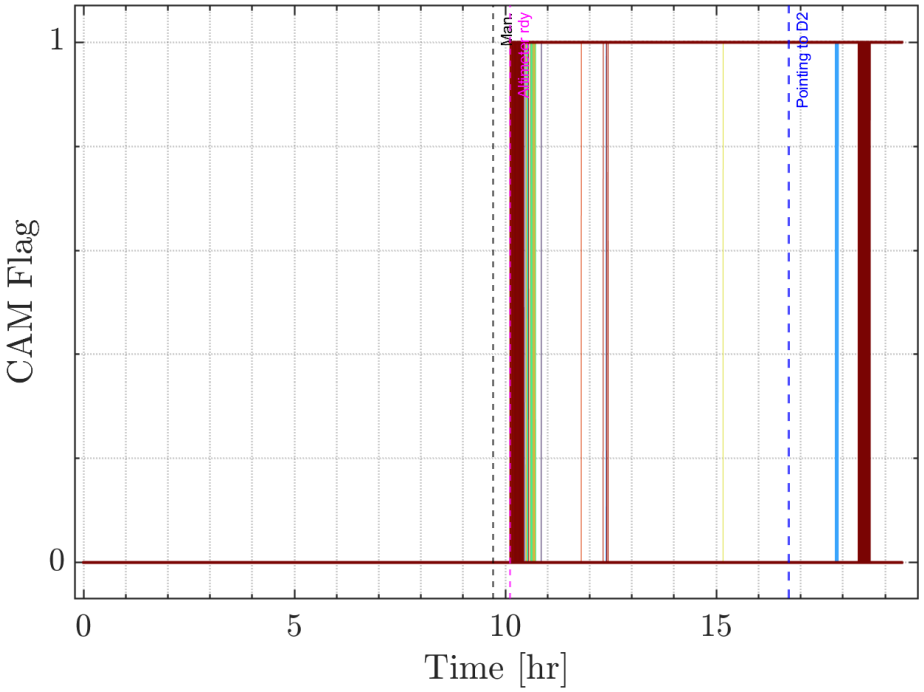


Figure 5.34: CAM flag - Unsafe EXP (Coupled).

# 6 | Summary and final considerations

Starting from the existing paradigm in handling uncertainties and safety in interplanetary missions, the presented work has endeavored to address a central question: Is it feasible to formulate failure detection strategies with the objectives of:

- Minimizing the spacecraft's dependence on Flight Dynamics planning.
- Enhancing autonomy in anticipation of numerous upcoming smaller missions.

Chapter 2 provided a succinct overview of recent missions akin to Hera, delineating challenges, trajectory design, and target bodies. While various methods in Space Situational Awareness (SSA) were scrutinized, none proved suitable for extension. Finally, Chapter 2 delved into the preliminaries necessary for the proposed strategies.

In Chapter 3, the mission scenario was characterized, encompassing descriptions and considerations specifically tied to the Hera spacecraft, simulation models, and a perturbation analysis. This aimed to evaluate the degree of assumptions that could yield acceptable results. Confirming prior findings, small celestial bodies were noted for presenting a highly uncertain, intricate, and rapidly changing environment. Dissipative forces like Solar Radiation Pressure (SRP) are no longer negligible compared to planetary orbits.

Chapter 4 thoroughly exposed the tested methods, justifying their formulations and highlighting anticipated limitations and use cases. Three algorithms, progressively complex, were developed by adapting existing concepts from literature to fit the Hera scenario and objectives. Concurrently, efforts were made to diminish computational time and ensure sufficient flexibility for practical applications.
Finally, chapter 5 showcased various test cases for the preliminary assessment of the algorithms concepts, evaluating the impact of the design assumptions and their performance.

## 6.1. Conclusive remarks

The challenge of developing an autonomous failure detection system involving only Navigation functionalities was tackled. However, *there appears to be no method simpler and more cost-effective than the navigation filter itself to conduct a trajectory safety assessment.*
Significant limitations in achievable accuracy were identified for the MOCRE when applied to the Hera mission scenario, despite its promising initial results. Specifically, the ability to filter out measurement noise and correct biases was deemed insufficient for reliable application in challenging environments like the Hera mission scenario, precisely where it is most needed. Additionally, the approach's dependence on the same limited set of measurements as the navigation filters makes it challenging to justify deployment in the actual on-board software. Although more complex estimation methodologies exist beyond the Least Square algorithm, their implementation may be hindered by associated costs from various perspectives.
Similar considerations applied to the second proposed approach. Despite its original aim of providing an independent and more robust safety assessment while reducing computational demand compared to the complete navigation filter, this goal was not achieved. The closest approach distance was found to be too sensitive to velocity estimation errors for the bias error sources to be left uncorrected.

The hypothesis testing framework, conceived as an independent check of the navigation solution rather than a completely independent system, emerged as the least explored and conventional of the three. While some promising outcomes were highlighted in the analysis of Chapter 5, the presented concept still requires further testing to properly characterize its performance.
In summary, the questions raised in chapter 2 literature review have been partially addressed, indicating that tools for detecting a dangerous failure in the desired trajectory can be designed to offer some degree of accuracy. However, the requirement for the assessment to be entirely independent appears overly stringent, especially considering the limited resources, both from the on-board computer standpoint and, even more critically, from the point of view of measurements acquisition

## 6.2. Future work

A list of potential future advancements and explorations is outlined below, categorized by algorithm. Firstly, it is emphasized the necessity of more comprehensive testing of all the methods, which were not included within the scope of the current study. Specifically, it is recommended to conduct Monte Carlo analyses involving the dispersion of both "true" and "on-board" parameters. This would be essential to characterize the collective performance of the algorithms in diverse scenarios. The current work, by contrast, assessed them solely through individual runs or sensitivity analyses focused on initialization errors.

**MOCRE**

1. Application of High-order uncertainty propagation methods such as DA to remove the assumptions required in the covariance computation.
2. Investigation to assess various batch smoothing/filtering techniques.
3. Replacement of the threshold-based decision with data-drive methodologies.

**Parallel filtering approach**

1. Re-working as smoother rather than as forward sequential filter.

**Filters bank Hypothesis testing**

1. Application of Differential Algebra as projector function in the Sigma point projector to enforce the constraint.
2. Improvements to the robustness of the filtering process to avoid divergence and/or covariance becoming non positive definite.

**On the trajectory safety assessment** In conclusion, broader considerations on how trajectory safety could be guaranteed in an autonomous way are encompassed. In the context of binary asteroid systems, it is deemed essential to develop methods for independently assessing collision risks for each of the two bodies, particularly when trajectories cross the secondary orbit. In such scenarios, the assumptions underlying the investigated methods completely break down. Moreover, the applicability of the "keep-out sphere" approach may be excessively restrictive, especially when the orbital radius of the secondary body is substantial.
The author perceives limited room for resolving the issue solely from a Navigation perspective, given the typically constrained set of observables, along with significant associated

uncertainty and variability. These factors pose challenges in predicting the trajectory's safety. Consequently, on-board guidance and control algorithms such as Model Predictive Control [26] yielding solutions with guaranteed safety, seems more fitting for use in future missions. In this context, the Navigation system design could pivot towards enhancing the accuracy of the estimation process and improving the robustness against dynamics modeling uncertainties.

# Bibliography

[1] M. Abramowitz and I. A. Stegun. *Handbook of Mathematical Functions with Formulas, Graphs, and Mathematical Tables*. Dover, New York, ninth dover printing, tenth gpo printing edition, 1964.

[2] A. Accomazzo, P. Ferri, S. Lodiot, J.-L. Pellon-Bailon, A. Hubault, R. Porta, J. Urbanek, R. Kay, M. Eiblmaier, and T. Francisco. Rosetta operations at the comet. *Acta Astronautica*, 115:434–441, 2015.

[3] N. Adurthi, P. Singla, and T. Singh. The conjugate unscented transform—an approach to evaluate multi-dimensional expectation integrals. In *2012 American Control Conference (ACC)*, pages 5556–5561. IEEE, 2012.

[4] S. Alfano. A numerical implementation of spherical object collision probability. *The Journal of the Astronautical Sciences*, 53:103–109, 2005.

[5] N. Amor, G. Rasool, and N. C. Bouaynaya. Constrained state estimation–a review. *arXiv preprint arXiv:1807.03463*, 2018.

[6] P. G. Antreasian, C. D. Adam, J. Geeraert, J. M. Leonard, E. Lessac-Chenen, A. Levine, J. McAdams, L. K. McCarthy, D. Nelson, B. Page, J. Y. Pelgrift, E. Sahr, D. Wibben, B. Williams, K. Williams, K. Berry, K. Getzandanner, M. Moreau, S. Rieger, B. W. Ashman, D. E. Highsmith, and D. Lauretta. OSIRIS-REx Proximity Operations and Navigation Performance at (101955) Bennu.

[7] R. H. Battin. *An Introduction to the Mathematics and Methods of Astrodynamics, Revised Edition*. American Institute of Aeronautics and Astronautics, Inc., Reston, VA, Jan. 1999. ISBN 978-1-56347-342-5 978-1-60086-154-3. doi: 10.2514/4.861543. URL `https://arc.aiaa.org/doi/book/10.2514/4.861543`.

[8] C. Buonagura, M. Pugliatti, and F. Topputo. Image Processing Robustness Assessment of Small-Body Shapes. *J Astronaut Sci*, 69(6):1744–1765, Dec. 2022. ISSN 2195-0571. doi: 10.1007/s40295-022-00348-6. URL `https://doi.org/10.1007/s40295-022-00348-6`.

[9] A. Capannolo, G. Zanotti, M. Lavagna, and G. Cataldo. Formation flying orbits and gnc design in binary asteroid systems. *Advances in Space Research*, 2023.

[10] J. R. Carpenter and C. N. D'Souza. Navigation filter best practices. 2018.

[11] J. R. Carpenter and F. L. Markley. Current-state constrained filter bank for wald testing of spacecraft conjunctions. In *23rd International Symposium on Space Flight Dynamics*, number GSFC. CP. 7474.2012, 2012.

[12] J. R. Carpenter and F. L. Markley. Sequential Wald Test Employing a Constrained Filter Bank: Application to Spacecraft Conjunctions. *J Optim Theory Appl*, 191 (2):440–458, Dec. 2021. ISSN 1573-2878. doi: 10.1007/s10957-021-01847-6. URL https://doi.org/10.1007/s10957-021-01847-6.

[13] J. R. Carpenter, F. L. Markley, and D. Gold. Sequential Probability Ratio Test for Collision Avoidance Maneuver Decisions. *J of Astronaut Sci*, 59(1-2):267–280, June 2012. ISSN 0021-9142, 2195-0571. doi: 10.1007/s40295-013-0017-2. URL http://link.springer.com/10.1007/s40295-013-0017-2.

[14] J. R. Carpenter, F. L. Markley, and D. Gold. Wald Sequential Probability Ratio Test for Analysis of Orbital Conjunction Data. In *AIAA Guidance, Navigation, and Control (GNC) Conference*, Boston, MA, Aug. 2013. American Institute of Aeronautics and Astronautics. ISBN 978-1-62410-224-0. doi: 10.2514/6.2013-5187. URL https://arc.aiaa.org/doi/10.2514/6.2013-5187.

[15] G. Chang. Robust Kalman filtering based on Mahalanobis distance as outlier judging criterion. *Journal of Geodesy*, 88(4):391–401, Apr. 2014. ISSN 0949-7714, 1432-1394. doi: 10.1007/s00190-013-0690-8. URL http://link.springer.com/10.1007/s00190-013-0690-8.

[16] A. Cheng, J. Atchison, B. Kantsiper, A. Rivkin, A. Stickle, C. Reed, A. Galvez, I. Carnelli, P. Michel, and S. Ulamec. Asteroid impact and deflection assessment mission. *Acta Astronautica*, 115:262–269, 2015. ISSN 0094-5765. doi: https://doi.org/10.1016/j.actaastro.2015.05.021. URL https://www.sciencedirect.com/science/article/pii/S0094576515002040.

[17] A. F. Cheng, H. F. Agrusa, B. W. Barbee, A. J. Meyer, T. L. Farnham, S. D. Raducan, D. C. Richardson, E. Dotto, A. Zinzi, V. Della Corte, et al. Momentum transfer from the dart mission kinetic impact on asteroid dimorphos. *Nature*, 616 (7957):457–460, 2023.

[18] A. Comellini, D. Casu, E. Zenou, V. Dubanchet, and C. Espinosa. Incorporating

Delayed and Multirate Measurements in Navigation Filter for Autonomous Space Rendezvous. *Journal of Guidance, Control, and Dynamics*, 43(6):1164–1172, June 2020. ISSN 1533-3884. doi: 10.2514/1.G005034. URL https://arc.aiaa.org/doi/10.2514/1.G005034.

[19] Coppola. Socrates plus satellite orbital conjunction reports assessing threatening encounters in space, 2022. URL https://Coppola.org/SOCRATES/. Last visited: 11-22-2023.

[20] V. T. Coppola. EVALUATING THE SHORT ENCOUNTER ASSUMPTION OF THE PROBABILITY OF COLLISION FORMULA. 2012.

[21] R. De Maesschalck, D. Jouan-Rimbaud, and D. Massart. The Mahalanobis distance. *Chemometrics and Intelligent Laboratory Systems*, 50(1):1–18, Jan. 2000. ISSN 01697439. doi: 10.1016/S0169-7439(99)00047-7. URL https://linkinghub.elsevier.com/retrieve/pii/S0169743999000477.

[22] P. Di Lizia, M. Massari, F. Cavenago, and A. Wittig. Assessment of onboard da state estimation for spacecraft relative navigation. *Final report, ESA*, 2017.

[23] N. G. Dias, B. N. Arribas, P. Gordo, T. Sousa, J. Marinho, R. Melicio, A. Amorim, P. Michel, and N.-M. Team. HERA Mission LIDAR Altimeter Implementation. *IOP Conf. Ser.: Mater. Sci. Eng.*, 1024(1):012112, Jan. 2021. ISSN 1757-899X. doi: 10.1088/1757-899X/1024/1/012112. URL https://dx.doi.org/10.1088/1757-899X/1024/1/012112. Publisher: IOP Publishing.

[24] M. P. et al. The ESA Hera Mission: Detailed Characterization of the DART Impact Outcome and of the Binary Asteroid (65803) Didymos. *Planet. Sci. J.*, 3(7), July 2022. ISSN 2632-3338. doi: 10.3847/PSJ/ac6f52. URL https://iopscience.iop.org/article/10.3847/PSJ/ac6f52.

[25] F. Ferrari, V. Franzese, M. Pugliatti, C. Giordano, and F. Topputo. Trajectory Options for Hera's Milani CubeSat Around (65803) Didymos. *J Astronaut Sci*, 68 (4), Dec. 2021. ISSN 0021-9142, 2195-0571. doi: 10.1007/s40295-021-00282-z. URL https://link.springer.com/10.1007/s40295-021-00282-z.

[26] T. A. Frekhaug, M. Sanjurjo-Rivo, and M. Soler. Output-feedback tube model predictive control for asteroid circumnavigation and descent. *Journal of Guidance, Control, and Dynamics*, pages 1–10, 2023.

[27] J. Frey, J. De Schutter, and M. Diehl. Fast integrators with sensitivity propagation

for use in casadi. In *2023 European Control Conference (ECC)*, pages 1–6. IEEE, 2023.

[28] J. L. Geeraert and J. W. McMahon. Square-Root Unscented Schmidt–Kalman Filter. *Journal of Guidance, Control, and Dynamics*, 41(1):280–287, Jan. 2018. ISSN 0731-5090, 1533-3884. doi: 10.2514/1.G002921. URL https://arc.aiaa.org/doi/10.2514/1.G002921.

[29] M. Ghezal, B. Polle, C. Rabejac, and J. Montel. Gyro stellar attitude determination. In *Guidance, Navigation and Control Systems*, volume 606, 2006.

[30] J. Gil-Fernandez and G. Ortega-Hernando. Autonomous vision-based navigation for proximity operations around binary asteroids. *CEAS Space J*, 10(2):287–294, June 2018. ISSN 1868-2510. doi: 10.1007/s12567-018-0197-5. URL https://doi.org/10.1007/s12567-018-0197-5.

[31] J. GIL-FERNANDEZ, M. CASASCO, I. CARNELLI, P. MARTINO, and M. KUPPERS. HERA autonomous Guidance, Navigation and Control experiments: enabling better asteroid science future missions. page 11 pages, 2019. doi: 10.13009/EUCASS2019-209. URL https://www.eucass.eu/doi/EUCASS2019-0209.pdf. Artwork Size: 11 pages Medium: PDF Publisher: Proceedings of the 8th European Conference for Aeronautics and Space Sciences. Madrid, Spain, 1-4 july 2019.

[32] K.-H. Glassmeier, H. Boehnhardt, D. Koschny, E. Kührt, and I. Richter. The rosetta mission: flying towards the origin of the solar system. *Space Science Reviews*, 128: 1–21, 2007.

[33] H. R. Goldberg, Ö. Karatekin, B. Ritter, A. Herique, P. Tortora, C. Prioroc, B. G. Gutierrez, P. Martino, and I. Carnelli. The juventas cubesat in support of esa's hera mission to the asteroid didymos. 2019.

[34] R. Hartley and A. Zisserman. *Multiple view geometry in computer vision*. Cambridge University Press, Cambridge, UK, 2nd ed edition, 2004. ISBN 978-0-511-18711-7. OCLC: 171123855.

[35] D. Jewitt, Y. Kim, J. Li, and M. Mutchler. The Dimorphos Boulder Swarm. *ApJL*, 952(1):L12, July 2023. ISSN 2041-8205, 2041-8213. doi: 10.3847/2041-8213/ace1ec. URL https://iopscience.iop.org/article/10.3847/2041-8213/ace1ec.

[36] JPL. Nasa jpl solar system dynamics, 2023. URL https://ssd.jpl.nasa.gov/ftp/eph/small_bodies/dart/dimorphos/. Last visited: 11-22-2023.

[37] S. Julier. The scaled unscented transformation. In *Proceedings of the 2002 American*

*Control Conference (IEEE Cat. No.CH37301)*, pages 4555–4559 vol.6, Anchorage, AK, USA, 2002. IEEE. ISBN 978-0-7803-7298-6. doi: 10.1109/ACC.2002.1025369. URL http://ieeexplore.ieee.org/document/1025369/.

[38] S. Julier and J. Uhlmann. Unscented filtering and nonlinear estimation. *Proceedings of the IEEE*, 92(3):401–422, Mar. 2004. ISSN 1558-2256. doi: 10.1109/JPROC.2003.823141. Conference Name: Proceedings of the IEEE.

[39] S. Julier, J. Uhlmann, and H. Durrant-Whyte. A new approach for filtering nonlinear systems. In *Proceedings of 1995 American Control Conference - ACC'95*, volume 3, pages 1628–1632, Seattle, WA, USA, 1995. American Autom Control Council. ISBN 978-0-7803-2445-9. doi: 10.1109/ACC.1995.529783. URL http://ieeexplore.ieee.org/document/529783/.

[40] S. Julier, J. Uhlmann, and H. Durrant-Whyte. A new method for the nonlinear transformation of means and covariances in filters and estimators. *IEEE Trans. Automat. Contr.*, 45(3):477–482, Mar. 2000. ISSN 00189286. doi: 10.1109/9.847726. URL http://ieeexplore.ieee.org/document/847726/.

[41] I. Knowles and R. J. Renka. Methods for numerical differentiation of noisy data. *Electron. J. Differ. Equ*, 21:235–246, 2014.

[42] D. S. Lauretta, S. S. Balram-Knutson, E. Beshore, W. V. Boynton, C. Drouet d'Aubigny, D. N. DellaGiustina, H. L. Enos, D. R. Golish, C. W. Hergenrother, E. S. Howell, C. A. Bennett, E. T. Morton, M. C. Nolan, B. Rizk, H. L. Roper, A. E. Bartels, B. J. Bos, J. P. Dworkin, D. E. Highsmith, D. A. Lorenz, L. F. Lim, R. Mink, M. C. Moreau, J. A. Nuth, D. C. Reuter, A. A. Simon, E. B. Bierhaus, B. H. Bryan, R. Ballouz, O. S. Barnouin, R. P. Binzel, W. F. Bottke, V. E. Hamilton, K. J. Walsh, S. R. Chesley, P. R. Christensen, B. E. Clark, H. C. Connolly, M. K. Crombie, M. G. Daly, J. P. Emery, T. J. McCoy, J. W. McMahon, D. J. Scheeres, S. Messenger, K. Nakamura-Messenger, K. Righter, and S. A. Sandford. OSIRIS-REx: Sample Return from Asteroid (101955) Bennu. *Space Science Reviews*, 212 (1):925–984, Oct. 2017. ISSN 1572-9672. doi: 10.1007/s11214-017-0405-1. URL https://doi.org/10.1007/s11214-017-0405-1.

[43] G. Lentaris, K. Maragos, I. Stratakos, L. Papadopoulos, O. Papanikolaou, D. Soudris, M. Lourakis, X. Zabulis, D. Gonzalez-Arjona, and G. Furano. High-performance embedded computing in space: Evaluation of platforms for vision-based navigation. *Journal of Aerospace Information Systems*, 15(4):178–192, 2018. doi: 10.2514/1.I010555. URL https://doi.org/10.2514/1.I010555.

[44] J.-S. Li, Z. Yang, and Y.-Z. Luo. A review of space-object collision probability computation methods. *Astrodyn*, 6(2), June 2022. ISSN 2522-0098. doi: 10.1007/s42064-021-0125-x. URL https://doi.org/10.1007/s42064-021-0125-x.

[45] P. D. Lizia, R. Armellin, and M. Lavagna. Application of high order expansions of two-point boundary value problems to astrodynamics. *Celest Mech Dyn Astr*, 102(4): 355–375, Dec. 2008. ISSN 0923-2958, 1572-9478. doi: 10.1007/s10569-008-9170-5. URL http://link.springer.com/10.1007/s10569-008-9170-5.

[46] Y.-z. Luo and Z. Yang. A review of uncertainty propagation in orbital mechanics. *Progress in Aerospace Sciences*, 89:23–39, Feb. 2017. ISSN 03760421. doi: 10.1016/j.paerosci.2016.12.002. URL https://linkinghub.elsevier.com/retrieve/pii/S0376042116301051.

[47] F. L. Markley and J. L. Crassidis. *Fundamentals of Spacecraft Attitude Determination and Control*. Springer New York, New York, NY, 2014. ISBN 978-1-4939-0801-1 978-1-4939-0802-8. doi: 10.1007/978-1-4939-0802-8. URL http://link.springer.com/10.1007/978-1-4939-0802-8.

[48] I. Martin, M. Dunstan, and M. S. Gestido. Planetary surface image generation for testing future space missions with pangu. In *2nd RPI Space Imaging Workshop*. Sensing, Estimation, and Automation Laboratory, 2019.

[49] A. Mashiku and J. R. Carpenter. A Collision Avoidance Strategy for a Potential Natural Satellite around the Asteroid Bennu for the Osiris-Rex Mission. In *AIAA/AAS Astrodynamics Specialist Conference*, Long Beach, California, Sept. 2016. American Institute of Aeronautics and Astronautics. ISBN 978-1-62410-445-9. doi: 10.2514/6.2016-5655. URL https://arc.aiaa.org/doi/10.2514/6.2016-5655.

[50] M. Massari, P. Di Lizia, F. Cavenago, and A. Wittig. Differential Algebra software library with automatic code generation for space embedded applications. In *2018 AIAA Information Systems-AIAA Infotech @ Aerospace*, Kissimmee, Florida, Jan. 2018. American Institute of Aeronautics and Astronautics. ISBN 978-1-62410-527-2. doi: 10.2514/6.2018-0398. URL https://arc.aiaa.org/doi/10.2514/6.2018-0398.

[51] W. MathWorld. Rodrigues' rotation formula, 2023. URL https://mathworld.wolfram.com/RodriguesRotationFormula.html. Last visited: 11-22-2023.

[52] NASA. Nasa confirms dart mission impact changed asteroid's motion in space, 2022. URL https://www.nasa.gov/press-release/

nasa-confirms-dart-mission-impact-changed-asteroid-s-motion-in-space. Last visited: 11-22-2023.

[53] NASA. Audit of nasa's deep space network, july 12, 2023, 2023. URL https://oig.nasa.gov/docs/IG-23-016.pdf. Last visited: 11-22-2023.

[54] NASA. Nasa's osiris-rex spacecraft views sample return capsule's departure, 2023. URL https://blogs.nasa.gov/osiris-rex/2023/10/03/nasas-osiris-rex-spacecraft-views-sample-return-capsules-departure/. Last visited: 11-22-2023.

[55] C. f. N. E. O. C. NASA. Neo basics. URL https://cneos.jpl.nasa.gov/about/neo_groups.html. Last visited: 11-22-2023.

[56] R. S. Park and D. J. Scheeres. Nonlinear mapping of gaussian statistics: theory and applications to spacecraft trajectory design. *Journal of guidance, Control, and Dynamics*, 29(6):1367–1375, 2006.

[57] R. S. Park and D. J. Scheeres. Nonlinear Semi-Analytic Methods for Trajectory Estimation. *Journal of Guidance, Control, and Dynamics*, 30(6):1668–1676, Nov. 2007. ISSN 0731-5090, 1533-3884. doi: 10.2514/1.29106. URL https://arc.aiaa.org/doi/10.2514/1.29106.

[58] A. Pellacani, F. Cabral, A. Alcalde, P. Kicman, J. Lisowski, I. Gerth, and B. Burmann. Semi-autonomous attitude guidance using relative navigation based on line of sight measurements – Aim scenario. *Acta Astronautica*, 152:496–508, Nov. 2018. ISSN 0094-5765. doi: 10.1016/j.actaastro.2018.08.051. URL https://www.sciencedirect.com/science/article/pii/S0094576517316065.

[59] A. Pellacani, P. Kicman, M. Suatoni, M. Casasco, J. Gil, and I. Carnelli. Design and validation of a GNC system for missions to asteroids: the AIM scenario. *CEAS Space J*, 10(4):555–566, Dec. 2018. ISSN 1868-2510. doi: 10.1007/s12567-017-0189-x. URL https://doi.org/10.1007/s12567-017-0189-x.

[60] A. PELLACANI, M. GRAZIANO, M. FITTOCK, J. GIL, and I. CARNELLI. HERA vision based GNC and autonomy. page 14 pages, 2019. doi: 10.13009/EUCASS2019-39. URL https://www.eucass.eu/doi/EUCASS2019-0039.pdf. Artwork Size: 14 pages Medium: PDF Publisher: Proceedings of the 8th European Conference for Aeronautics and Space Sciences. Madrid, Spain, 1-4 july 2019.

[61] L. Perea, J. How, L. Breger, and P. Elosegui. Nonlinearity in sensor fusion: divergence

issues in ekf, modified truncated gsf, and ukf. In *AIAA Guidance, Navigation and Control Conference and Exhibit*, page 6514, 2007.

[62] V. Pesce, S. Silvestrini, and A. Colagrossi. *Modern spacecraft guidance, navigation, and control: from system modeling to AI and innovative applications*. Elsevier, 2022. ISBN 978-0-323-90916-7.

[63] A. Rossi, F. Marzari, J. R. Brucato, V. Della Corte, E. Dotto, S. Ieva, S. L. Ivanovski, A. Lucchetti, E. M. Epifani, M. Pajola, et al. Dynamical evolution of ejecta from the dart impact on dimorphos. *The Planetary Science Journal*, 3(5):118, 2022.

[64] T. Saiki, Y. Takei, T. Takahashi, S. Kikuchi, H. Sawada, C. Hirose, F. Terui, N. Ogawa, Y. Mimasu, G. Ono, et al. Overview of hayabusa2 asteroid proximity operation planning and preliminary results. *Transactions of the Japan Society for Aeronautical and Space Sciences, Aerospace Technology Japan*, 19(1):52–60, 2021.

[65] R. Serra, D. Arzelier, M. Joldes, J.-B. Lasserre, A. Rondepierre, and B. Salvy. Fast and Accurate Computation of Orbital Collision Probability for Short-Term Encounters. *Journal of Guidance, Control, and Dynamics*, 39(5):1009–1021, May 2016. ISSN 0731-5090, 1533-3884. doi: 10.2514/1.G001353. URL `https://arc.aiaa.org/doi/10.2514/1.G001353`.

[66] S. Servadio et al. *New developments in nonlinear filtering using differential algebra*. PhD thesis, 2021.

[67] D. Simon. *Optimal state estimation: Kalman, H infinity, and nonlinear approaches*. John Wiley & Sons, 2006.

[68] N. Stacey and S. D'Amico. Adaptive and Dynamically Constrained Process Noise Estimation for Orbit Determination. *IEEE Trans. Aerosp. Electron. Syst.*, 57(5): 2920–2937, Oct. 2021. ISSN 0018-9251, 1557-9603, 2371-9877. doi: 10.1109/TAES.2021.3074205. URL `https://ieeexplore.ieee.org/document/9409684/`.

[69] G. W. Stewart. *Matrix algorithms: volume 1: basic decompositions*. SIAM, 1998.

[70] B. D. Tapley, B. E. Schutz, and G. H. Born. *Statistical orbit determination*. Elsevier Academic Press, Amsterdam ; Boston, 2004. ISBN 978-0-12-683630-1.

[71] Y. Tsuda, M. Yoshikawa, M. Abe, H. Minamino, and S. Nakazawa. System design of the hayabusa 2—asteroid sample return mission to 1999 ju3. *Acta Astronautica*, 91: 356–362, 2013.

[72] D. A. Vallado. *Fundamentals of astrodynamics and applications*, volume 12. Springer Science & Business Media, 2001.

[73] M. Valli. Nonlinear estimation and filtering for space applications. 2013.

[74] R. Van Der Merwe. *Sigma-point Kalman filters for probabilistic inference in dynamic state-space models*. Oregon Health & Science University, 2004.

[75] R. Van der Merwe and E. Wan. The square-root unscented Kalman filter for state and parameter-estimation. In *2001 IEEE International Conference on Acoustics, Speech, and Signal Processing. Proceedings (Cat. No.01CH37221)*, volume 6, Salt Lake City, UT, USA, 2001. IEEE. ISBN 978-0-7803-7041-8. doi: 10.1109/ICASSP.2001.940586. URL `http://ieeexplore.ieee.org/document/940586/`.

[76] F. Venditti, S. Marshall, L. Zambrano Marin, M. Devogele, and A. McGilvray. The population of binary and triple near-earth asteroids observed with the arecibo planetary radar system. In *AAS/Division for Planetary Sciences Meeting Abstracts*, volume 54, pages 104–01, 2022.

[77] A. Wald. Sequential tests of statistical hypotheses. *The Annals of Mathematical Statistics*, 16(2):117–186, 1945. ISSN 00034851. URL `http://www.jstor.org/stable/2235829`.

[78] A. Wald. *Sequential analysis*. Courier Corporation, 2004.

[79] B. Williams, P. Antreasian, E. Carranza, C. Jackman, J. Leonard, D. Nelson, B. Page, D. Stanbridge, D. Wibben, K. Williams, M. Moreau, K. Berry, K. Getzandanner, A. Liounis, A. Mashiku, D. Highsmith, B. Sutter, and D. S. Lauretta. OSIRIS-REx Flight Dynamics and Navigation Design. *Space Science Reviews*, 214(4):69, June 2018. ISSN 0038-6308, 1572-9672. doi: 10.1007/s11214-018-0501-x. URL `http://link.springer.com/10.1007/s11214-018-0501-x`.

[80] D. Woodbury and J. Junkins. On the Consider Kalman Filter. In *AIAA Guidance, Navigation, and Control Conference*, Toronto, Ontario, Canada, Aug. 2010. American Institute of Aeronautics and Astronautics. ISBN 978-1-60086-962-4. doi: 10.2514/6.2010-7752. URL `https://arc.aiaa.org/doi/10.2514/6.2010-7752`.

[81] C. Yanez, M. Gupta, V. Morand, and J. Dolado. On the gaussianity validity time for orbital uncertainty propagation. 2019.

[82] N. Yongfang and Z. Tao. Scaling parameters selection principle for the scaled unscented kalman filter. *Journal of Systems Engineering and Electronics*, 29(3):601–610, 2018.

# A | Appendix A: Additional analysis results

## A.1. Additional MOCRE results in Unsafe EXP

This section of the appendix contains additional results with respect to those shown and analyzed in section 5.1.

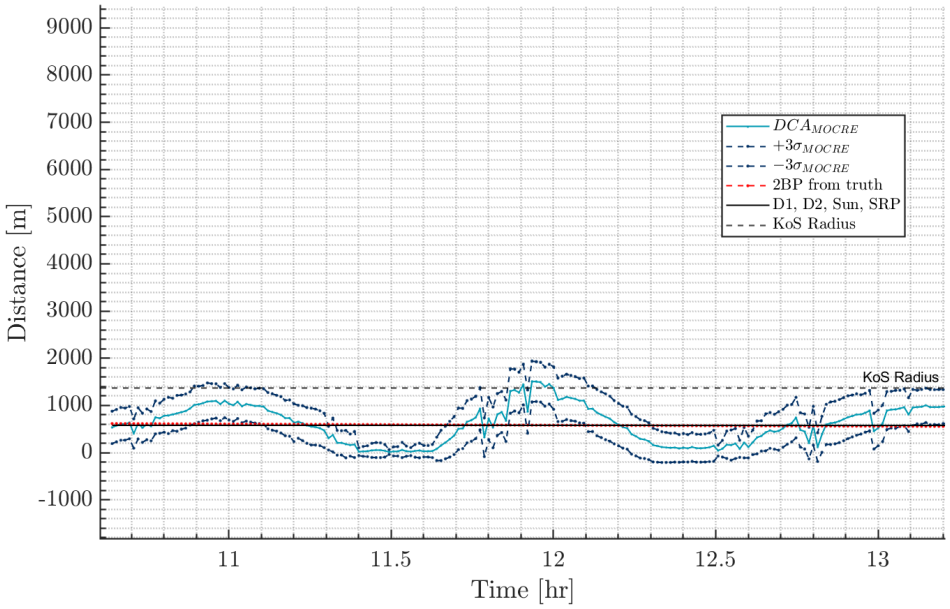


Figure A.1: MOCRE closest approach distance evaluation with HFM measurements - Unsafe EXP (default tuning).

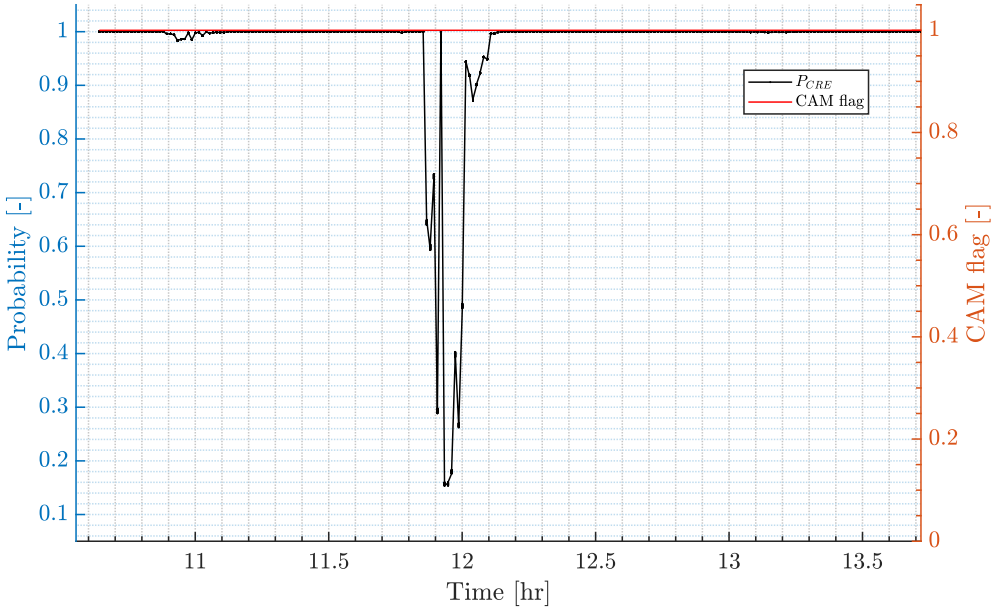


Figure A.2: PoC and CAM flag from MOCRE output with noisy measurements - Unsafe EXP (Default tuning).

## A.2. Additional Parallel filter results

This section of the appendix contains additional results with respect to those shown and analyzed in section 5.2.

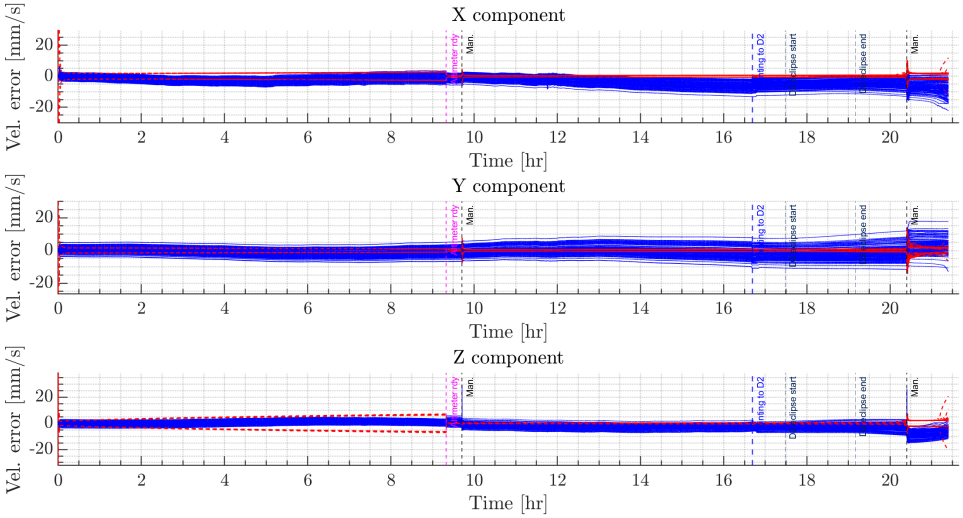


Figure A.3: KEP: Velocity errors and $3\sigma$ covariance bounds with $\mu$ uncertainty - Nominal EXP @CAM frame.

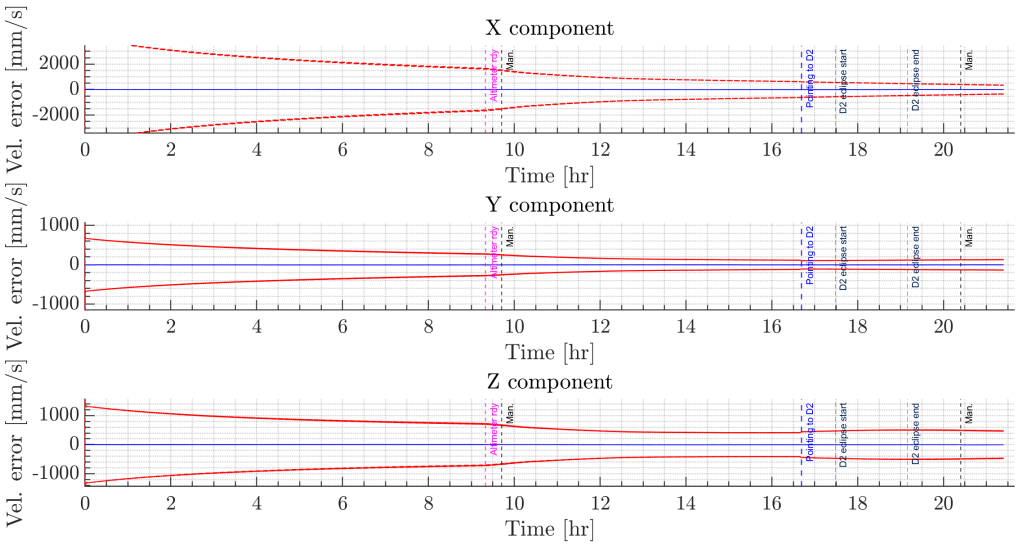


Figure A.4: Cartesian KEP: Velocity errors and $3\sigma$ covariance bounds with $\mu$ uncertainty - Nominal EXP @CAM frame.

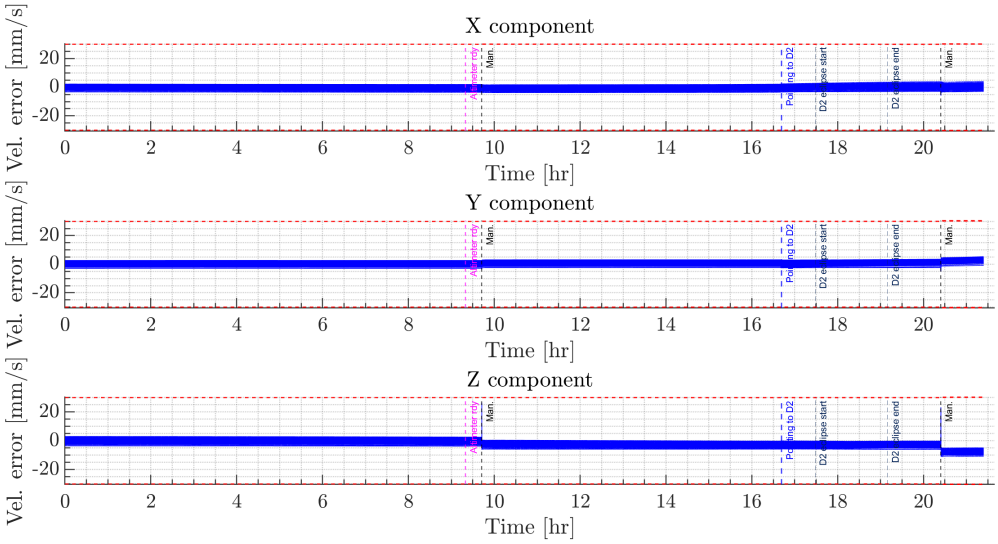


Figure A.5: Cartesian HF: Velocity errors and $3\sigma$ covariance bounds without $\mu$ uncertainty - Nominal EXP @CAM frame.

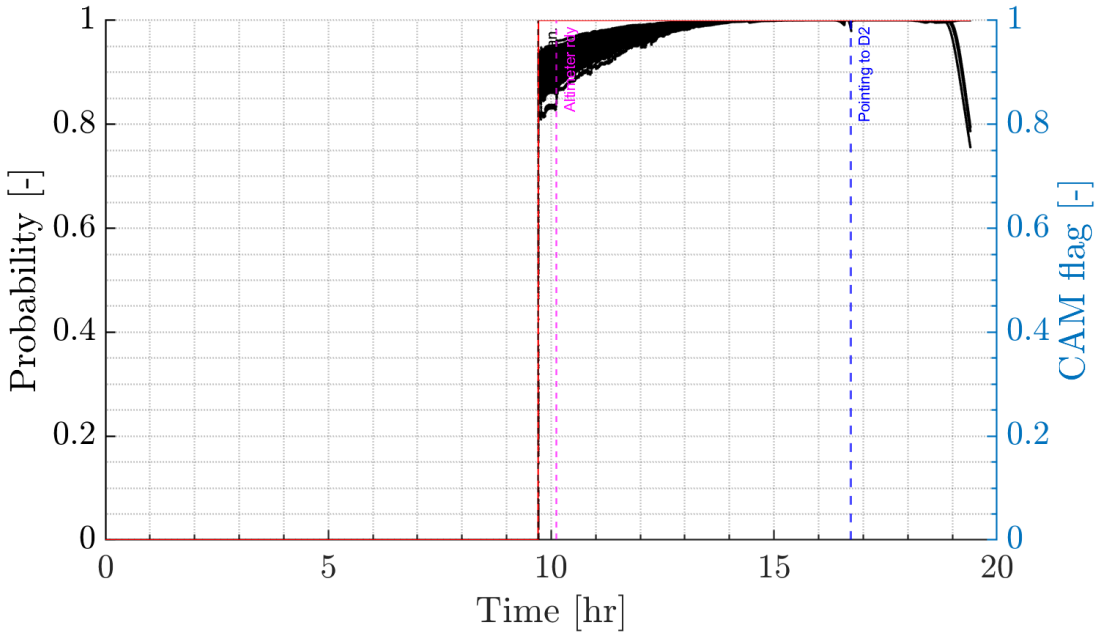


Figure A.6: PoC (black) and CAM flag (red) from DCA prediction of Cartesian filter with 2BP dynamics without $\mu$ parameter uncertainty - Unsafe EXP.

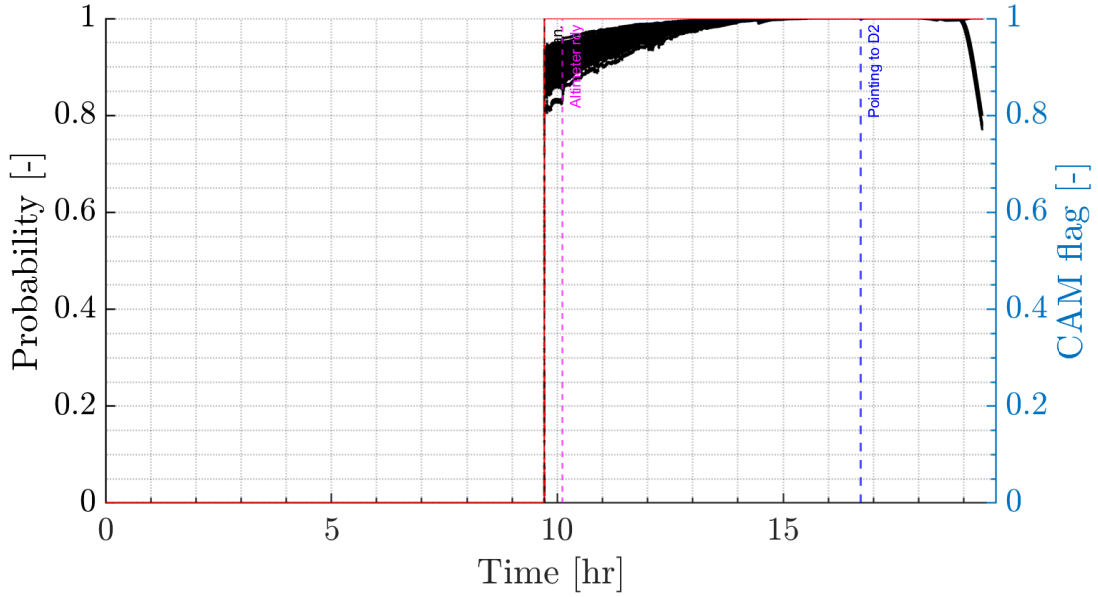


Figure A.7: PoC (black) and CAM flag (red) from DCA prediction of Cartesian filter with refined dynamics without $\mu$ parameter uncertainty - Unsafe EXP.